High Pressure Minerals in the Earth and Moon: Understanding the Lunar Impact History and Earth's Deep Water Cycle

---

DISSERTATION

zur Erlangung des akademischen Grades eines Doktors der Naturwissenschaften (Dr. rer. nat.) in der Bayreuther Graduiertenschule für Mathematik und Naturwissenschaften (BayNAT) der Universität Bayreuth

vorgelegt von

Niccolò Satta

aus Sassari (Italien)

Bayreuth, 2020

Die vorliegende Arbeit wurde in der Zeit von Juni 2017 bis April 2020 in Bayreuth am Bayerischen Geoinstitut unter Betreuung von Herrn Dr. Hauke Marquardt angefertigt.

Vollständiger Abdruck der von der Bayreuther Graduiertenschule für Mathematik und Naturwissenschaften (BayNAT) der Universität Bayreuth genehmigten Dissertation zur Erlangung des akademischen Grades eines Doktors der Naturwissenschaften (Dr.rer.nat.).

Dissertation eingereicht am: 30.04.2020
Zulassung durch das Leitungsgremium: 30.04.2020
Wissenschaftliches Kolloquium: 30.06.2020

Amtierender Direktor: Prof. Dr. Markus Lippitz

Prüfungsausschuss:
Prof. Dr. Hauke Marquardt (Gutachter)
Prof. Dr. Daniel Frost (Gutachter)
PD Dr. Gerd Steinle-Neumann (Vorsitz)
PD Dr. Catherine McCammon

Summary

The detection and study of high pressure minerals either remotely through seismology or in natural specimens can provide important constraints on physical and chemical properties occurring at normally inaccessible conditions, such as during planetary impact events or deep inside planets. For four and a half billion years, countless impact events have shattered the Moon's surface, leaving a unique record of impact craters. Understanding the nature, and estimating the ages of the largest lunar craters was among the main goals of the Apollo missions. However, despite the large number of samples collected, the ages of the largest craters are still debated. $^{40}Ar/^{39}Ar$ ages constrained in lunar samples may be biased by subsequent thermal events, hampering our current understanding of the Moon's collisional history. A viable way to evaluate this possibility is to evaluate the behaviour of lunar regolith under shock compression.
In this thesis, scanning and transmission electron microscope techniques are used to constrain shock conditions recorded in a regolith breccia, by a detailed description of shock-induced microtextures and mineralogical assemblages. I present the first observation of natural ferropericlase in a lunar rock. My observations suggest that the lunar ferropericlase formed as a result of shock-induced incongruent melting of olivine, a phenomenon found previously only in experiments. Furthermore, I estimated the pressure - temperature evolution of the shock event. Our results indicate that because of its porous nature, the lunar regolith can experience elevated temperatures even during low magnitude impacts. Based on these findings, we suggest that a more accurate estimate of the ages of the main collisional episodes of the Moon's surface requires a re-evaluation of the current $^{40}Ar/^{39}Ar$ constrains.

Subduction of altered oceanic slabs and hydrous sediments control the input of water into the deep Earth's interior. During subduction, hydrous materials are exposed to increasing pressures and temperatures, which causes a chain of prograde metamorphic reactions to occur. Previous experimental investigations indicate that water, bound as hydroxyl groups, can be passed between hydrous phases and consequently delivered by subduction to the deepest portions of the Earth's mantle. Seismological surveys provide information

on the seismic structures that characterize subducting scenarios, however, an accurate interpretation of the hydration state is achievable only through experimental constraints on the possible seismic signatures of these hydrous phases.

In this thesis, I conducted two projects with the aim of characterizing the single-crystal elasticity of phase E and δ-(Al,Fe)OOH, two hydrous phases relevant for the delivery and stabilization of water in the Earth's deep interior.

In the case of phase E, experimental methodologies were used for the synthesis of single crystals, and an accurate chemical characterization was achieved with state-of-the-art analytical techniques. Brillouin spectroscopy and X-ray diffraction analysis were employed to determine the full elastic tensor and unit-cell parameters, respectively. I found that phase E has very low aggregate velocities, significantly lower than those of other minerals expected to be stable at the same pressure and temperature conditions. By combining my findings with previous experimental investigations, aggregate velocities of subducted rocks were evaluated assuming different hydration states. These results imply that if present, phase E is capable of significantly lowering seismic wave velocities, raising the possibility that this hydrous phase could be detected remotely allowing hydrated regions of the deep mantle to be mapped.

By performing Brillouin spectroscopy and X-ray diffraction measurements in a diamond-anvil cell, the structure and elastic properties of δ-(Al,Fe)OOH have been examined up to pressures where a second order phase transformation occurs from the $P2_1nm$ space group to $Pnnm$. The elastic tensors of both the $P2_1nm$ and $Pnnm$ structures were constrained experimentally. In addition, by tracking the intensity attenuation of selected reflections we were able to tightly constrain the transition pressure. Our findings are in agreement with previous investigations on the aluminium end member, suggesting that the incorporation of Fe^{3+} has a limited effect on the $P2_1nm$ to $Pnnm$ phase transition. Both X-ray diffraction and Brillouin spectroscopy results show that, prior to the transition into the $Pnnm$ phase, the $P2_1nm$ δ-(Al,Fe)OOH phase experiences an elastic softening. This softening is associated with a change in the hydrogen bond configuration from asymmetric ($P2_1nm$) to disordered ($Pnnm$). Similar changes can be expected in other hydroxide minerals, suggesting that the elastic softening may be a common precursor of hydrogen bond symmetrization.

Zusammenfassung

Der Nachweis von Hochdruckmineralen, entweder indirekt durch Seismologie oder direkt in natürlichen Gesteinsproben, kann wichtige Hinweise auf die physikalischen und chemischen Zustände unter normalerweise nicht zugänglichen p,T Bedingungen liefern. Viereinhalb Milliarden Jahre lang haben zahllose Einschlagsereignisse die Oberfläche des Mondes zertrümmert und dabei eine einzigartige Ansammlung von Einschlagskratern hinterlassen. Das Verständnis der Natur sowie die Abschätzung der Alter der größten Einschlagskrater war eines der Hauptziele der Apollomissionen. Trotz der großen Anzahl von Proben, die dabei gesammelt wurden, wird das Alter großen Einschlagskrater immer noch diskutiert. $^{40}Ar/^{39}Ar$ Alter, die in den lunaren Proben ermittelt wurden, können durch nachfolgende thermische Ereignisse beeinflusst worden sein, so dass unser gegenwärtiges Verständnis der Kollisionsgeschichte des Mondes unvollständig bleibt. Ein gangbarer Weg, um diese Möglichkeit zu bewerten, besteht in der Untersuchung des Verhaltens von lunarem Regolith unter Schockkompression.

In der vorliegenden Arbeit wurden raster- und transmissionselektronenmikroskopische Methoden eingesetzt, um die in Regolith-Brekzien dokumentierten Schockbedingungen durch eine detaillierte Beschreibung der schockinduzierten Mikrotexturen und Mineralvergesellschaftungen einzugrenzen. In dieser Studie wird die erstmalige Beobachtung von natürlichem Ferroperiklas in einem lunaren Gestein vorgestellt. Darüber hinaus deuten weitere Beobachtungen darauf hin, dass der lunare Ferroperiklas als Resultat von shockinduziertem inkongruentem Schmelzen von Olivin entstanden ist, einem Phänomen, das bisher nur in Experimenten beobachtet werden konnte. Die Druck-Temperatur Entwicklung des Schockereignisses wurde abgeschätzt. Die Ergebnisse deuten darauf hin, dass der lunare Regolith aufgrund seiner porösen Struktur erhöhte Temperaturen auch bei Einschlägen geringer Magnitude erfahren kann. Basierend auf diesen Resultaten wird vorgeschlagen, dass eine genauere Bestimmung der Alter der Haupteinschlagsphasen auf der Mondoberfläche eine Reevaluierung der gegenwärtigen $^{40}Ar/^{39}Ar$ Grenzbedingungen erforderlich macht.

Subduktion von alterierten ozeanischen Platten und wasserhaltigen Sedimenten kontrollieren die Zufuhr von Wasser in das tiefe Erdinnere. Während der Subduktion werden die wasserhaltigen Materialien zunehmenden Drücken und Temperaturen ausgesetzt, was eine Kette von prograden metamorphen Reaktionen auslöst. Vorhergehende experimentelle Untersuchungen deuten darauf hin, dass Wasser, gebunden als Hydroxylgruppen, zwischen wasserhaltigen Phasen ausgetauscht werden kann und folglich durch Subduktion bis in die tiefsten Bereiche des Erdmantels verbracht werden kann. Seismologische Studien liefern Informationen über die seismischen Strukturen, die charakteristisch für Subduktionsbereiche sind, eine akkurate Interpretation des Hydratisierungszustandes kann jedoch nur durch experimentelle Bestimmungen der möglichen seismischen Signaturen der wasserhaltigen Phasen erreicht werden.

In der vorliegenden Arbeit wurden zwei Projekte mit dem Ziel durchgeführt, die Einkristall-Elastizität der Phase E und δ-(Al,Fe)OOH zu bestimmen, zwei wasserhaltigen Phasen, die für den Transport und die Speicherung von Wasser im tiefen Erdinneren relevant sind. Im Fall der Phase E wurden experimentelle Methoden für die Synthese von Einkristallen genutzt, und eine akkurate chemische Charakterisierung wurde mit modernen analytischen Methoden erreicht. Brillouinspektroskopie und Röntgenbeugungsanalyse wurden verwendet, um den vollständigen elastischen Tensor bzw. die Gitterparameter zu bestimmen. Mithilfe dieser Daten konnten wir bestimmen, dass die Phase E nur sehr niedrige Aggregatgeschwindigkeiten hat, die signifikant geringer sind als die anderer Minerale, die bei denselben Drücken und Temperaturen stabil sind. In dem wir unsere Resultate mit denen früher experimenteller Untersuchungen kombinierten, konnten wir die Aggregatgeschwindigkeiten von subduziertem Gesteinen mit unterschiedlichem Hydratisierungsgrad evaluieren. Diese Resultate implizieren, dass - falls vorhanden - Phase E fähig ist, die seismischen Wellengeschwindigkeiten signifikant zu erniedrigen, und so die Möglichkeit eröffnet, dass diese wasserhaltige Phase durch Fernerkundung detektiert werden kann und hydratisierte Bereiche des tiefen Mantels kartiert werden können.

Durch Brillouinspektroskopie und Röntgenbeugungsmessungen in einer Diamantstempelzelle wurden die Struktur und die elastischen Eigenschaften von δ-(Al,Fe)OOH bis zu einem Druck untersucht, bei dem eine Phasentransformation zweiter Ordnung von der $P2_1nm$ zur $Pnnm$ Raumgruppe auftritt. Die elastischen Tensoren von beiden Strukturen ($P2_1nm$ und $Pnnm$) wurden experimentell bestimmt. Weiterhin waren wir durch die Verfolgung der Intensitätsverringerung ausgewählter Reflektionen in der Lage, den Übergangsdruck eng einzugrenzen. Unsere Ergebnisse sind in Übereinstimmung mit vorhergehenden Untersuchungen an dem reinen Aluminium-Endglied, was darauf hindeutet, dass der Einbau von Fe^{3+} nur einen geringen Einfluss auf den $P2_1nm$ zu $Pnnm$ Phasenübergang hat. Sowohl die Röntgenbeugung als auch die Brillouinspektroskopie zeigen, dass,

vor dem Übergang in die *Pnnm* Phase, die $P2_1nm$ δ-(Al,Fe)OOH Phase eine Erniedrigung der elastischen Parameter aufweist. Diese Erniedrigung ist assoziiert mit einem Wechsel in der Konfiguration der Wasserstoffbindung von asymmetrisch ($P2_1nm$) zu ungeordnet (*Pnnm*). Ähnliche Änderungen können auch in anderen Hydroxid-Mineralen erwartet werden, was darauf hindeutet, dass die Erniedrigung der elastischen Parameter ein verbreiteter Vorläufer der Symmetrisierung von Wasserstoffbindungen sein könnte.

Acknowledgments

I would like to express my gratitude to my supervisor, Prof. Dr. Hauke Marquardt for his continuous support and guidance throughout my PhD project.

I wish to thank Ohtani-sensei for giving me the opportunity to work on the Apollo project.

A special thanks to Dr. Tiziana Boffa Ballaran for her help and contagious optimism, and to Dr. Alexander Kurnosov and Giacomo Criniti for their fundamental contributions to the Brillouin spectroscopy and X-ray diffraction experiments.

Another special thanks to Dr. Sergio Speziale for sharing with me his always interesting scientific viewpoints.

I would like to thank Catherine McCammon for helping with Mössbauer data and Raphael Njul for preparing the samples. I wish also to thank all the BGI and TU staff members.

A huge thanks to the Q.C.S. group Johannes, Filippe and Joe, for all the laughs.

Last, but not least, Kassidy, I thank you for your unconditional support and most of all, patience.

Contents

1 Introduction

The geological evolution of the Earth is the result of a combination between extra- and intra-planetary processes, that shaped our planet over a time span of billions of years.
In the last decades, various disciplines in the Earth and Planetary sciences have seen incredible achievements. In these, technological advancements were pivotal. Experimental approaches combined with state-of-art analytic methodologies now allow the exploration of matter at physical conditions relevant to the Earth's interior, opening a window to explore processes that are typically confined to the deep Earth. In parallel, space exploration missions have given us unique opportunities to study the nature of cosmic bodies, providing important confirmations to dynamical processes of the Solar System. While these scientific findings provided answers to some questions, new and valuable questions are arising, and several of them have the study of high pressure minerals as common denominator. Answering these questions would bring us a step closer to understanding the geological evolution of our planet, as well as the likelihood that other planetary bodies developed plate tectonics and habitable conditions.

Currently, there are major on-going debates with regards to the nature and timing of *Late Heavy Bombardment* (LHB) (Wetherill, 1975). The LHB involves a hypothesized scenario in which pulses of asteroidal impactors stormed the planetary population of the inner Solar System (Gomes et al., 2005), influencing the geological processes (Glikson, 2001; Marchi et al., 2014) and evolution of life on Earth (Sleep et al., 1989; Abramov and Mojzsis, 2009; Nutman et al., 2016). The LHB finds its roots in lunar breccias - rock lithified by shock compression, which have been brought back to the Earth by the astronauts of the Apollo missions (Turner et al., 1973; Tera et al., 1974). However, the LHB is now challenged by new evidences (Bottke and Norman, 2017), and what was the most remarkable discovery of the space exploration may be simply the result of speculative intepretations (Boehnke and Harrison, 2016).
The Moon holds one of the best preserved - and accessible - record of impact events on its surface, and should therefore be able to provide information to delineate the timing and dynamics of the LHB.

In this thesis, I show the importance of characterizing high-pressure minerals in lunar shocked samples at the micro-scale to better understand impact kinetics on the Moon's surface. In particular, I use a series of analytical techniques to characterize shock-related features in a lunar breccia that constrain the behaviour of lunar surface rocks under shock compression. I show that the lunar regolith can be exposed to very high temperatures even during low magnitude impact, and I discuss this finding with respect to our understanding of the collisional history of the Moon.

Another major puzzle for our understanding of the geological evolution of the Earth regards water and its distribution in the Earth's interior. Water is intimately connected to the geological events that controlled, and still control the Earth's evolution, influencing all processes that shape our planet at large scale, ranging from the lithosphere to the deep mantle (Asimow and Langmuir, 2003; Aubaud et al., 2004; Hirth and Kohlstedt, 1996; Ohtani, 2005).
According to theoretical calculations (Peacock, 1990), experiments (Kohlstedt et al., 1996; Bolfan-Casanova, 2005), and analysis of diamond inclusions (Wirth et al., 2007; Pearson et al., 2014; Tschauner et al., 2018), the hydrosphere constitutes just a small fraction of the terrestrial water budget, which sees most of its mass stored in the Earth's crust and mantle reservoirs (Ohtani, 2005). Plate tectonics allows the exchange of water between the hydrosphere and Earth's interior. The subduction of oceanic lithosphere is the main process to deliver large masses of hydrous material to the Earth's interior (Bebout, 1995). Therefore, understanding the physical processes that characterize subducting slabs can provide a new understanding on the delivery and distribution of water in the Earth's interior.
In this thesis, I empasize how the elastic properties of major high pressure hydrous phases are needed to quantify water and its distribution in subduction zones. In particular, I will follow an experimental approach to characterize the elasticity of two hydrous phases, phase E and δ-(Al,Fe)OOH, that are thought to be main actors in the hydration of subducted slabs at various depths in the Earth's mantle.

1.1 A Brief Overview on the Impact History of the Moon

The Moon's geological quiescence allowed the preservation of its lithosphere during the last four billion years, offering the opportunity to study the main events in its geological history through surface features (Hiesinger and Head, 2006; Stöffler, 2006).
The most striking feature of the Moon's surface is its cratering record, which shows a wide variety of sizes and morphological aspects. Over the last billions of years the Moon has been exposed to countless impacts that constantly fragmented its primordial crystalline basement (Stöffler, 2006). Currently, the primordial crustal rocks constitute only a limited fraction of the Moon's surface, which is mostly covered by a blanket of shocked debris (lunar breccias), mixed with regolith, the unconsolidated finest fraction (Lucey et al., 2006).
The collection of rocky samples from different lunar terrains was among the primary goals of the Apollo missions. From 1969 to 1972, starting with Apollo 11 and ending with the Apollo 17 mission, ten astronauts walked on the Moon's surface, and brought back to Earth almost 400 kg of lunar rocks (Hiesinger and Head, 2006). Prior to the Apollo-era, most of the lunar craters were thought to have a volcanic origin, e.g. Spurr (1949). The extent of shock metamorphism in the lunar samples, however, proves that the main lunar craters (or basins) are in fact the result of large collisional episodes.
The ages of the main lunar basins have been used to define a chronology of the Moon's collisional history, that currently counts five different periods which, from the oldest to the youngest, are the *pre-Nectarian*, the *Nectarian*, the *Imbrian*, the *Eratosthenia*n and the *Copernican* periods (Wilhelms et al., 1987; Stöffler and Ryder, 2001). Each of these periods is linked to the formation of a large basin, whose age was directly inferred using $^{40}Ar/^{39}Ar$ dating and U–Pb isotopic compositions of shocked samples. For example, the Imbrium basin (∼1100 km ∅) was sampled by the Apollo 15 mission, and its absolute age was used to mark the limit between Nectarian and Imbrian periods (Wilhelms et al., 1987; Neukum and Ivanov, 1994; Stöffler and Ryder, 2001).
An even more remarkable outcome of the Apollo missions relates to the ages of the impact events, showing that most of the collisional episodes are concentrated between 3.75 and 3.95 Ga (Stöffler, 2006). This aspect lead to the formulation of the LHB hypothesis, stating that the Moon experienced a cataclysm (i.e., a spike in the flux of impactors) which resulted in the production of the majority of the lunar basins (Tera et al., 1974; Ryder et al., 2000). However, this hypothesis has been challenged by Schaeffer and Schaeffer (1977), who pointed out the complications related to the scarce sample population, which is indeed representative of only a small fraction of the total area of the Moon's surface

(Warren and Taylor, 2014). In addition, the ages on these cratering episodes were constrained by disturbances in isotopic systems (Jessberger et al., 1974; Dalrymple and Ryder, 1993, 1996). Using the $^{40}Ar/^{39}Ar$ system, for example, it is possible to track partial losses of ^{40}Ar, which can be related to thermal events triggered by impacts, and therefore be used to constrain the age of the cratering episodes. However, subsequent impact episodes can cause an overprinting of the thermal disturbance within the same sample (Mercer et al., 2015), making it difficult to obtain reliable absolute ages for individual cratering events (Fernandes et al., 2013), yielding, as for the case of the Imbrium basing, different ages (Stöffler and Ryder, 2001). Understanding the shock metamorphism conditions in terms of pressures and temperatures would facilitate a better understanding of thermal events recorded in the Apollo samples. Therefore it would provide a better understanding on the main lunar impact event, and a test for the LHB hypothesis. The lunar samples brought back from the Apollo missions should contain all the information necessary to characterize the behavior of lunar rocks under shock compression at the microscale, which is thus far constrained by only a single study (Kaneko et al., 2015).

1.1.1 Linking Impacts, Microtextures and Phase Transitions

In any given material, an impact can induce shock only if the shock-induced deformation travels faster than the velocity of sound.

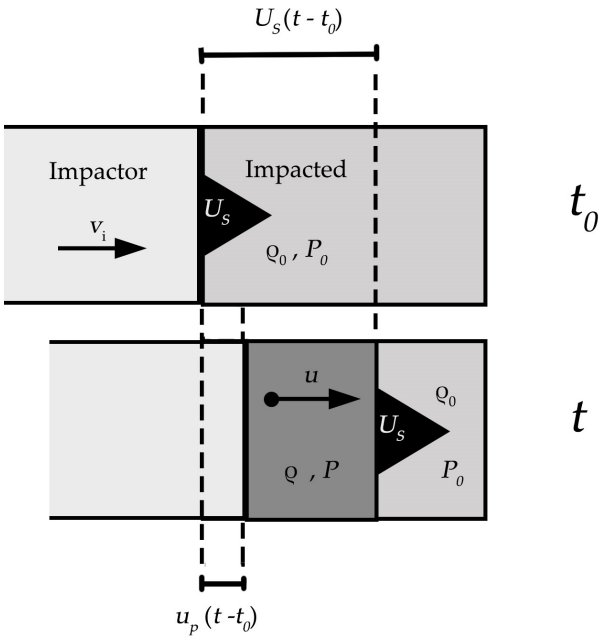

Figure 1.1: Schematic representation showing the interaction between impactor and impacted bodies during the first contact (t_0) and after a time t.

In this case, shock waves propagate through both the impactor and impacted bodies, causing a sharp rise (or pulse) in pressure and temperature experienced by both. The basics of the mechanism behind the generation of pressure through a shock event can be described with a schematic representation (Figure 1.1). When an impactor and the impacted objects get in contact (t_0), a shock wave is generated. A shock wave propagating with velocity U_s induces a migration of the impacted surface with a velocity u_p (also known as particle velocity). After a time t, the distance covered by the shock wave is $U_s \cdot (t - t_0)$, while the resulting migration of the impact surface can be quantified as $u_p \cdot (t - t_0)$. The states reached by a certain material under a single shock event are described by the Hugoniot curve. Hugoniot curves are calculated using the Rankine-Hugoniot equations, that relate the shock pressure (P) to the shock wave and particle velocities (U_s and u, respectively), and density ρ:

$$P - P_0 = \rho_0 \cdot u_p \cdot U_s \tag{1.1}$$

In addition, if the material does not show any phase tranformation, it is possible to use the empirical linear relation between U_s and u_p, that includes an approximation of the bulk velocity at ambient pressure (C_0), and the term $S = (1 + \gamma)/2$, where γ is the Grüneisen parameter (Melosh, 1989, 2013; Osinski and Pierazzo, 2013; Poirier, 2000):

$$U_s = (C_0 + S \cdot u_p) \qquad with \quad \gamma = \alpha \cdot K_T \cdot \frac{V}{c_V} \tag{1.2}$$

where α is the thermal expansion, K_T is the isothermal bulk modulus, V is the volume, and c_V is the specific heat capacity. Therefore, by combining Equation 1.2 with Equation 1.1, the Rankine-Hugoniot equation can be expressed as:

$$P - P_0 = \rho_0 \cdot u_p \cdot (C_0 + S \cdot u_p) \tag{1.3}$$

After shock compression, rarefaction waves induce an adiabatic release of the compression state, and bring the shocked objects back to ambient pressure. The duration of the pressure pulse (t_{pp}) therefore can be described as the sum between the time that a shock wave takes to travel through the material (t_i), and the time that a rarefaction wave takes to release the pressure (t_r):

$$t_{pp} = t_i + t_r \tag{1.4}$$

This can be further expanded in terms of impactor size (assuming a spherical impactor with diameter D, and density ρ_0), shock and rarefaction wave velocities, U_s and U_r, respectively, and the density under shock compression ρ (Melosh, 1989, 2013; Osinski and

Pierazzo, 2013):

$$t_{pp} = \frac{D}{U_s} + \left(\frac{\rho_0}{\rho}\right) \cdot \left(\frac{D}{U_r}\right) \tag{1.5}$$

Accordingly to the Murnaghan equation, rarefaction wave velocity U_r can be expressed as (Melosh, 1989, 2013; Osinski and Pierazzo, 2013):

$$U_r = \sqrt{\frac{\rho_0 \cdot C_0^2 + (4 \cdot S - 1) \cdot P}{\rho}} \tag{1.6}$$

and the shock pressure P as (Dai et al., 1997):

$$P = \frac{\rho_0 \cdot C_0^2 \cdot (1 - \rho_0 \,/\, \rho)}{\left[1 - S \cdot (1 - \rho_0 \,/\, \rho)\right]^2} \tag{1.7}$$

Contrary to static compression, shock compression is not an isothermal process, and therefore it has a thermal component that exposes the material to an increase of temperature during the shock event. The shock temperature induced by the impact can be obtained by numerical integration of the equation (Langenhorst and Hornemann, 2005):

$$dT = \frac{V_0 - V}{2 \cdot C_V} dP + \left(\frac{P - P_0}{2 \cdot C_V} - T \cdot \frac{\gamma}{V}\right) dV \tag{1.8}$$

where C_V is the molar heat capacity, T is the temperature along the Hugoniot curve, and V is the volume.

It is clear from Equation 1.7 that by knowing the shock pressure P, it is possible to have an estimate of ρ and obtain the kinematic parameter U_r (Equation 1.6), and therefore the size of the impactor object (Equation 1.5). In addition, impact velocity v_i can be approximated as $v_i = 2 \cdot u_p$ (Langenhorst and Hornemann, 2005).

During an impact, the shock event can leave a record in terms of microtextures and mineralogical transformations in the shocked material. Through a comparison with phase relations defined by static high-pressure experiments, shock-induced mineralogical transformations can be used to constrain shock pressures and temperatures. This information can be further used for the interpretation of the kinetics behind impact events.

While shock-induced features have been extesinvely studied on different meteorites, e.g., Chen et al. (1996, 1998, 2004); Miyahara et al. (2011, 2013, 2016); Ozawa et al. (2009)., the description of high pressure minerals in lunar rocks is limited to the single case of stishovite, which was found in the Apollo Section 15299,200 (Kaneko et al., 2015), hampering our understanding of the behavior of the lunar regolith during shock compression. Part of this thesis will focus on the characterization of shock-induced features in the Apollo Section 15299,247 (Figure 1.2). This section was extracted from the same sample (Apollo

Sample 15299) from which the section studied by Kaneko et al. (2015) was obtained.

1.1.2 Apollo Sample 15299

Subsection 1.1.1 emphasized how the study of shock-induced microtextures and mineralogical transformations could address the open questions regarding the collisional history of the Moon (Section 1.1). A brief description of the lunar sample investigated for this thesis will be provided in the following. This sample was provided by the NASA Johnson Space Center to Tomoko Arai[1].

The main goal of the Apollo 15 mission was to explore and sample the terrains in the Hadley-Appenine region, close to the edge of the Imbrium basin (Swann et al., 1972). Almost 80 kg of lunar samples (rocks and soil) were brought back to Earth by the astronauts[2] (Hiesinger and Head, 2006), mainly consisting of volcanic rocks and lunar breccias (Dowty et al., 1973; McKay et al., 1989).

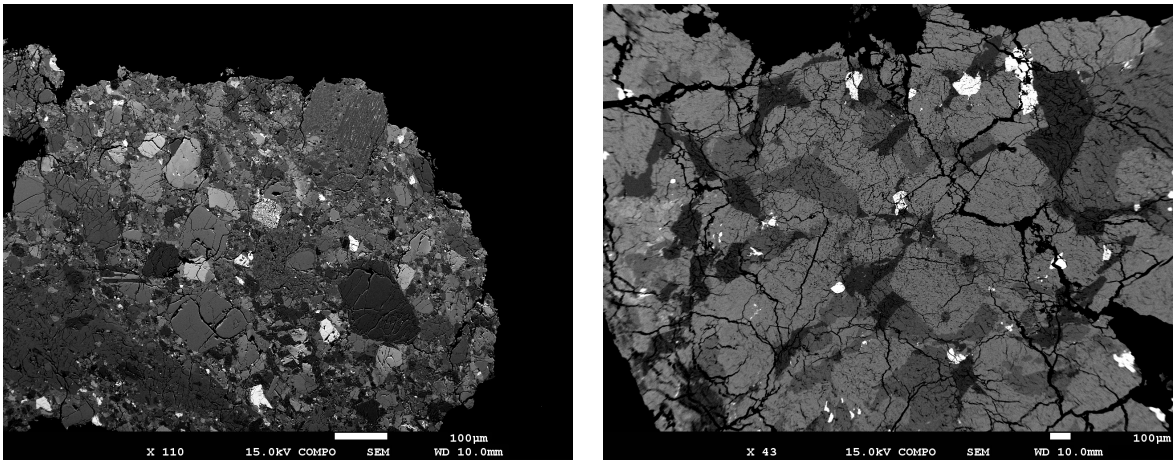

(a) (b)

Figure 1.2: Back-scattered electron images of the breccia (a) and basaltic clast (b) lithological domains in the Apollo Section 15299,247.

The Apollo section 15299,247 shows the typical aspects of an impact melt breccia, and in particular is constituted by two main and distinct lithological domains (Figure 1.2). A small fraction (~20 vol%) of the section is a polymictic breccia with small angular fragments (~100 µm ∅) of olivine, pyroxene, anorthitic plagioclase, silica, and ilmenite, embedded in a glassy matrix. The remaining portion is constituted by a large clast of a

[1]Planetary Exploration Research Center, Chiba Institute of Technology, Chiba 275-0016, Japan. Email: tomoko.arai@it-chiba.ac.jp

[2]David R. Scott, Commander; James B. Irwin, Lunar Module Pilot; Alfred M. Worden, Command Module Pilot

low-Ti basaltic rock with large (up to 500 µm ∅) pyroxene and anorthitic plagioclase. In this clast, olivine is present only in minor quantities, while oxides, such as chromite and ilmenite, appear only as accessory components. Shock-induced features, such as shock-melt veins and pockets are present in both domains.
In Chapter 4, the characterization of high-pressure minerals contained in a shock-melt pocket of the Apollo Section 15299,247 is described. These observations allowed us to estimate the pressure-temperature conditions experienced during shock compression by this lunar regolith sample. In addition, I show how this information was used to provide new insights on the Moon's collisional history.

1.2 Water in the Earth's Interior

1.2.1 Origin and Distribution

The origin of the terrestrial water has puzzled researches for decades. Until recently, comets were thought to have played a key role in the delivery of water to Earth, with what is generally described as the *Late Veneer* scenario (Chyba, 1990, 1991; Owen and Bar-Nun, 1995). However, isotopic evidences, such as oxygen (Greenwood et al., 2018), and in particular the very high cometary D/H ratio (Bockelée-Morvan et al., 2004; Altwegg et al., 2015), which is roughly twice the one estimated for the oceanic water (Lécuyer et al., 1998), suggest that the late accretion of material had a limited contribution to the current water budget of the Earth. Presently, there are several dynamic models that attempt to uncover the origin of water (O'Brien et al., 2018). The most promising ones offer a scenario in which the forming Earth had his feeding zone in the Inner Solar System, i.e. the region between the Sun and Jupiter's orbit (Namouni et al., 1996; Weidenschilling et al., 1997). Here, elevated nebular temperatures, combined with the low condensation temperature of hydrogen, would have inhibited the condensation of water. Therefore, the forming early-Earth would have accreted relatively dry [Morbidelli et al. (2000); Dauphas (2017) and references therein], a solution that is also capable of reconceiling geochemical costrains (Clayton et al., 1984; Dauphas et al., 2002). Finally, the Earth would have received the delivery of most of its present mass of water during its later stage of formation by carbonaceous-chondiritic planetesimals (Alexander et al., 2012; Marty, 2012; Schlichting et al., 2015), as they migrated sunward as result of inward-then-outward migration of Jupiter (Walsh et al., 2011).
The current distribution of water in the Earth in the result of a continuous exchanges of material between the surface and Earth's deep interior. Plate tectonics control this material exchange, forming new oceanic lithosphere along the mid-oceanic ridges, and the

sinking (c)old lithospheric material in subduction zones.

After being formed, the oceanic lithosphere is subjected to a wide spectrum of metamorphic reactions resulting from the interaction with sea water. Petrographic analyses of ophiolitic sequences (i.e. obducted oceanic lithosphere fragments), provided the first constrains on the complex composition and structure of the oceanic lithosphere (Dilek and Furnes, 2014). Over time, direct evidences (Alt et al., 1986; Ildefonse et al., 2007; Michibayashi et al., 2007) and experimental studies (Janecky and Seyfried, 1986) have shown that the oceanic lithosphere can contain a relatively large amount of water stored in hydrous minerals. Serpentinization reactions constitute the most prevalent and efficient processes with which the oceanic lithosphere incorporates water, and are described as the alteration of ferromagnesian silicates such as olivine and pyroxenes to form serpentine group minerals, together with other hydrous minerals such as brucite and talc:

$$\begin{array}{ccccccc} MgSiO_3 & + & Mg_2SiO_4 & + & 2H_2O & \rightarrow & Mg_3Si_2O_5(OH)_4 \\ \text{pyroxene} & + & \text{olivine} & + & \text{water} & \rightarrow & \text{serpentine} \end{array}$$

$$\begin{array}{ccccccc} 2Mg_2SiO_4 & + & 3H_2O & \rightarrow & Mg_3Si_2O_5(OH)_4 & + & Mg(OH)_2 \\ \text{olivine} & + & \text{water} & \rightarrow & \text{serpentine} & + & \text{brucite} \end{array}$$

$$\begin{array}{ccccccc} 6MgSiO_3 & + & 3H_2O & \rightarrow & Mg_3Si_2O_5(OH)_4 & + & Mg_3Si_4O_{10}(OH)_2 \\ \text{pyroxene} & + & \text{water} & \rightarrow & \text{serpentine} & + & \text{talc} \end{array}$$

During subduction, serpentine minerals are predicted to break down as a result of the rising temperature, causing fluid migrations into the overlying mantle wedge, possibly inducing melt formation (Schmidt and Poli, 1998; Ulmer and Trommsdorff, 1995), as well as triggering deep earthquakes within the subduction zone (Campione and Capitani, 2013; Hacker et al., 2003; Jung et al., 2004). Along a cold geotherm, however, a fraction of the water may be preserved through the formation of Dense Hydrous Magnesium Silicates (DHMS), and subsequently transferred to larger depths (Irifune et al., 1998; Litasov and Ohtani, 2007; Ohtani, 2005; Faccenda, 2014). Experiments on hydrous peridotites and harzburgites have suggested a mechanism capable of delivering water via DHMS to the Earth's lower mantle (Frost, 1999; Ohtani et al., 2004). The peridotitic fraction of a slab can store a substantial fraction of water as serpentine minerals. Antigorite, the high-pressure polymorph of serpentine, contains up to 13 wt% of water. Antigorite has been shown to dehydrate at 6 GPa and 600 °C, producing an assemblage of harzburgitic composition capable of retaining (ideally) almost 4 wt% of the initial antigorite water budget in phase A, while the rest is dissolved as free fluid or in melts (Ulmer and Trommsdorff,

1995; Litasov and Ohtani, 2007). Experiments on hydrous natural harzburgite have shown phase A to be stable at 10 GPa and 900 °C (Frost, 1999).

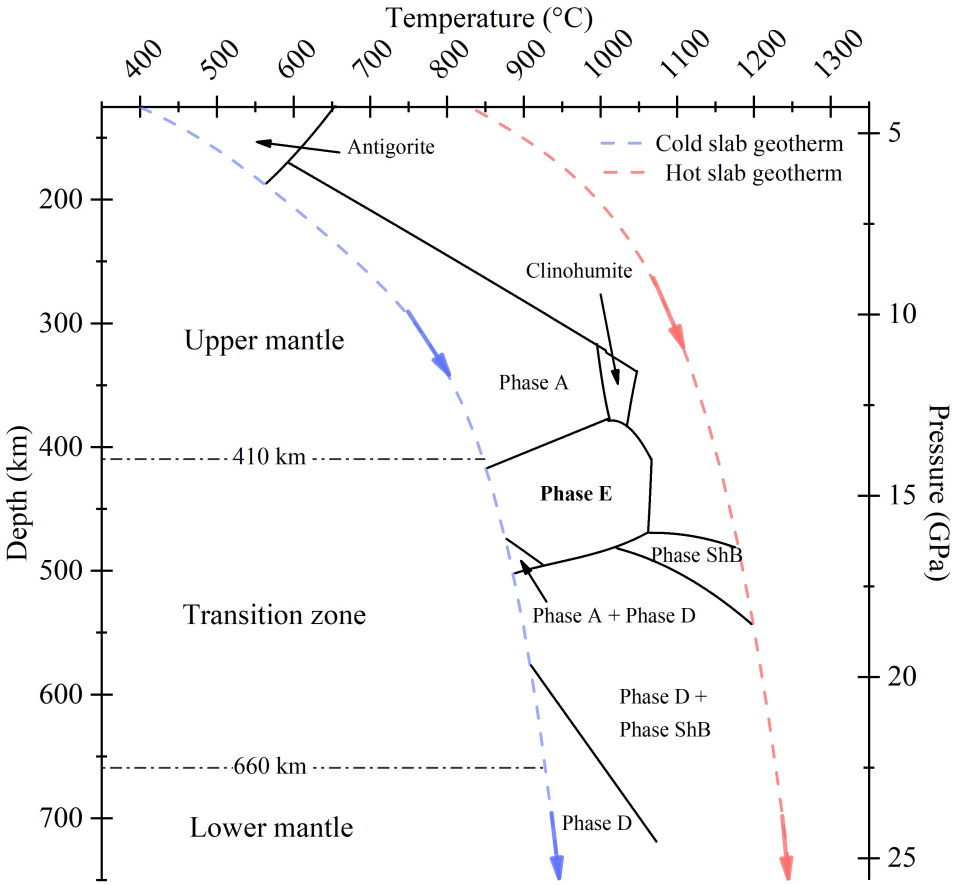

Figure 1.3: Dense Hydrous Magnesium Silicates in possible subduction contexts. Stability fields result by a series of experiments in the MgO-SiO_2- H_2O system. A detailed summary of these experimental results is reported in Frost (1999). Geotherms are from Thompson (1992).

In addition, phase A was found to coexist with phase E at ∼13 GPa and 1000 °C in the experimental studies using Mg_2SiO_4 plus 20 wt% H_2O as starting material (Kanzaki, 1991). In the experiments on hydrous harzburgitic samples, phase E has been found to occur in combination with wadsleyite at pressure and temperature conditions comparable to a cold geotherm in the transition zone (Frost, 1999). Above 16 GPa, the phase E-bearing assemblage may react to form superhydrous phase B along with ringwoodite and stishovite, possibly delivering water to the uppermost lower mantle. Moreoever, phase D has been found to be stable at lower mantle pressures and temperatures (Pamato et al., 2015), indicating that it can play a role in the stabilization of water in the deepest portion of the Earth's mantle (Figure 1.3).

In addition to the water stored in the peridotitic portion of subducting slabs, the basaltic

crust and hydrous sediments can also play a role in the delivery of water to the lower mantle. Thus, a chain of reactions ending with solid solutions of δ-AlOOH, ε-FeOOH and phase H, has been suggested as an efficient transport mechanism of water (Sano et al., 2004; Duan et al., 2018; Liu et al., 2019; Nishi et al., 2019), bringing important confirmations to the role that Al-bearing hydrous phases may have in the stabilization of water in the Earth's lower mantle (Nishi et al., 2014; Pamato et al., 2015). Geodynamical simulations such as Brandenburg and van Keken (2007), supported by seismological observations (Fukao and Obayashi, 2013; Hutko et al., 2006) and geochemical evidences (Van Keken et al., 2002), indicate that slabs can pass through the transition zone and enter the Earth's lower mantle. However, the hydration state of subducting slabs is debated, limiting our understanding about the physical processes that characterize subduction events.

1.2.2 Mapping Water at Depth

Seismology pictures the Earth's subsurface by studying earthquakes and related propagation of seismic waves in the Earth's interior. Earthquakes are, in their simplest form, impulsive and intense loadings that generate seismic waves that propagate throughout the Earth's Interior. In a first approximation, i.e. without taking into account any influences related to inelastic contribution (Karato, 2008), the propagation velocity of seismic waves depend on the elastic response (quantified by the bulk K and shear G moduli), and density (ρ) of the materials of the Earth's interior, where in the case of isotropic conditions (Poirier, 2000):

$$v_P = \sqrt{\frac{K + \frac{4}{3} \cdot G}{\rho}} \tag{1.9}$$

$$v_S = \sqrt{\frac{G}{\rho}} \tag{1.10}$$

Equation 1.9 and Equation 1.10 imply that it is possible to predict the propagation velocity of seismic waves if the elastic response of the constituents of the Earth's interior is known, and vice versa. In addition, since seismic velocities are affected by phase transitions and chemical variations (Birch, 1952), the combination of seismological observations and laboratory data has been used to understand the composition of the Earth's interior (Anderson et al., 1969), eventually leading to more complex evaluations such as its hydration state, e.g., Buchen et al. (2018) and Schulze et al. (2018). Nowadays, seismological tools such as seismic tomography are capable of performing high-resolution investigations, and image the behavior of seismic waves in a three-dimensional space. In particular, seismic tomography has been successfully used to investigate subduction contexts, revealing important aspects of the subduction geometries and their relation to arc magmatism, vol-

canism and seismicity (Zhao, 2015). However, our current knowledge on elastic properties of hydrous phases likely present in slabs is limited, hampering an accurate estimation of the hydration state of slabs during subduction through seismological observation (Mainprice and Ildefonse, 2009). Therefore, laboratory elasticity measurements on candidate hydrous phases in relevant pressure-temperature-composition space become necessary to put tighter constrains on the interpretation of seismic heterogeneities of subducting slabs in terms of depth, temperature and hydration state.
This thesis will focus on using an experimental approach to explore the elastic behavior of two water carriers, Phase E and δ-(Al,Fe)OOH. In the following, both phases will be introduced in terms of stability fields, structural aspects and their relation to the elastic properties.

1.2.3 Phase E

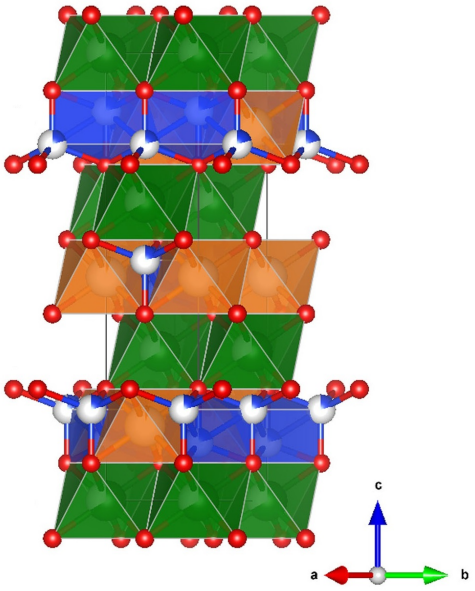

Figure 1.4: Structural model of phase E. Green octahedra belong to brucite-like sheets. Interlayered octahedra and tetrahedra are shown in orange and blue, respectively. White spheres represent cation sites, which in phase E are only partially occupatied. Oxygens in red. Structural data for this model were taken from Kudoh et al. (1993).

Among all the DHMS phases, phase E $Mg_{2.08}Si_{1.16}O_{2.8}(OH)_{3.2}$ has been found to be stable at relatively high temperatures (1200°C at 13.5 GPa) (Komabayashi et al., 2005). Phase E crystallizes in the trigonal system (space group $R\bar{3}m$). Its crystal structure (Figure 1.4) is constituted by parallel brucite-like sheets of octahedra, stacked along the c-axis (Kudoh et al., 1993). Brucite-like layers are cross-linked by interlayered octahedra and tetrahedra, and hydrogen bonds (Tomioka et al., 2016). Interlaying octahedra and tetrahedra

are connected to the brucite-like layers via shared edges and corners, respectively. The relations between intra- and inter-layer polyhedra lead to complex cation vacancies localized in the brucite-like layers that do not follow any long-range ordering (Kudoh et al., 1993). These structural aspects make phase E a non-stoichiometric phase, with variable chemical composition and density, but more importantly allow the stabilization of up to ~19 wt% H_2O in its crystal structure (Crichton and Ross, 2000). High-pressure diffraction on Fe-bearing phase E single-crystals showed that it is the DHMS with both the lowest bulk modulus, K_{T0} = 92.9(7) GPa, and the lowest density (ρ = 2.84 g cm^{-3}) at room conditions (Crichton and Ross, 2000). In addition, the pressure derivative of the bulk modulus is relatively high K'_{T0} = 7.3(2). Compared to San Carlos olivine (Zha et al., 1998), phase E differs especially in K_{T0} and its pressure derivative, which are ~30% lower and ~80% higher, respectively. This difference makes phase E an ideal candidate to be detectable by seismological investigations with the perspective of mapping water. Most of the single-crystal elastic properties of DHMS, such as phase A (Sanchez-Valle et al., 2006, 2008), superhydrous phase B (Pacalo and Weidner, 1996; Rosa et al., 2015) and phase D (Liu et al., 2004; Rosa et al., 2012) have been investigated experimentally. On the other hand, a full description of phase E elasticity is missing. For this reason, part of this thesis focuses on constraining the single-crystal elastic properties of phase E by Brillouin spectroscopy and X-ray diffraction. In Chapter 5, the full elastic tensor of phase E is provided, and the possible role that this hydrous phase has in the detection of water at depth is discussed.

1.2.4 δ-(Al,Fe)OOH

The wide stability field in terms of pressures and temperatures (Ohtani et al., 2001; Sano-Furukawa et al., 2008; Nishi et al., 2017), as well as the large compositional range (Kawazoe et al., 2017; Xu et al., 2019) of the solid solution between aluminum and iron oxy-hydroxide (δ-AlOOH and ε-FeOOH), makes these compounds ideal candidates for storing water in the Earth's lower mantle (Duan et al., 2018; Liu et al., 2019; Nishi et al., 2019).

δ and ε oxy-hydroxides adopt a $CaCl_2$-type structure (space group $P2_1nm$) with columns of edge-sharing octahedra stacked along the c-axis, and connected along the a- and b-axes through corners (Figure 1.5). Each octahedron is coordinated by a hydroxide and 5 oxygens, leading to the formation of hydrogen bonds in the basal plane (**a**-**b** plane). In the aluminum end-member and in samples belonging to the δ-(Al,Fe)OOH solid solution, it has been shown that pressure induces a transformation toward higher symmetry ($P2_1nm$ → $Pnnm$) between 8 and 10 GPa by inducing a reduction in the O···O distance (Kuribayashi et al., 2014; Sano-Furukawa et al., 2009, 2018; Ohira et al., 2019). The $P2_1nm$ to

Pnnm transition results in an abrupt change of the a and b axial compressibilities that, according to Sano-Furukawa et al. (2018), is related to a disordered configuration of the hydrogen between two equivalent sites across the O···O in the **a-b** plane. This suggests that the disordered hydrogen configuration may be a precursor of the symmetrization of the hydrogen bonds (Figure 1.5), which has been constrained to be completed between 15-18 GPa by experimental (Sano-Furukawa et al., 2018) and theoretical investigations (Cortona, 2017; Pillai et al., 2018).

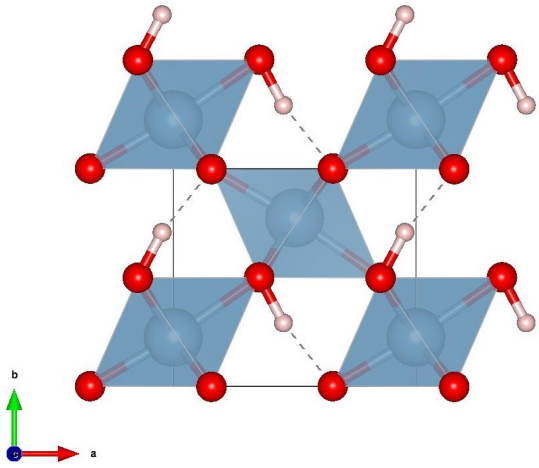

(a) $P2_1nm$ - Asymmetric hydrogen

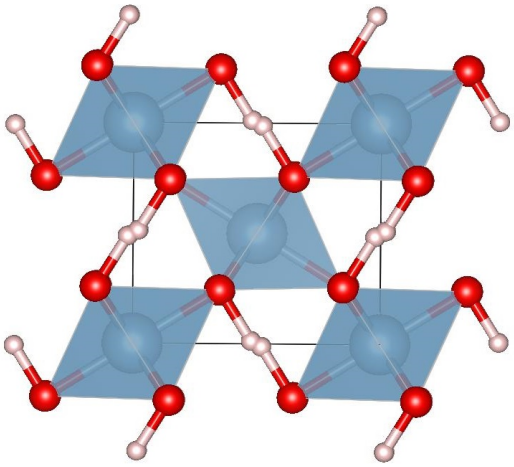

(b) *Pnnm* - Disordered hydrogen

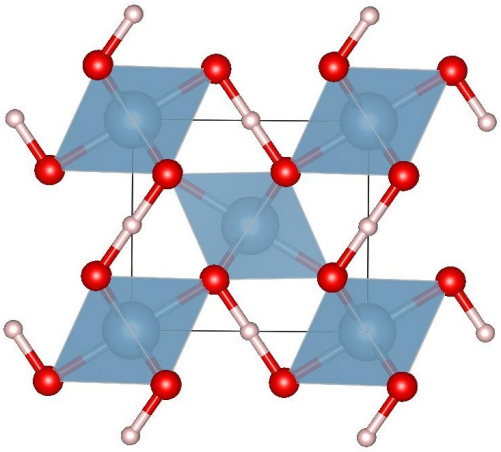

(c) *Pnnm* - Symmetric hydrogen

Figure 1.5: Structural models of δ-Al,OOH at ambient conditions (a), at 9.5 GPa (b), and 18 GPa (c). Atomic coordinates of (b) and (c) are based on Sano-Furukawa et al. (2018). Al atoms sit in the center of the blue octahedra. Oxygen and hydrogen are in red and pink, respectively.

Currently, the elastic tensors of the low- and high-symmetry polymorphs of δ-AlOOH

have been constrained only by theoretical investigations (Tsuchiya and Tsuchiya, 2009; Cortona, 2017; Pillai et al., 2018), limiting our understanding of the effect that the $P2_1nm$ to $Pnnm$ transition has on the elastic properties of this hydrous phase. Understanding the pressure-induced hydrogen bond evolution and its effects on the elastic properties of δ-AlOOH is important, as it provides constrains for other phases expected to undergo hydrogen symmetrization, such as H_2O ice VII (Meier et al., 2018), and Al-rich phase D (Pamato et al., 2015). For this reason, part of this thesis focuses on the characterization of the $P2_1nm$-$Pnnm$ transition in δ-AlOOH. In Chapter 6, I provide the elastic tensors of the $P2_1nm$ and $Pnnm$ structures of Fe-bearing δ-AlOOH, which were constrained experimentally by simultaneous single-crystal high-pressure X-rays and Brillouin spectroscopy measurements.

2 Methods

This study used different techniques to investigate specific aspects of the samples of interest. This chapter summarizes all the tools employed in this work. Basics of the physical principles behind each technique used are presented together with technical aspects and details on the experimental strategies followed. Textbooks and review articles are referenced in each section in order to provide further details.
The first section includes the techniques employed for the synthesis and chemical characterization of the samples investigated. In the second section, the selection routine of the samples used for high-pressure experiments is presented. In addition, specifics of the technical and operational aspects on the technology used to achieve high-pressure conditions are included. The third section aims to outline the techniques employed for the high-pressure characterization of the elastic properties of the material this study focuses on. Since this section covers central aspects of the present thesis, the theoretical background, as well as the physical and operating principles are treated more in details. The fourth section includes a description of the techniques used during a six month project carried out at Tohoku University in Sendai (Japan). This project is the result of a collaboration between the Bayerisches Geoinstitut (University of Bayreuth, Germany) and the Department of Earth Science at the Tohoku University (Japan), as part of the "Deep Earth Volatile Cycles" International Research and Training Group[1].

[1] http://www.deepearthvolatiles.de/

2.1 Characterization of Shock-Induced Textural and Mineralogical Features

2.1.1 Scanning Electron Microscopy

The Scanning Electron Microscope (SEM) uses a focused and accelerated electron beam to conduct chemical and morphological studies. In particular, it exploits the elastic and inelastic interactions between a focused and accelerated electron beam, and the atoms that constitute the sample. Elastically (back-scattered) and inelastically scattered (secondary) electrons can be used to qualitatively determine elemental distributions, and to imagine morphological aspects, respectively. In addition, elemental concentrations in the sample can be obtained through Energy Dispersive X-ray Spectrometry (EDS) measurements (Newbury and Ritchie, 2013). An introduction to this technique can be found in Reed (2005). Because of the possibilities of capturing high-resolution images and doing EDS analyses, the SEM-EDS system constitutes a perfect tool to explore the shock-induced features in shocked samples, such as meteorites and lunar regolith breccia.
The shock-induced textural aspects present in the Apollo section 15299,247 were studied in back-scattered mode using a JEOL[2] JSM-7000F installed at the Department of Earth Science of the Tohoku University (Sendai, Japan). In addition, the same system was used to determine elemental concentrations in mineral components using EDS analyses. For these SEM studies, the Apollo section 15299,247 was coated with a deposition of a thin film of carbon (coating thickness 15 nm). The SEM system was operated with an accelerating potential of 15 kV. Areal and point EDS analyses were done with a working distance of 10 mm. Both working distance and beam current were calibrated using a cobalt standard. Calibration, imaging, and EDS analyses were performed using the software AZtec™ [3]. Detailed observation at high-magnification ($>$ x6000) were done using a shorter working distance (6.7 mm) with the aim of improving the spatial resolution (Figure 2.1). Results are illustrated in Chapter 4.

[2]JEOL Ltd., Tokyo, Japan.
[3]Oxford Diffraction Ltd., Yarnton, Oxfordshire, United Kingdom.

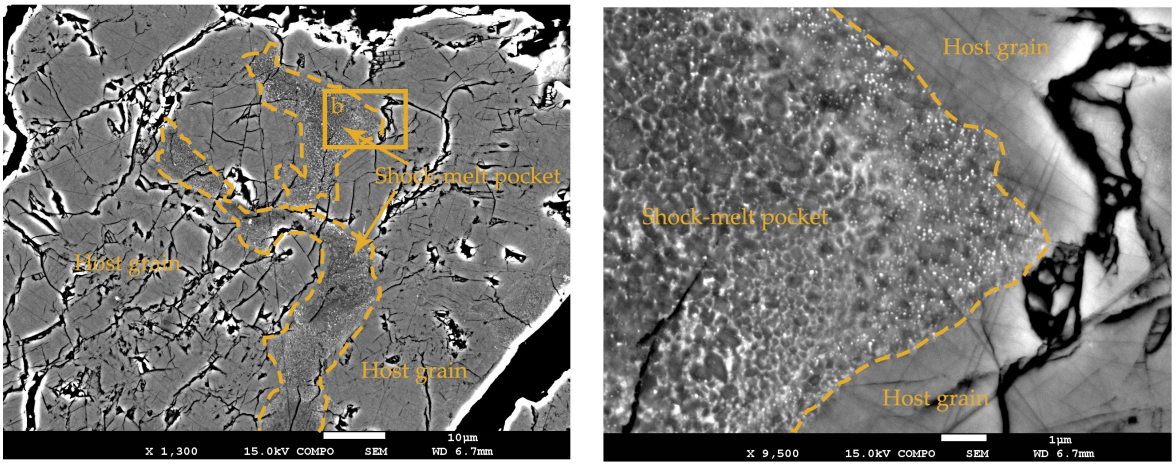

(a) (b)

Figure 2.1: Back-scattered electron images of a shock-melt pocket at low (a) and high (b) magnifications. Mustard rectangle in (a) shows the location of (b).

2.1.2 Transmission Electron Microscopy

Transmission Electron Microscopy (TEM) is a microscopic technique that operates by accelerating a monochromatic beam of electrons with very high potential (up to 300 kV), so that can it be transmitted through a very thin sample (∼100 nm). Focusing of the electron beam on the sample results in different interactions that can be used for imaging with nanometer resolution, but also to obtain information on the crystalline structure and chemical composition of the sample studied. Thus, the accelerated electron beam can be diffracted by the sample by following Bragg's law (see Subsection 2.4.2). Therefore, electron diffraction can be used to acquire diffraction pattern and the crystal structure of the sample. In addition, the electron beam can induce the emission of characteristic X-rays from the sample, which can be analyzed with EDS (see Subsection 2.1.1) to assess elemental composition. A detailed introduction to this technique, including specifics on its operational principles and possible applications can be found Williams and Carter (1996).

In this study, a JEOL[2] 2100F TEM (installed at the Department of Civil Engineering and Architecture at Tohoku University, and operated by Masaaki Miyahara[4]), was used to characterize mineralogical assemblages confined in a shock-melt pocket of the Apollo Section 15299,247. The preparation of the lamellae used in the TEM investigation was done with an FEI[5] Quanta 200 3D (installed at the Electron Microscopy Center at To-

[4]Department of Earth and Planetary Systems Science, Graduate School of Science, Hiroshima University, Higashi-Hiroshima 739-8526, Japan. Email: miyahara@hiroshima-u.ac.jp.
[5]FEI Technologies Inc., Hillsboro, Oregon, USA.

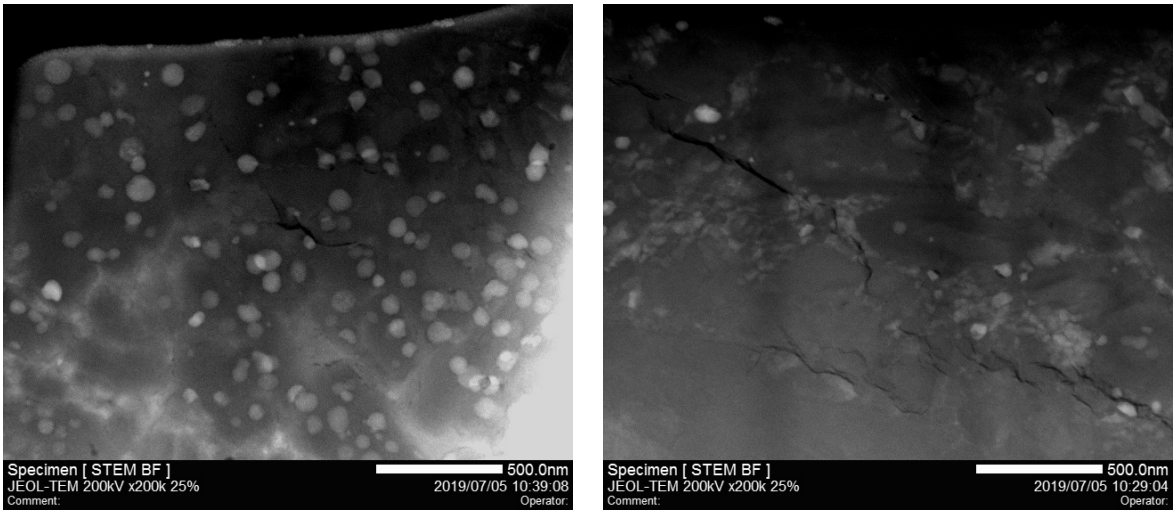

(a) (b)

Figure 2.2: HAADF images showing textural and mineralogical details of shock-induced features contained in the TEM lamella extracted by the Apollo section 15299,247.

hoku University, Sendai, Japan, and operated by Masahiko Nishijima[6]). In this process, a low-current Ga^+ beam was accellerated with a potential of 30 kV, and focused on the Apollo section 15299,247. Both the camera-length and wavelength of the electron beam were calibrated using a gold particle standard. Sample surfaces exposed by the lamella are perpendicular to the polished surface pictured by the SEM, and therefore, allow to image the sample from a different angular perspective. In this study, this was crucial, as it allowed us to expose shock-induced features, including their textural and mineralogical details. TEM lamella was imaged on the nano-meter scale using the High-Angle Annular Dark-Field (HAADF) (Pennycook and Jesson, 1990) imaging technique (Figure 2.2) using the TEM in scanning mode (STEM mode). This incoherent-imaging technique limits the contribution of scattered electrons to the image, and has a contrast which depends on the atomic number Z (i.e., the *Z-contrast*). Subsequently, structural aspects of the mineralogical components were investigated with Selected Area Electron Diffraction (SAED) analyses. In Selected Area Electron Diffraction (SAED), a metal pinhole is used to limit size of the electron beam.

This has the advantage that only a specific area of the lamella is probed with the electron beam. This has been crucial for collecting diffraction patterns of crystals with a size in the order of tens of nm, as for example, the bright spherules in Figure 2.2. As any other two-dimensional diffraction pattern, an SAED pattern (Figure 2.3) can be used to quantify interplanar spacings (d_{hkl}) along different plane directions *hkl*. By taking into

[6]The Electron Microscopy Center, Tohoku University, Sendai 980-8577, Japan.
Email: m.nishijima@mac.com.

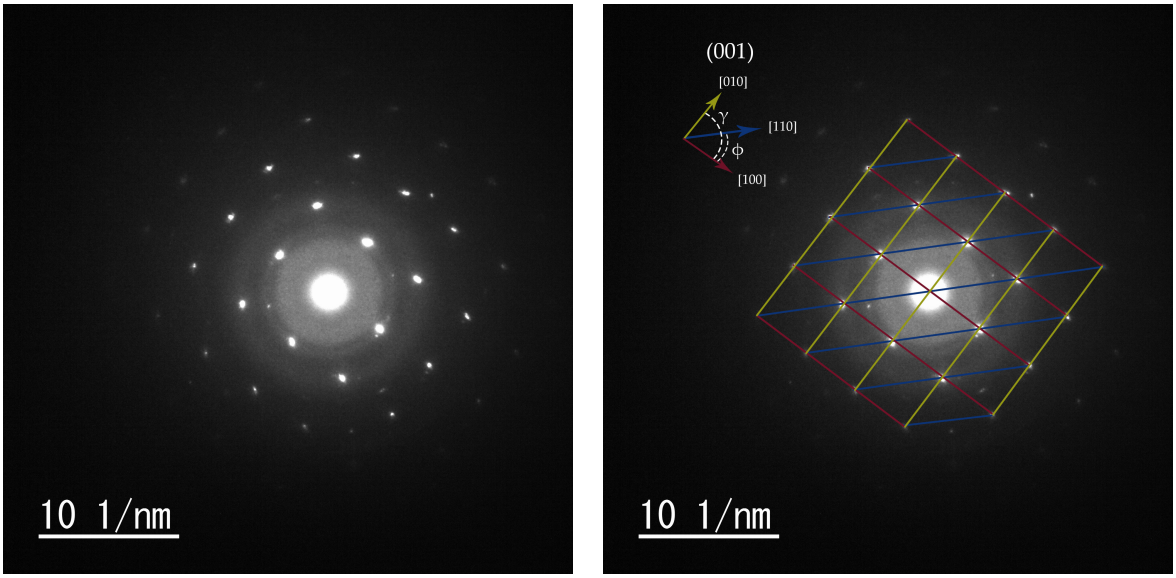

(a) (b)

Figure 2.3: Original (a) and edited (b) two-dimensional lattice image showing three distinct *hkl* lines and their angular relations. Rings in the background arise from the contribution of an amorphous component. γ (90°) shows the angular relation between the yellow arrow (plane direction *010*) and the red arrow (plane direction *100*). The blue arrow lies along the bisector of the γ (90°), i.e. $\phi = 45°$.

account the angular relation between different plane directions *hkl*, and the interplanar d-spacing between reflections from the same line (d_{hkl}), *hkl* reflections can be indexed. For example, Figure 2.3 shows a ferropericlase diffraction pattern. In this case, d_{hkl} were measured along three different lines, showing different angular relations (ϕ and γ), in the (001) plane. Being cubic, the relation that links the unit-cell parameter of ferropericlase (a) to the d_{hkl} associated with *hkl* reflection indices, is described by the equation:

$$d_{hkl} = \frac{a}{\sqrt{h^2 + k^2 + l^2}} \tag{2.1}$$

Different equations can be used depending on the crystal systems involved (Giacovazzo et al., 2011). A comprehensive description of the SAED results can be found in Chapter 4. The chemical characterization was done in STEM-mode using EDS. In this analysis, different single mineralogical components, as well as the bulk material, have been chemically characterized. Furthermore, elemental mapping (Figure 2.4) was performed, and used to evaluate the partitioning behavior of different chemical elements within the shock-induced features. Elemental concentrations were calculated using experimentally determined Cliff-Lorimer factors (Cliff and Lorimer, 1975).

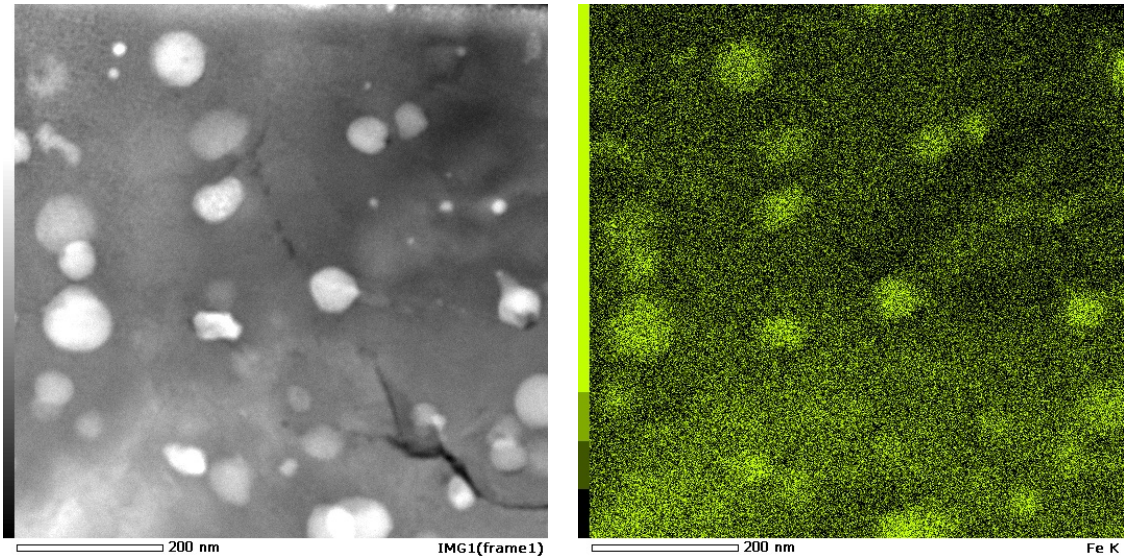

(a) Back-scattered image. (b) Iron.

Figure 2.4: Elemental mapping in EDS mode.

2.2 Synthesis of Large Single crystals and their Chemical Characterization

2.2.1 Multi-Anvil Technique and Sample Synthesis

Kawai-type multi-anvil apparatus are routinely used to subject a large volume of samples (up to cm^3) to pressures and temperatures representative of the deepest portion of Earth's mantle. The concept behind the operation of a multi-anvil apparatus relies on the relation $P = F \ / \ A$, that links pressure (P) with force (F) and area (A). In particular, it uses a series of anvils to transfer a constant force onto gradually smaller anvil assemblies, thus reducing the area on which the constant force acts. Kawai-type multi-anvil apparatus employ a hydraulic press to generate an uniaxial force that applies on a set of six anvils, the so-called first-stage anvils. The first-stage anvils create a cubic volume which is filled by the second-stage anvils. The second-stage anvils are constituted by a set of eight cubes with truncated corners, and are used to transfer the force onto a smaller assembly of octahedral shape, called octahedron. The octahedron contains the capsule, in which the starting material is loaded, and has the role of transferring the pressure to the capsule in a quasi-hydrostatic regime. A resistance heater, thermal insulator and thermocapsules are inserted in the octahedron. These components allow the generation of heat, limit the heat dissipation, and provide a constant monitoring of the temperature within the capsule, respectively. Because of their capabilities in reaching high-pressure and high-temperature

conditions, the multi-anvil technique plays a key role in the synthesis of high-pressure phases, with a crystal size suitable for conventional characterization techniques. A more comprehensive description of multi-anvil apparatus, as well as a variety of applications of this technique, can be found elsewhere (Keppler and Frost, 2005).

Fe-bearing phase E $\delta-(Al,Fe)OOH$ crystals were synthesized employing a Hymag[7] (1000 tonnes) Kawai-type multi-anvil apparatus. Fe-bearing phase E synthesis used San Carlos olivine powder as starting material and a flux (liquid water) to enhance crystal growth. $\delta-(Al,Fe)OOH$ were synthesized in two distinct runs (H4765 and H4944). Both the H4765 and H4944 used a mixture of $Al(OH)_3$: Fe_2O_3 = 92.5 : 7.5 (mol) as starting material. In all the synthesis runs, starting materials were finely ground in an agate mortar prior to loading, and tungsten carbide cubes supported by pyrophyllite gaskets were used as second-stage anvil assembly. Octahedrons made of Cr_2O_3-doped MgO were employed as pressure-transmitting medium. Electrical heating was provided using a resistive $LaCrO_3$ heater surrounded by a ZrO_2 insulator. In addition, a MgO sleeve was placed between the metal capsule and the heater.

Table 2.1: Synthesis run details.

Run No.	**Fe-bearing Phase E** H4583[a]	**δ-(Al,Fe)OOH** H4765[b] & H4944
Starting material	San Carlos Olivine powder	$Al(OH)_3$ + Fe_2O_3
Fe/(Mg+Fe)	0.1	-
Fe/(Al+Fe)	-	0.075
Flux	liquid water	-
Set-up		
Configuration	18/11	10/4
Heater	$LaCrO_3$	$LaCrO_3$
Capsule	Pt	PtRh
Anvil	WC	WC
Synthesis conditions		
Pressure (GPa)	14	21
Temperature (°C)	1100	1150
Duration (h)	3	5

[a]prepared and conducted by Takaaki Kawazoe; [b]prepared and conducted by Takayuki Ishii.

All the three synthesis strategies were characterized by a first step in which the target pressure in the capsule was achieved using the hydraulic press to increase the force. Subsequently, electrical power was provided to the heater. The sample was heated until it

[7]Hymag GmbH, Germany.

reached the the target temperature, and then kept at constant pressure and temperature for a determined period of time. Quenching of the sample was done by cutting off the power supply to the electric resistance heater. Final decompression was performed over 15 h. Details on the assemblies and experimental conditions for each run are listed in Table 2.1. Synthesis run No. H4583 and H4765 were prepared and conducted by Takaaki Kawazoe[8] and Takayuki Ishii[9], respectively.

2.2.2 Electron Microprobe Analyses

The Electron Microprobe (EMP) is an analytical technique that uses an electron beam to induce the emission of characteristic X-rays from a sample, and uses them to constrain major and minor element concentrations of the sample. In particular, the EMP uses an accelerated electron beam focused on the target. The electron beam ionizes the inner shell electrons of the atoms constituting the sample, therefore producing vacancies in the inner shells. Consequently, outer shell electrons fills these vacancies in the inner shell while emitting X-ray radiation that is characteristic to each element (i.e., characteristic X-rays). In Wavelength Dispersive Spectromety (WDS) analyses, an analyzer crystal with determined interplanar spacing d is used to select specific wavelengths (λ) associated with characteristic X-rays, following Bragg's law (Bragg, 1914):

$$n \cdot \lambda = 2 \cdot d_{hkl} \cdot \sin\theta \tag{2.2}$$

where n is an integer, and θ the diffraction angle. Different planes are brought to diffraction through a rotation of the analyzer crystal, which concurs with a translation of the detector. Analyzer crystals with different interplanar spacings might be used to cover the entire wavelength range. Element concentrations can be estimated by comparing the intesity of the X-ray lines emitted by the sample, and those emitted from a standard of known composition. A matrix correction is necessary to have an accurate estimate of elemental concentrations in the analyzed region. An introduction to the physical principles of the EMP, quantitative analysis corrections, and their application in Geoscience can be found, for example in Reed (2005).

In this study, EMP analyses were performed on Fe-bearing phase E and δ-(Al,Fe)OOH to assess major and minor element concentrations. In addition, the quantification of the water content was estimated from the difference between the sum of the analyzed oxides and 100%.

[8]Now at: Department of Earth and Planetary Systems Science, Hiroshima University, Hiroshima 739-8526, Japan. Email: kawazoe@hiroshima-u.ac.jp.

[9]Bayerisches Geoinstitut, Universität Bayreuth, 95440 Bayreuth, Germany. Email: takayuki.ishii@uni-bayreuth.de.

Table 2.2: EMP analysis set-up. Ens = enstatite, Alm = almandine garnet, And = andradite garnet.

	Mg	**Si**	**Fe**	**Ni**	**Mn**	**Ca**	**Al**	**Cr**
Standard	Ens	Ens	Alm	Ni-metal	And	$MnTiO_3$	Alm	Cr-metal
Current (nA)	5	5	5	5	5	5	5	5
Voltage (kV)	15	15	15	15	15	15	15	15
Acquisition time (s)	10	10	10	10	10	10	10	10

Prior to being analyzed, selected grains of Fe-bearing phase E and δ-(Al,Fe)OOH were embedded in an epoxy resin, polished and carbon-coated with graphite particles (15 nm coating thickness). All the measurements were performed at the Bayerisches Geoinstitut using a JEOL[2] JXA-8200.

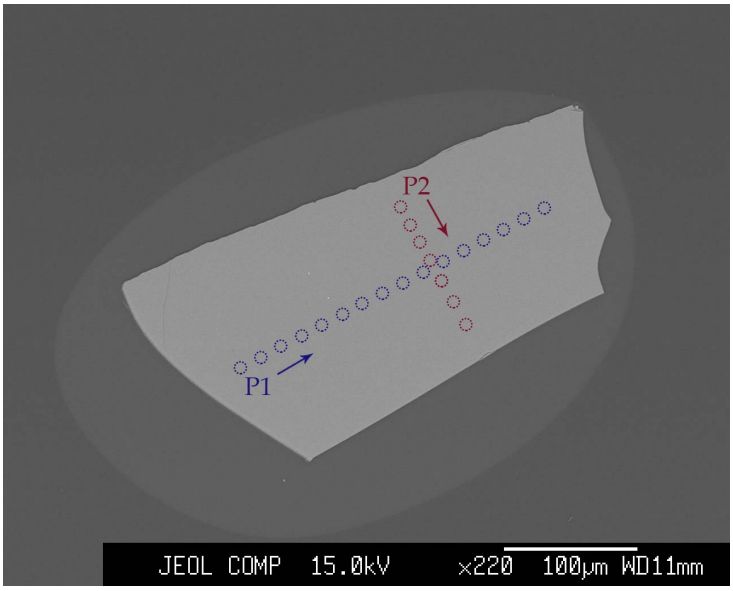

Figure 2.5: Back-scattered electron image of a phase E single crystal showing the experimental strategy followed for its chemical characterization. Measured areas in P1 and P2 profiles are represented by blue and red dotted circles, respectively.

Chemical analyses were run using a low current and defocused beam (10 µm ∅) to limit the loss of the volatile component. Furthermore, due to the natural origin of the starting material used to synthesize Fe-bearing phase E crystals (see Subsection 2.2.1), various elements expected to be only present in minor concentrations (<1 wt%) were included in the chemical analyses. On the other hand, only iron and aluminum concentrations were measured in δ-(Al,Fe)OOH grains. Various crystals from the same batch were analyzed within the same measurement session, in order to delineate possible chemical variations between grains from the same synthesis run. Analysis points were collected along perpen-

dicular profiles in order to investigate the elemental distributions within the same sample (Figure 2.5). A minimum of 10 analysis points were collected in each probed grain. The results obtained did not show any anomalous distribution of the element concentrations. Therefore, the final chemical composition, including water content, was determined by averaging the measured points. Detailed results of the chemical analyses performed on Fe-bearing phase E and δ-(Al,Fe)OOH are listed in Chapter 5 and Chapter 6, respectively.

2.3 Experiments with Diamond-Anvil Cells

2.3.1 Sample Selection and Orientation

The elasticity of a given crystal is influenced by the presence of structural defects within the probed sample (e.g. crystal mosaicity) (Giacovazzo et al., 2011). Therefore, the samples studied here were rigorously selected on the basis of their crystalline quality prior to being prepared and used for high-pressure experiments.

The first round of selection was simply based on the size of the grain (>200 μm ∅). δ-(Al,Fe)OOH belonging to the synthesis run No. H4944 were too small in size (<50 μm) to be further used. Subsequently, only grains with an homogeneous extinction, which is indicative for a single crystallographic domain, were selected. Successively, selected grains were glued onto a glass fiber with nail polish, placed on a goniometer head, and investigated with a Xcalibur[3] Kappa four-circle diffractometer run by the CrysAlis^{PRO} [3] software package. The investigated grain was exposed for 5 seconds to a molybdenum $K\alpha$ radiation (50 kV, 40 mA) at different angular combinations. Diffracted X-rays were collected using a Sapphire[3] 2 CCD area detector. This process allowed for the collection of a series of diffraction images in a relatively short period of time (∼10 minutes of total collection time). Acquired diffraction images were used to evaluate the number of distinguishable crystallographic domains within a single grain. Only grains that exhibited a single crystallographic domain were kept for further analyses. In that case, diffraction patterns were used to determine the unit-cell parameters, and their spatial relation with the Cartesian coordinate system of the instrument (matrix orientation).

The mosaicity of the selected single crystals was investigated using a HUBER[10] Eulerian four-circle diffractometer. This system, driven by the SINGLE software (Angel and Finger, 2011), combines a molybdenum glass tube (Mo-$K\alpha$ at 50 kV and 40 mA) with a point detector to enhance the signal-to-noise ratio in diffraction experiments. The previously determined matrix orientation was first updated according to the different coordinate systems used by the two different diffractometers, and then used to predict the position of the

[10]HUBER Diffraktionstechnik GmbH & Co. KG, Rimsting, Germany.

individual *hkl* diffraction peaks. The mosaicity of the probed single crystal was quantified by the Full Width at Half Maximum (FWHM) of individual diffraction peaks in rotation images collected using the ω-axis. Only single crystals showing a FWHM <0.1° in ω-scans were further used. For the single-crystal orientation procedure, at least two peaks (each one associated with a *hkl* diffraction peak with h, k and $l \neq 0$) were centered at positive and negative 2θ. The resulting diffraction peaks were used to correct the angular misalignment between calculated and observed matrix orientations (typically <1°). After misalignment correction, the matrix orientation was used to refine the unit-cell parameters of the single crystal. Subsequently, the single crystal was driven to a selected (*hkl*) plane, and then rotated in the ω-axis until the chosen (*hkl*) was parallel to the Y-axis of the diffractometer. A total of four (two + two) Fe-bearing phase E and δ-(Al,Fe)OOH single crystals were selected and oriented. Fe-bearing phase E and δ-(Al,Fe)OOH platelet orientations can be found in Chapter 5 and Chapter 6, respectively. Finally, the oriented single crystals were embedded in a drop of UV-activated glue to preserve their orientation. The double-side polishing of the oriented single crystal required for Brillouin measurements using the forward symmetric scattering geometry (see Subsection 2.4.3), was done by Raphael Njul[11]. Final thicknesses of Fe-bearing phase E and δ-(Al,Fe)OOH platelets were 20 and 13 μm, respectively.

2.3.2 Focused Ion Beam

The Focused Ion Beam (FIB) is an instrument that allows a morphological modification of a sample using a process referred to as *sputtering*. This process exploits the momentum transfer induced by inelastic collisions between an accelerated and focused ion beam, and the atoms that constitute the sample. Material can be removed from the sample with high-precision in the micrometer scale, thus shaping the material morphology. An FIB system can be combined together with a Scanning Electron Microscope (Subsection 2.1.1) to form a *dual system*. The combination of electron and ion columns allows for the monitoring of the milling process by high-resolution electron imaging. FIB dual beam systems are widely employed in experimental Geosciences to achieve tasks such as milling of TEM lamellae (Wirth, 2009), and the preparation of samples for high-pressure experiments (Marquardt and Marquardt, 2012). A detailed description of this technique is, however, beyond the scope of this thesis. More details about this technique and its applications can be found elsewhere (Nastasi et al., 1996; Orloff et al., 2003).
For this thesis, an FEI[5] Scios dual beam system (installed at the Bayerisches Geoinstitut, University of Bayreuth, Germany) was used to cut semi-circles from δ-(Al,Fe)OOH oriented platelets to be used in a multi-loading of a diamond-anvils cell (Schulze et al.,

[11] Bayrerisches Geoinstitut, University of Bayreuth, Germany. Email: raphael.njul@uni-bayreuth.de.

2017). The oriented platelets resulted from a procedure that involves the selection, orientation and polishing of single crystals (Subsection 2.3.1). For the FIB cutting procedure, platelets were glued on a metallic holder with nail polish. The platelets were not coated with conductive material. The FIB-cut was done using an accelereted Ga^+ beam (20 kV). An efficient sputtering rate was achieved using a current of 30 nA (Marquardt and Marquardt, 2012). Circular patterns (110 µm ∅) were first excavated from the original platelet, and successively split in two equal parts using a rectangular pattern (100 x 5 μm^2). The resulting semi-circles (Figure 2.6) were extracted from the original platelet using acetone to dissolve glue residuals. Semi-circles belonging to different platelets with distinct orientations were finally loaded in a diamond-anvil cell (see Figure 2.8).

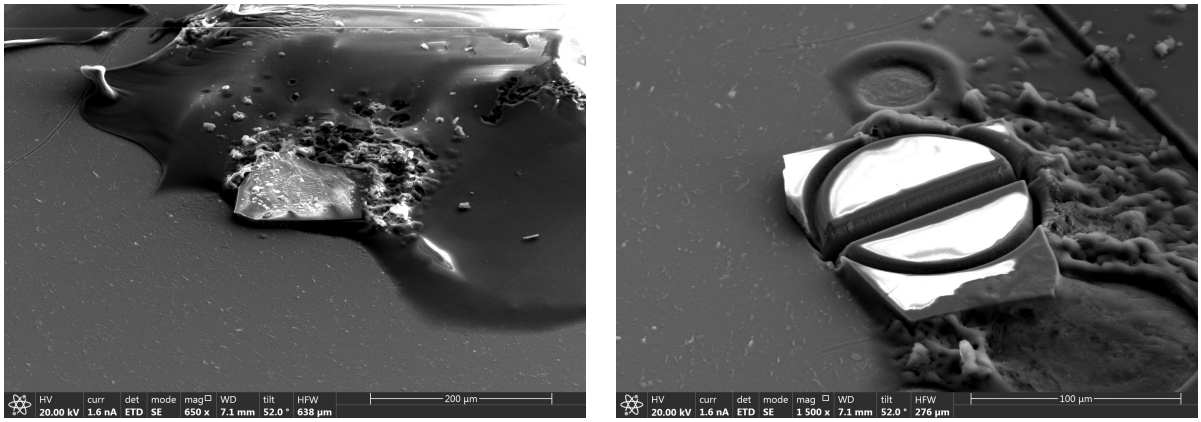

(a) (b)

Figure 2.6: Secondary electron images of a δ-(Al,Fe)OOH platelet before (a), and after (b) the FIB-cut procedure. Note that (b) has a higher magnification, and it is rotated by 90° with respect to (a).

2.3.3 Diamond-Anvil Cell

A diamond-anvil cell (DAC) is an experimental tool employed to compress a sample to high-pressure conditions. Its operating principle is based on the uniaxial compression of a sample between two parallel flat-top diamond-anvils. The sample is surrounded by a soft pressure-transmitting medium that ensures quasi-hydrostatic conditions during compression. The transparency of the diamonds to a wide range of electromagnetic radiations (e.g., X-ray and laser light) allows for the investigation of the sample while subjected to high-pressure conditions.

The most popular DAC designs are constituted by two main metallic parts: the piston and the cylinder (Figure 2.7). The piston and cylinder fit each other, and they both support the seats. Each diamond-anvil is glued on its respective seat, which can be translated and/or tilted to align the culets of the diamond-anvils. A pre-indented metallic gasket

is used to contain the pressure-transmitting medium, which fills the pressure chamber, ensuring quasi-hydrostatic stress environment within certain pressure limits (Angel et al., 2007). Pre-indentation of the gasket is done by squeezing it between the diamond-anvils. A cylindrical pressure chamber can be obtained using infrared laser cutting, or by drilling a hole with a drilling tool. Pressurization of the pressure chamber is achieved by tightening screws which connect the piston with the cylinder. The samples are placed inside the pressure chamber together with a pressure gauge. The pressure gauge is used to determine the pressure to which the samples are subjected (Subsection 2.3.4).

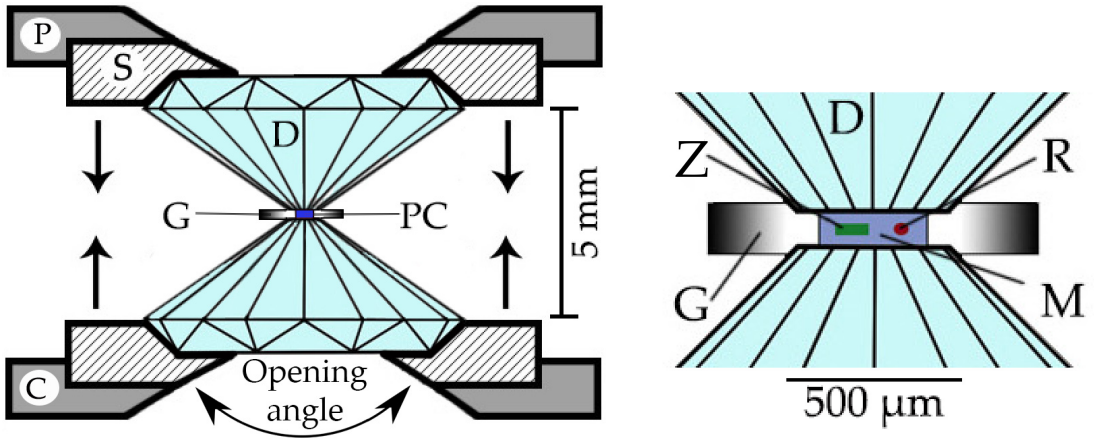

Figure 2.7: (a) A schematic sketch of a DAC equipped with 500 µm culet diamond-anvils. Arrows show the direction of compression. P = piston, C = cylinder, S = seats, D = diamond-anvils, G = gasket, PC = pressure chamber; (b) detail of the pressure chamber: Z = crystal, D = diamond-anvils, R = pressure gauge, M = pressure-transmitting medium, G = gasket.

The DAC framework used in this study follows the BX90 DAC design (Kantor et al., 2012). The BX90 is a pyston-cylinder DAC characterized by a large opening with an angle of 90°, allowing the access to the sample through a wide angular range during tilting (i.e, a rotation in the axis ∥ to the compression axis). In this study, the DAC was equipped with Ia type diamonds from Boehler-Almax[12] with 80° aperture and a culet size of 400 µm (Boehler and De Hantsetters, 2004). Diamond-anvils were glued with UHU[13] istant-glue on tungsten carbide seats. A circular pressure chamber (250 µm ∅) was cut by focusing an infrared laser on a pre-indented (50 µm) rhenium gasket. Neon and helium were employed as pressure-transmitting medium in two different runs. Both of the pressure-transmitting media ensured quasi-hydrostatic conditions during the pressure

[12] Almax easyLab Inc., Massachusetts, USA.
[13] UHU GmbH & Co. KG, Germany.

range of interest for the experiments (Klotz et al., 2009). The gas loading was done using the system at the Bayerisches Geoinstitut (University of Bayreuth, Germany). A detailed description of this loading system can be found in Kurnosov et al. (2008). FIB-cut platelets with different crystallographic orientations (Subsection 2.3.1) were loaded into the pressure chamber, along with a ruby used for pressure determination (Figure 2.8).

2.3.4 Pressure Determination in Diamond-Anvil Cells

When performing high-pressure experiments, it is important to have an accurate estimation of the pressure at which the experiments are being conducted. For this reason, materials that show a correlation between pressure and a change in their physical properties, e.g. ruby (Al_2O_3:Cr) (Forman et al., 1972) and Sm:YAG (Trots et al., 2013), are routinely used as pressure gauges in high-pressure experiments that involve the use of the DAC technology.

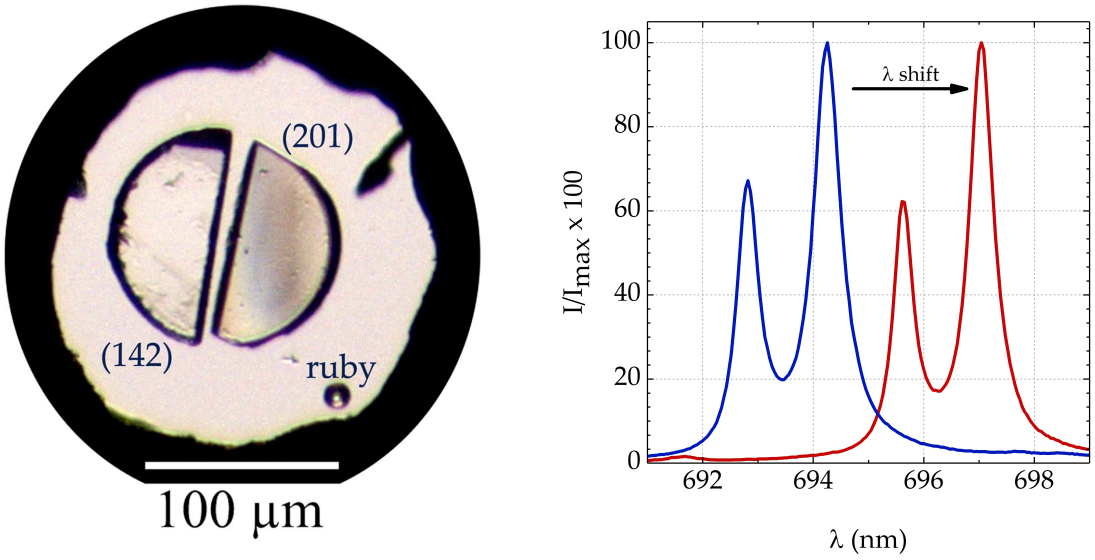

(a) (b)

Figure 2.8: (a) A view into the sample chamber of the DAC loaded with δ-(Al,Fe)OOH platelets. Pressure in the pressure chamber, determined using the shift on the ruby R1 fluorescence line, is 9.8 GPa. (142) and (201) refer to the crystallographic orientation of the two platelets. The ruby sphere is marked as "ruby"; (b) Ruby fluorescence spectra collected at ambient condition (blue) and 9.8 GPa (red).

In this study, the pressure determination during high-pressure experiments relied on the estimation of the pressure-induced frequency shift of the (Al_2O_3:Cr) ruby R1 fluorescence line. This pressure-related shift has been accurately calibrated at room temperature up to 150 GPa (Dewaele et al., 2008). The experimental strategy involved a double collection

(one through each diamond-anvil) of ruby fluorescence spectra before and after each high-pressure measurement session. In addition, a ruby fluorescence spectrum was collected at ambient conditions during each measurement session. The pressure inside the pressure chamber was determined following the pressure-frequency relation described by Mao et al. (1986):

$$P(\lambda) = \frac{A}{B} \cdot \left[\left(1 + \frac{\lambda}{\lambda_0} \right)^B - 1 \right] \tag{2.3}$$

and using the calibration given by Dewaele et al. (2008) ($A = 1920$ and $B = 9.61$), where λ_0 and λ are the measured frequency of the ruby R1 fluorescence line at ambient conditions and high pressures, respectively.

2.4 Single-Crystal Elasticity

2.4.1 Principles of Elasticity and Equation of State

The generalized form of the Hooke's law describes the relationship for infinitesimal strains between the stress (σ_{ij}) and strain (ε_{ij}) second-rank tensors with the compliance S_{ijkl} and the elastic C_{ijkl} fourth-rank tensors (Nye, 1957):

$$\varepsilon_{ij} = S_{ijkl}\sigma_{kl} \qquad \sigma_{ij} = C_{ijkl}\varepsilon_{kl} \qquad with \quad i,j,k,l = 1,2,3 \tag{2.4}$$

Being forth-rank tensors, S_{ijkl} and C_{ijkl} have 81 components each. This number, however, can be reduced to 36 components by taking into account the symmetrical relations in the stress (σ_{ij}=σ_{ji}) and strain ($\varepsilon_{ij} = \varepsilon_{ji}$) tensors, and in the S_{ijkl} and C_{ijkl} tensors (e.g., $C_{ijkl} = C_{ijlk}$). In addition, the subscripts of the components of a forth-rank tensor can be reduced from 36 to 21 using the Voigt notation:

$$11 \rightarrow 1; 22 \rightarrow 2; 33 \rightarrow 3; 23 = 32 \rightarrow 4; 13 = 31 \rightarrow 5; 12 = 21 \rightarrow 6 \tag{2.5}$$

Further reductions can be introduced depending on the crystal symmetry. Thus, the 21 independent, non-zero components necessary to describe a material with triclinic symmetry are reduced to 2 in the case of an isotropic material. Elastic tensors for triclinic (left)

and isotropic materials (right) are reported in Equation 2.6:

$$\begin{bmatrix} C_{11} & C_{12} & C_{13} & C_{14} & C_{15} & C_{16} \\ C_{12} & C_{22} & C_{23} & C_{24} & C_{25} & C_{26} \\ C_{13} & C_{23} & C_{33} & C_{34} & C_{35} & C_{36} \\ C_{14} & C_{24} & C_{34} & C_{44} & C_{45} & C_{46} \\ C_{15} & C_{25} & C_{35} & C_{45} & C_{55} & C_{56} \\ C_{16} & C_{26} & C_{36} & C_{46} & C_{56} & C_{66} \end{bmatrix} \begin{bmatrix} C_{11} & C_{12} & C_{12} & 0 & 0 & 0 \\ C_{12} & C_{11} & C_{12} & 0 & 0 & 0 \\ C_{12} & C_{12} & C_{11} & 0 & 0 & 0 \\ 0 & 0 & 0 & \frac{C_{11}-C_{12}}{2} & 0 & 0 \\ 0 & 0 & 0 & 0 & \frac{C_{11}-C_{12}}{2} & 0 \\ 0 & 0 & 0 & 0 & 0 & \frac{C_{11}-C_{12}}{2} \end{bmatrix} \tag{2.6}$$

For a given material, the incompressibility, or bulk modulus (K) is described as the ratio between the change in pressure (P) and the fractional compression-induced variation in V, while the material's resistance to shear stresses, or shear modulus (G), is described as the ratio between the stress and strain tensors (Nye, 1957; Poirier, 2000):

$$K = -V\left(\frac{\partial P}{\partial V}\right) \qquad G = \frac{\sigma_{ij}}{\varepsilon_{ij}} \qquad with \quad i \neq j \tag{2.7}$$

The C_{ijs} and S_{ijs} of an isotropic aggregate of anisotropic crystals can be quantified adiabatically with, for example, Brillouin spectroscopy (see Subsection 2.4.3). The C_{ijs} and S_{ijs} can then be used to describe K and G in isostrain (Voigt bounds) and isostress (Reuss bounds) conditions, respectively (Watt et al., 1976):

$$K_{Voigt} = \frac{C_{11} + C_{22} + C_{33} + 2 \cdot (C_{12} + C_{13} + C_{23})}{9} \tag{2.8}$$

$$G_{Voigt} = \frac{C_{11} + C_{22} + C_{33} + 3 \cdot (C_{44} + C_{55} + C_{66}) - (C_{12} + C_{13} + C_{23})}{15} \tag{2.9}$$

$$K_{Reuss} = \frac{1}{S_{11} + S_{22} + S_{33} + 2 \cdot (S_{12} + S_{13} + S_{23})} \tag{2.10}$$

$$G_{Reuss} = \frac{15}{4 \cdot (S_{11} + S_{22} + S_{33}) + 3 \cdot (S_{44} + S_{55} + S_{66}) - 4 \cdot (S_{12} + S_{13} + S_{23})} \tag{2.11}$$

The arithmetic average of elastic moduli in Voigt and Reuss bounds, know as the Voigt-Reuss-Hill (VRH) average, is representative for the elastic behavior of a crystalline aggregate of anisotropic crystals (Hill, 1952). The VRH average of bulk and shear moduli can be used in the computation of v_P and v_S, for an aggregate with a density ρ:

$$v_P = \sqrt{\frac{K_{VRH} + \frac{4}{3} \cdot G_{VRH}}{\rho}} \qquad v_S = \sqrt{\frac{G_{VRH}}{\rho}} \tag{2.12}$$

Alternatively, the bulk modulus of a given material can be determined through an isothermal deformation, such as the measurement of the decrease in V, when subjected to increases in P (i.e. compression). The relation between adiabatic (K_S) and isothermal (K_T) bulk modulus is described in terms of the thermal expansion coefficient (α), temperature (T) and Grüneiser parameter (γ), where c_V is the specific heat at constant volume (Poirier, 2000):

$$K_T = \frac{K_S}{(1 + \alpha \cdot T \cdot \gamma)} \qquad with \quad \gamma = \alpha \cdot K_T \cdot \frac{V}{c_V} \tag{2.13}$$

The elastic response of a crystal at high-pressure conditions, however, no longer fulfill the infinitesimal strain conditions required by Hooke's law. Hence, the necessity to develop the Equation of States (EoS) (Eliezer et al., 1986), i.e. P-V-T relations, which take into account large finite strains. In general, EoS models aim to describe a particular physical process in a regime of interest by refining model parameters to match the experimental data. For instance, various EoS models, with different domains of validity and different degrees of accuracy, have been developed for solid materials (Menikoff, 2007). The Birch-Murnaghan EoS (Birch, 1947) is commonly used in the high-pressure research in Geosciences (Angel, 2000).

Pressure is the volume V derivative of the Helmholtz energy (F) (Poirier, 2000):

$$P = -\left(\frac{\partial F}{\partial V}\right)_T \tag{2.14}$$

Through a Taylor expansion of Helmholtz energy in terms of finite Eulerian strain (f_E):

$$f_E = \frac{1}{2} \cdot \left[\left(\frac{V_0}{V}\right)^{2/3} - 1\right] \tag{2.15}$$

Pressure can be expressed, at a given reference temperature, as:

$$P = \frac{1}{3} \cdot (1 + 2 \cdot f_E)^{5/2} \cdot \left(a_2 \cdot f_E + \frac{1}{2} \cdot a_3 \cdot f_E^2 + \frac{1}{6} \cdot a_4 \cdot f_E^3 + \cdots\right) \tag{2.16}$$

where the coefficient of f_E, f_E^2 and f_E^3 in terms of bulk modulus (K_0) and its pressure derivatives of first order $K_0^{'} = \partial K/\partial P$ and second order $K_0^{''} = \partial^2 K_0/\partial P^2$.

$$a_2 = 9 \cdot K_0 \tag{2.17}$$

$$a_3 = 27 \cdot K_0 \cdot (K_0^{'} - 4) \tag{2.18}$$

$$a_4 = 81 \cdot K_0 \cdot \left[K_0 \cdot K_0^{''} + K_0^{'} \cdot (K_0^{'} - 7) + \frac{143}{9}\right] \tag{2.19}$$

by substituting Equation 2.17, Equation 2.18 and Equation 2.19 in Equation 2.16, one obtains a third order Birch-Murnaghan EoS:

$$P = \frac{1}{3} \cdot (1 + 2 \cdot f_E)^{5/2} \cdot \left[9 \cdot K_0 \cdot f_E \cdot \frac{27}{2} \cdot K_0 \cdot (K_0^{'} - 4) \cdot f_E^2 \right] \tag{2.20}$$

2.4.2 Single-Crystal X-ray Diffraction

Diffraction of X-ray by single crystals is a powerful technique that allows us to collect information about the crystalline structure of a given material, including unit-cell parameters and bond relations. Being non-distructive, this technique finds broad applications in different scientific environments (Giacovazzo et al., 2011). The principle behind this technique is based on the detection and interpretation of constructive interferences, resulting from the interaction between a crystalline structure and a focused X-ray beam. These constructive interferences follow the Bragg's law (Equation 2.2). If λ is known, it is possible to obtain information on the distance between planes of the same (hkl) family by measuring θ. In this thesis, the X-ray diffraction strategy aimed to describe the spatial relation between different (hkl) families, and uses this information to quantify the unit-cell parameters, their angular relation, and to characterize their evolution under high-pressure conditions. An exhaustive description of this technique can be found in Giacovazzo et al. (2011), while its application to high-pressure research can be found in Boffa-Ballaran et al. (2013).

All the X-ray diffraction experiments performed at high pressures have been conducted using the combined X-ray diffraction - Brillouin spectroscopy system installed at the Bayerisches Geoinstitut. In this system, the diffraction of X-ray radiation is induced using a focused flux of molibdenum Kα radiation, with a high intensity (55 mA), and accelerated with a potential of 45 kV. The X-ray radiation is generated by a Rigaku[14]FR-E Super Bright High-Brilliance rotating anode, and focused on the sample with a multilayer VaryMax^{TM} optics (80 mm focusing distance). The DAC containing the sample platelets was mounted on a goniometer head, and placed on a four-circle HUBER[10] Eulerian cradle with the compression axis $\parallel$ to the Y-axis of the diffractometer (Busing and Levy, 1967). The diffracted radiation was collected using a point detector equipped with YAP:Ce scintillator coupled to a photomultiplier. The X-ray diffraction system was controlled using the SINGLE software (Angel and Finger, 2011).

The experimental strategy involved a first quantification of the crystal offset along the beam (Y-axis). The Y-offset was quantified using the angular relations between hkl diffraction peaks with high ω ($>10°$) collected in eight different combinations of Eulerian angles

[14]Rigaku Corporation, Tokyo, Japan.

(King and Finger, 1979). Iterative corrections, applied through a translation of the DAC along the Y-axis using the screws of the goniometer head, were done to reduce the Y-offset to <100 μm. Subsequently, for each platelet, a typical data collection involved the eight-position centering 10 to 20 *hkl* diffraction peaks with $20° < 2\theta < 30°$. Collected diffraction profiles in ω-scans were individually refitted using a gaussian shape function, implemented in the Win-IntegrStp software (Angel, 2003). In the refitting process, FWHM, Kα1/Kα2 ratio, background and peak position were refined. Overall, the diffraction peaks did not experience a broadening during the high-pressure measurements (see Subsection 2.3.1). The unit-cell parameters were determined with a vector-least square refinement protocol implemented in the SINGLE software (Angel and Finger, 2011). Typically, uncertainties in the unit-cell volumes were around 10^{-4} Å. Results from the X-ray diffraction analyses on Fe-bearing phase E and δ-(Al,Fe)OOH are reported in Chapter 5 and Chapter 6, respectively.

2.4.3 Brillouin Spectroscopy

Brillouin spectroscopy can be used to obtain a complete description of the elastic properties of probed solid materials, such as glasses and minerals. In addition, Brillouin spectroscopy can be combined with DAC technology, allowing the exploration of matter at physical conditions relevant to the deep Earth's interior (Marquardt et al., 2009; Mashino et al., 2016; Kurnosov et al., 2017).

This section containes the general principles of Brillouin light scattering, as well as various aspects from a technical point of view. A more detailed review of the scattering process and experimental set-up details, as well as complete description on the applications of Brillouin spectroscopy to the Geosciences can be found in Speziale et al. (2014).

Brillouin spectroscopy refers to the spectroscopic measurements of Brillouin light scattering. Brillouin light scattering is an inelastic process, and occurs when a light wave interacts with periodic thermal oscillation in a scattering medium. In quantum mechanics, light can be described as *photons*, and the temperature-induced oscillations within the scattering medium as *phonons*. Therefore, in quantum mechanics, Brillouin light scattering is described by the interaction between an incident photon and a crystal acoustic phonon (Figure 2.9). During the scattering process, the annihilation of the incident photon (wavevector $\mathbf{k}_0$ and frequency ω_0), together with the creation or annihilation of a crystal phonon (wavevector $\mathbf{q}$ and frequency ω_q), result in a photon that is scattered at an angle θ (wavevector $\mathbf{k}_s$ and frequency ω_s). Due to the conservation of energy and momentum, the scattered photon will be characterized by a different frequency with respect to the incident photon. Down- and up-shifts in the frequency of the scattered photons are called Stokes (phonon creation) and anti-Stokes (phonon annihilation) events, respec-

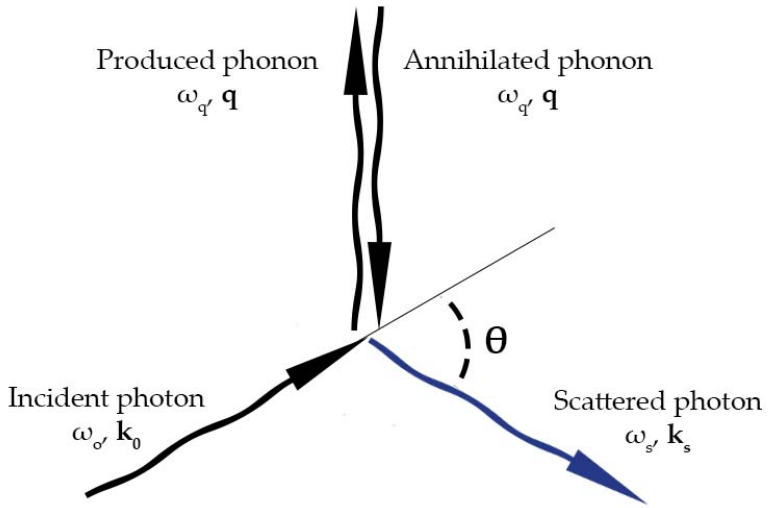

Figure 2.9: The Brillouin light scattering effect explained using a quantum mechanical approach.

tively:

$$Stokes \Rightarrow \begin{cases} \omega_s = \omega_0 - \omega_q \\ \mathbf{k}_s = \mathbf{k}_0 - \mathbf{q} \end{cases} \qquad anti - Stokes \Rightarrow \begin{cases} \omega_s = \omega_0 + \omega_q \\ \mathbf{k}_s = \mathbf{k}_0 + \mathbf{q} \end{cases} \tag{2.21}$$

where acoustic phonon velocities (v), frequency shifts ($\Delta\omega$) and scattering wave vectors ($\mathbf{q}$) are related by the equation (Grimsditch et al., 2001):

$$v = \frac{\Delta\omega}{|\mathbf{q}|} \tag{2.22}$$

The use of a DAC during high-pressure experiments limits the optical accessibility to the sample. The *forward symmetric geometry*, first proposed by Whitfield et al. (1976), is typically used to perform Brillouin scattering measurements using the DAC technology. In this scattering geometry (Figure 2.10), a transparent sample is shaped as a platelet with parallel polished surfaces. The acoustic phonon wave vector $\mathbf{q}$ lies along the bisector of the angle between incident and scattered photons (θ^{ext}). In high-pressures measurements, these scattering conditions are respected only if the culets of the diamonds-anvils are $\parallel$ to each other, and to the polished surfaces of the platelet. Non-parallelism of the platelets and/or diamond-anvil's surfaces might induce detectable deviations in measured frequency shifts (Speziale et al., 2014). If the external scattering angle, wavelength of the incident radiation, and experimentally measured frequency shifts ($\Delta\omega$) are known, then

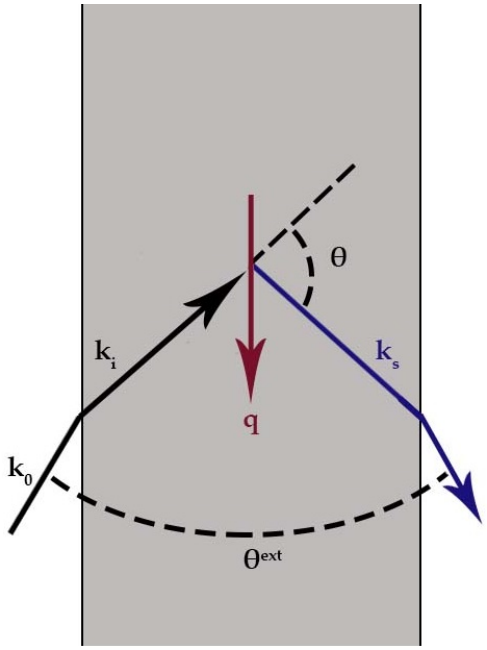

Figure 2.10: Brillouin scattering effect in *forward symmetric scattering geometry*. Note the refraction at the sample surfaces.

the acoustic wave velocities can be obtained using the relation:

$$v = \frac{\Delta\omega \cdot \lambda_0}{2 \cdot sin(\frac{\theta^{ext}}{2})} \tag{2.23}$$

The concept behind Brillouin spectroscopy is to use a radiation (with a known λ) to stimulate the Brillouin light scattering within the sample, and quantify shifts in the frequency ($\Delta\omega$) of the scattered photons. A typical experimental set-up utilizes a monochromatic laser as photon source, a χ circle to rotate the sample and to probe different phonon directions, and a Fabry-Perot interferometer (Lindsay et al., 1981) to resolve frequency shifts; photon detection can be done with a photomultiplier tube, or a more efficient photodiode detector.

Using a Fabry-Perot interferometer, a typical[15] Brillouin spectrum (Figure 2.11) is symmetric and dominated in intensity by the elastic contributions. A central singlet marks the Rayleigh peak ($\Delta\omega = 0$), while the *ghosts* (higher orders of repetition of the Rayleigh peak transmitted partially out of phase) are limited to the margin of the spectra. Inelastic contributions from the sample, pressure medium, and diamond-anvils are located between the Rayleigh peak and the ghosts.

[15]The use of a scanning amplitude larger than λ_0 is generally preferred, as it allows us to include the *ghosts* in the spectrum, hence provides an internal standard for the channel-frequency conversion.

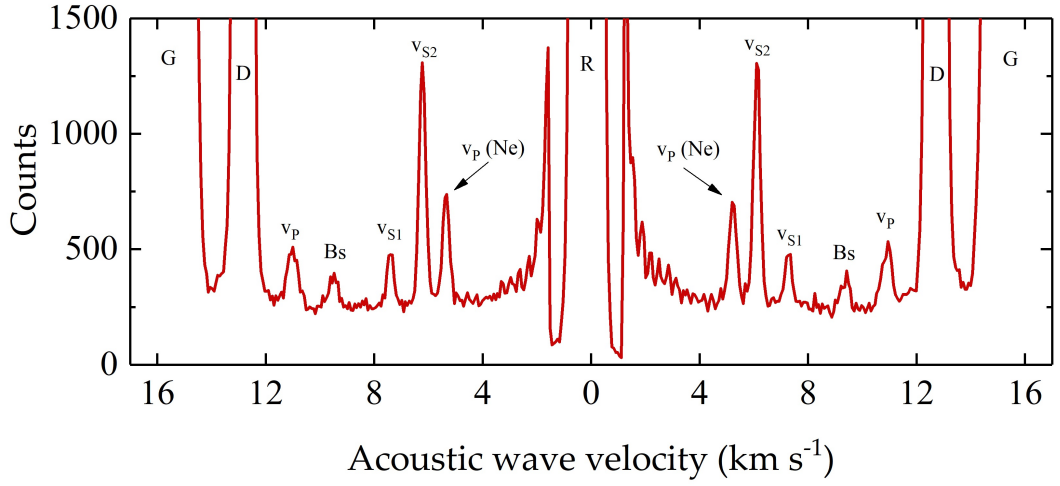

Figure 2.11: Representative Brillouin spectrum of δ-(Al,Fe)OOH. G = ghosts, D = diamonds quasi-transverse slow wave, v_P = sample longitudinal wave, Bs = Neon backscattering, v_{S1} = sample quasi-transverse fast wave, and v_{S2} = sample quasi-transverse slow wave. Note that the velocity scale is not valid for the backscattered peaks.

2.4.3.1 Brillouin Spectroscopy at the Bayerisches Geoinstitut

All of the Brillouin scattering measurements included in this thesis were performed following the *forward symmetric scattering geometry* using the combined X-ray diffraction - Brillouin Spectroscopy facility installed at the Bayerisches Geoinstitut (Trots et al., 2011). For specifics on the X-ray diffractometer system see Subsection 2.4.2.
In this system, Brillouin light scattering is stimulated using a monochromatic light (λ_0 = 532 nm) as photon source. This radiation is generated by a coherent Verdi[16] V2 solid-state Nd:YVO4 frequency-doubled laser. During measurements, thermally-induced stresses in the sample were avoided by keeping the laser power at the sample in the order of 70 mW. Different laser polarization were explored to maximize the elasto-optic coupling (Speziale et al., 2014). The laser light was focused on the sample using focusing optics (i.e., lens with focal length = 10 cm). Arbitrary acoustic wave directions were probed by rotating the sample along an axis perpendicular to the scattering plane. A four-circle HUBER[10] Eulerian cradle was used to rotate. The external scattering angle θ^{ext} (80°) was periodically calibrated with a glass standard (Kurnosov et al., 2017). The scattered light, collected by the collecting lens (focal length = 10 cm), was sent through a system of mirrors to a TFP-1[17] multi-pass tandem Fabry-Perot interferometer. In the interferometer, the distance between the first set of mirrors was 4 mm in all experiments. The scattered

[16] Coherent Inc., Santa Clara, California, USA.
[17] The Table Stable Ltd., Mettmenstetten, Switzerland.

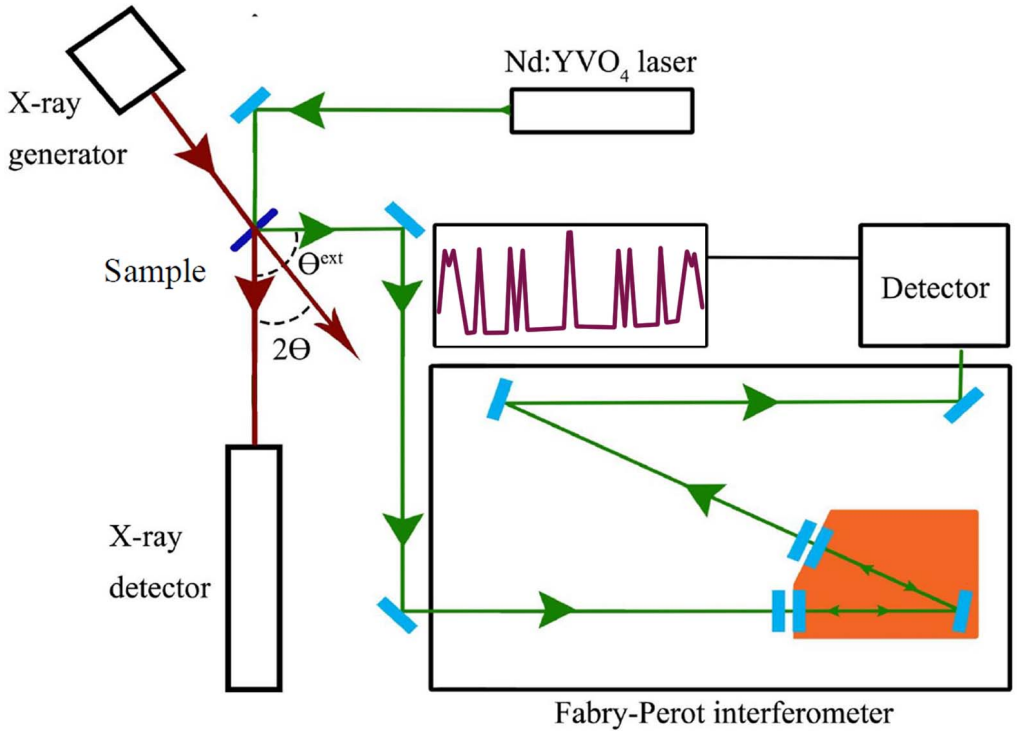

Figure 2.12: Sketch showing the main technical components of the Brillouin spectroscopy system installed at the Bayerisches Geoinstitut, University of Bayreuth, Germany.

light was detected with either a COUNT[18]-10B avalanche photodiode, or a Hamamatsu[19] H11202-050 single photon counting module. Both the detectors allowed the collection of spectrum with a final signal-to-noise ratio of ~3 in about 3 hours. Longer collections (up to 12 hours) were done along crystallographic directions characterized by low a elasto-optic coupling. Finally, the scattered light was recorded with a multi-channel analyzer (512 channels).

Pseudo-Voigt functions implemented in PeakFit[20] were used to fit individual spectral features in the channel range of Brillouin spectra. The final peak positions were calculated as an arithmetic mean between Stokes and anti-Stokes contributions. Frequency differences between Stokes and anti-Stokes contributions from the Rayleigh peak were converted from channel numbers using the relation:

$$\Delta\omega = \frac{c \cdot \Delta C}{2 \cdot d \cdot \mu} \tag{2.24}$$

c is the velocity of the light in vacuum, ΔC the difference in channel between the central peak and inelastic peak, d is the mirror distance and μ is the averaged mean position

[18]LASER COMPONENTS GmbH, Olching, Germany.
[19]Hamamatsu Photonics K.K., Hamamatsu, Japan.
[20]Systat Software Inc., San Jose, California, USA.

in channel of the ghosts and inelastic contributions to the spectrum. According to the scattering geometry used, the conversion of frequency shifts into acoustic wave velocities followed the Equation 2.23. Uncertainties in the velocity values were determined by the propagation of the uncertainties resulting from individual peak fitting, and the standard deviation between Stokes and anti-Stokes contributions.

2.4.3.2 Determination of the components of the elastic tensor from measured acoustic wave velocities

The propagation of a monochromatic plane-wave in an anisotropic medium of density ρ, is described by the Christoffel equation (Nye, 1957; Every, 1980):

$$(C_{ijkl}n_jn_l - \rho v^2\delta_{ik})U_k = 0 \tag{2.25}$$

This equation relates the elastic tensor (C_{ijkl}) and density of the medium (ρ) to the acoustic waves traveling through a certain direction (n_j and n_l), with velocities (v) and polarizations (U_k). Solutions to the Christoffel equations can be found by treating this equation as an eigenvector-eigenvalue problem, where U_k is the eigenvector of $C_{ijkl}n_jn_l$, and ρv^2 is the corresponding eigenvalue. The characteristic equation $|C_{ijkl}n_jn_l - \rho v^2\delta_{ik}| = 0$ can be reported in matrix form. In particular, by introducing the Christoffel matrix coefficient $\Gamma_{ik} = \Gamma_{ki} = C_{ijkl}n_jn_l$, and by substituting $x = -\rho v^2$, it becomes:

$$\begin{vmatrix} \Gamma_{11}+x & \Gamma_{12} & \Gamma_{13} \\ \Gamma_{21} & \Gamma_{22}+x & \Gamma_{23} \\ \Gamma_{31} & \Gamma_{32} & \Gamma_{33}+x \end{vmatrix} = \xi_0 \cdot x^3 + \xi_1 \cdot x^2 + \xi_2 \cdot x + \xi_3 = 0 \tag{2.26}$$

with the invariants $(\xi_0, \xi_1, \xi_2, \xi_3)$:

$$\xi_0 = 1 \tag{2.27}$$

$$\xi_1 = \Gamma_{11} + \Gamma_{22} + \Gamma_{33} \tag{2.28}$$

$$\xi_2 = \Gamma_{11}\cdot\Gamma_{22} + \Gamma_{22}\cdot\Gamma_{33} + \Gamma_{11}\cdot\Gamma_{33} - \Gamma_{13}\cdot\Gamma_{31} - \Gamma_{12}\cdot\Gamma_{21} - \Gamma_{23}\cdot\Gamma_{32} \tag{2.29}$$

$$\xi_3 = \Gamma_{11}\cdot\Gamma_{22}\cdot\Gamma_{33} + \Gamma_{12}\cdot\Gamma_{23}\cdot\Gamma_{31} + \Gamma_{13}\cdot\Gamma_{32}\cdot\Gamma_{21} - \Gamma_{13}\cdot\Gamma_{31}\cdot\Gamma_{22} - \Gamma_{12}\cdot\Gamma_{21}\cdot\Gamma_{33} - \Gamma_{23}\cdot\Gamma_{32}\cdot\Gamma_{11} \tag{2.30}$$

Being cubic, this equation has three real solutions. These three eigenvalue solutions are related to three different waves that show an individual geometrical relation between their polarization vector $\boldsymbol{U}$ and the propagation direction $\boldsymbol{n}$. In the case of anisotropic solids, the fastest wave (v_P) has a longitudinal polarization (i.e., $\boldsymbol{U}$ parallel $\boldsymbol{n}$); the other two

waves (v_{S1} and v_{S2}) have transverse polarizations (i.e., $\boldsymbol{U} \perp \boldsymbol{n}$). However, the geometrical relations between $\boldsymbol{n}$ and $\boldsymbol{U}$ slightly deviate from the ideal case. Therefore, it is common practice to add the suffix *quasi* when describing a wave (i.e., *quasi*-longitudinal and *quasi*-transverse waves).

For the determination of the elastic tensor (C_{ijkl}), the analytical density of the sample (ρ), wave directions (its direction cosines, n_j and n_l) together with the Brillouin acoustic wave velocities (v) dataset, were used in a least-square inversion of the Christoffel equations. This inversion routine was developed and implemented in an Origin[21] 2018 script by Johannes Buchen[22]. Cardano's solutions to the cubic equation expressed in terms of v_P, v_{S1} and v_{S2}, coordinate system conversions, together with a detailed description of the inversion procedure, are described in Buchen (2018). The elastic tensors of Fe-bearing phase E and δ-(Al,Fe)OOH resulting from the best-fit to the Christoffel equation can be found in Chapter 5 and Chapter 6, respectively. Elastic tensors determined at different pressure points have been used to refine individual C_{ijkl0} and their pressure dependency C'_{ijkl0}. The theoretical model based on the finite Eulerian strain approach described by Stixrude and Lithgow-Bertelloni (2005) has been used for this scope. In this model, the C_{ijkl} are expressed as a third order expansion of the Helmholtz energy (Subsection 2.4.1):

$$C_{ijkl} = (1 + 2 \cdot f)^{5/2} \cdot \Bigg\{ (C_{ijkl0} + (3 \cdot K_0 \cdot C'_{ijkl0} - 5 \cdot C_{ijkl0}) \cdot f + \left[6 \cdot K_0 \cdot C'_{ijkl0} - 14 \cdot C_{ijkl0} - \frac{3}{2} \cdot K_0 \cdot \delta^{ij}_{kl} \cdot (3 \cdot K'_0 - 16) \right] \cdot f^2 \Bigg\} \quad (2.31)$$

[21] OriginLab, Northampton, Massachusetts, USA.

[22] Now at: Seismological Laboratory, California Institute of Technology, Pasadena, California, USA. Email: jobuchen@caltech.edu.

3 | Synopsis and Aim of the Thesis

This chapter summarizes the studies performed with the aim of contributing to the open debates on the collisional history of the Moon, and the water distribution in the Earth's interior (Chapter 1). Section 3.1 presents the results obtained through the study of the shock metamorphism features recorded in the Apollo Section 15299,247, included as submitted manuscript in Chapter 4. The summary presented in Section 3.2 is based on single-crystal elasticity measurements of phase E and its implications for the seismic detection of water; the published manuscript is in Chapter 5. Section 3.3 provides an overview of the results obtained in the experimental study of the high-pressure elasticity of δ-(Al,Fe)OOH single crystals. This study focused on the characterization of the $P2_1nm$ and $Pnnm$ phases of δ-(Al,Fe)OOH, including details pertaining to the $P2_1nm$-$Pnnm$ transition; a draft of the manuscript is in Chapter 6.

3.1 Natural Incongruent Melting of Olivine in a Regolith Breccia Provides New Insights for Collisions on the Moon's Surface

This section summarizes the following submitted manuscript included in Chapter 4:

Satta, N., Miyahara, M., Ozawa, S., Marquardt, H., Nishijima, M., Arai, T., and Ohtani, E. Natural Incongruent Melting of Olivine in a Regolith Breccia Provides New Insights for Collisions on the Moon's Surface. Submitted to Proceedings of the National Academy of Sciences of the United States of America.

This study was conceived by E. Ohtani, N. Satta and H. Marquardt. T. Arai and E. Ohtani selected the sample. N. Satta, M. Miyahara, S. Ozawa, and E. Ohtani were involved in the collection, analysis and interpretation of the data. M. Nishijima operated the FIB. N. Satta wrote the first draft of the manuscript. All authors discussed the results and contributed to the final manuscript.

Despite the large number of studies on lunar samples, very little attention has been paid to the effect of shock metamorphism in terms of textures and mineralogical assemblages in lunar breccias, leading to uncertainties in our understanding of the collisional history of the Moon (Section 1.1). This study aims to fill this gap by acquiring textural and mineralogical evidences to constrain the response of the lunar regolith to shock compression, and evaluate how our observations contribute to the current knowledge of the Moon's collisional history.

For this study, we selected a lunar rock sampled during the Apollo 15 mission in the proximity of the Imbrium basin - one of the largest Moon's basins. The sample was investigated by SEM and TEM (Section 2.1), focusing on detailed observations to characterize a shock-melt pocket contained in an olivine grain. The studied shock-melt pocket was found to contain two distinct mineralogical domains, marking the difference between the inner and outer regions of the pocket (Figure 3.1). In particular, while a matrix of fragmented host olivine is present throughout the whole pocket, the interface between pocket and host grain showed a large concentration of small Fe-rich ferropericlase crystals (~50 nm ∅), together with Si-rich zones.
Although this is the first observation of ferropericlase in a lunar sample, previous studies on meteorites reported the presence of this high-pressure mineral within shocked textural

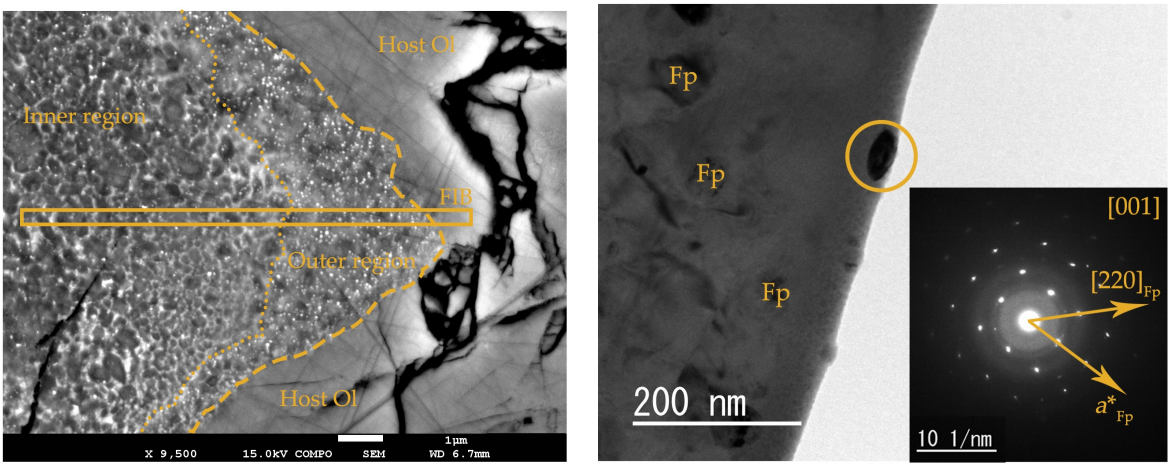

(a) (b)

Figure 3.1: SEM and TEM images of the investigated shock-melt pocket. (a) High magnification BSE image showing the mineralogical domains within the shock-melt pocket. Mustard rectangle shows the location of the block extracted with FIB. (b) TEM image of ferropericlase crystals. Inset SAED pattern is from the ferropericlase crystal within the mustard circle.

features. This enabled us to compare previous studies to ours to better understand the shock-induced processes behind the formation of lunar ferropericlase. In meteorites, ferropericlase has been found to be either the result of crystallization from a congruent melt or the product of solid-state transformation of olivine, hence always occurring in combination with its pyroxene complement. What is remarkable in our study is the fact that the pyroxene component is missing. Furthermore, when a shock feature such as a shock-melt pocket contains ferropericlase, the olivine surrounding the shock feature typically contains ringwodite and/or wadsleyite. However, we found no evidences supporting the presence of olivine high-pressure polymorphs nor their back transformation into olivine, suggesting that the shock conditions for their formation were, probably, never reached. The only reasonable hypothesis capable of reconciling our textural, mineralogical and chemical observations is ferropericlase forming as result of an incongruent melting of olivine, a process that has never been documented before in a natural context. Our findings confirm decades of experimental studies regarding the phase relation in the $(Mg,Fe)_2SiO_4$ system. Furthermore, these observations enabled us to speculate on the pressure-temperature evolution of the impact event that triggered olivine to melt incongruently, showing that the studied lunar rock experienced elevated temperatures during a relatively low-magnitude impact event. This finding implies that under shock compression, the lunar regolith behaves very differently from any other extra-terrestrial material studied thus far (Figure 3.2). We infer that a possible cause for this behavior lies in the intrinsic porous nature of the lunar regolith.

Thermal disturbances in the $^{40}Ar/^{39}Ar$ system are typically assumed to be induced by large impact events, and played a key role in the formulation of the LHB hypothesis, as well as in the dating of the main lunar basins. Our study shows that even impacts of low magnitude can expose the lunar regolith to temperatures capable of introducing disturbances in the $^{40}Ar/^{39}Ar$ system. Therefore, our study emphasizes the necessity to take into account the peculiar behavior of the lunar regolith under shock compression for a more accurate understanding of the Moon's collisional history using isotopic data.

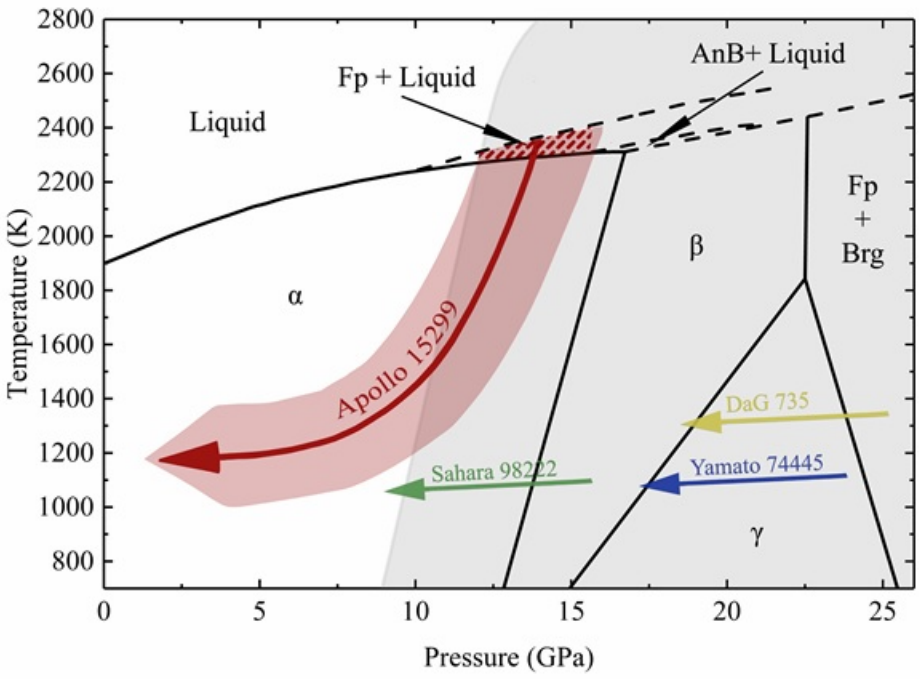

Figure 3.2: P-T conditions estimated from the high-pressure assemblages (patterned region in red) contained in the shock-melt pocket of the Apollo sample 15299. $(Mg,Fe)_2SiO_4$ phase relations are from Presnall and Walter (1993). The light grey region in the P-T area represents the stability field of stishovite Schmitt and Ahrens (1983). Shaded region in red shows a tentative P-T path of the Apollo sample 15299. Yellow, green and blue arrows represent the tentative adiabatic decompression paths of shergottite - DaG 735 (Miyahara et al., 2011) and, L6 chondrites - Sahara 98222 and Yamato 74445 (Ozawa et al., 2009), respectively. Fp = ferropericlase, Brg = bridgmanite, α = olivine, β = wadsleyite, γ = ringwoodite and AnB = anhydrous phase B.

3.2 Single-Crystal Elasticity of Iron-Bearing Phase E and Seismic Detection of Water in the Earth's Upper Mantle

This section summarizes the following published manuscript included in Chapter 5:

Satta, N., Marquardt, H., Kurnosov, A., Buchen, J., Kawazoe, T., McCammon, C. and Boffa Ballaran, T. (2019). Single-Crystal Elasticity of Iron-Bearing Phase E and Seismic Detection of Water in the Earth's Upper Mantle. American Mineralogist:1526-1529.

This study was conceived by H. Marquardt and N. Satta. The samples were synthesized by T. Kawazoe. N. Satta, A. Kurnosov, T. Boffa Ballaran, C. McCammon were involved in the collection of the data. N. Satta analyzed the data with the help of J. Buchen. N. Satta wrote the first draft of the manuscript with the help of H. Marquardt. All authors discussed the results and contributed to the final manuscript.

Despite the role that phase E might play in stabilizing and delivering water in the Earth's mantle (Subsection 1.2.1), its shear elastic properties are unknown, limiting the prediction of its seismic signature, and in turn, its quantification at depth through seismological observations. This study focused on determining the first complete description of the elastic tensor of phase E, and includes an evaluation of how phase E may affect seismic wave velocities in subduction zone contexts.

For this study, large single crystals of optically clear Fe-bearing phase E were synthesized, and analytical techniques were employed to constrain the chemical composition and unit-cell parameters. Two distinct platelets with complementary orientations were measured by Brillouin spectroscopy. More than 70 measured velocities were collected along 19 different directions, placing tight constrains on the full elastic tensor of phase E at ambient conditions. The resulting bulk and shear moduli, together with the analytical density value, were used to compute aggregate velocities (Section 2.4). According to our results, phase E exhibits the lowest aggregate velocities in comparison to other minerals predicted to be stable along with phase E in a subduction scenario. This suggests that, if present, phase E would cause a detectable decrease of seismic velocities. To evaluate this possibility, three different hydration states (dry, hydrous and phase E-bearing) were assumed to model mineralogical assemblages of the lowermost upper mantle, and shallow transition zone. Phase E-bearing assemblages represent the highest hydration state considered, and

their seismic velocities were computed following the mineral fractions given by Ohtani et al. (2004). For the computation of hydrous rocks, phase E was assumed to form at the expenses of the $(Mg,Fe)_2SiO_4$ mineralogical component. Therefore, hydrous assemblages have their phase E fractions replaced by hydrous wadsleyite and olivine in upper mantle and transition zone rocks, respectively. The computation of dry rocks utilizes the same mineral fractions assumed for the hydrous rocks, but because no water is present, dry olivine and wadsleyite were used in the modeling. Figure 3.3 displays the comparison of the ambient condition aggregate velocities between the three considered hydration states of the upper mantle and transition zone assemblages. Being a comparison at ambient conditions, this model does not provide the absolute differences between the considered assemblages. However, it highlights that aggregate velocities decrease towards higher hydration states, in particular in the transition zone assemblages. We further explored the evolution of bulk and shear moduli of phase E with pressure. Using available compressional data, K'_{T0} was constrained, while G' was assumed to be identical to the value of phase A. We found that at depths of the shallow transition zone, phase E would still be sensibly slower than wadsleyite. This suggests that even small amounts of phase E would cause a detectable deviation in seismic velocities, hence allowing the seismic mapping of water at depth.

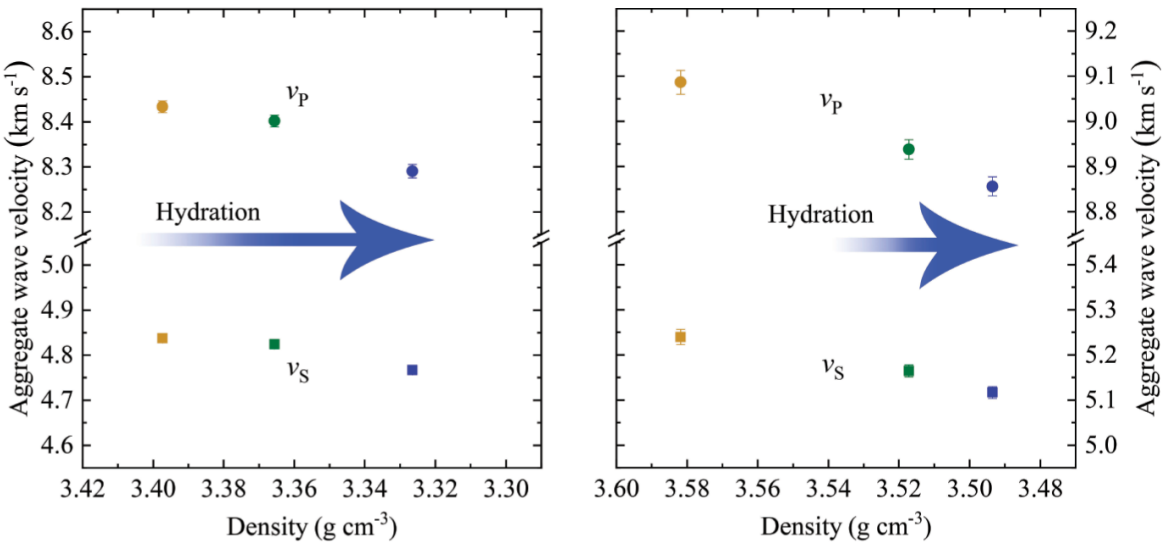

Figure 3.3: Aggregate velocities of dry, hydrous, and phase E-bearing upper mantle (a) and transition zone (b) peridotites at ambient conditions as a function of density. Circles and squares refer to v_P and v_S, respectively. Dry, hydrous, and phase E-bearing rock velocities are shown in yellow, green, and blue colors, respectively.

3.3 Elastic Softening Driven by Hydrogen Disorder in δ-(Al,Fe)OOH

This section summarizes the following manuscript prepared for submission and included in Chapter 6:

Satta, N., Criniti, G., Kurnosov, A., Boffa Ballaran, T., Ishii, T., and Marquardt, H. Elastic Softening Driven by Hydrogen Disorder in δ-(Al,Fe)OOH.

This study was conceived by H. Marquardt and N. Satta. The samples were synthesized by T. Ishii. N. Satta, G. Criniti, A. Kurnosov and T. Boffa Ballaran were involved in the collection of the data. N. Satta and G. Criniti processed and interpreted the data, and wrote the first draft of the manuscript with the help of T. Boffa Ballaran.

Solid solutions between phase H, δ-AlOOH and ε-FeOOH are the main candidates in the retainment of water in the deepest regions of the Earth's lower mantle (Subsection 1.2.1). For this reason, aluminum and iron end-members have been extensively investigated by both theoretical and experimental studies. δ-AlOOH is expected to undergo a phase transition, from $P2_1nm$ to $Pnnm$, between 8 and 10 GPa. This pressure-induced transition is triggered by a disordered configuration of the hydrogen bonds. While some theoretical predictions pointed out that this phase transition has major influences on the elastic response of δ-(Al,Fe)OOH, experimental confirmation and quantification is missing. In particular, experimental investigations of these oxy-hydroxides are limited to X-ray and neutron diffraction investigations, leaving the prediction of the elastic tensors of both $P2_1nm$ and $Pnnm$ δ-(Al,Fe)OOH structures to theoretical studies. In this study, we provided the first quantitative experimental constrains on the elastic tensors of $P2_1nm$ and $Pnnm$ δ-(Al,Fe)OOH, and evaluate the effects that the $P2_1nm$-$Pnnm$ phase transition has on its elastic behavior.

Large single crystals of δ-$(Al_{0.97}Fe_{0.03})$OOH were synthesized (Section 2.2). Two optically clear single crystals were selected, oriented parallel to complementary crystallographic planes, and prepared for high-pressure experiments with the DAC (Section 2.3). X-ray diffraction and Brillouin scattering measurements were simultaneously collected at the same pressure conditions, allowing us to probe both the unit-cell parameters and the elastic tensor.
By tracking the decrease in intensity of the $0\bar{3}0$ reflection, which is systematically extinct in the $Pnnm$ space group, we were able to constrain the transition pressure. The match

between our results of those of previous X-ray and neutron diffraction studies indicates that the incorporation of Fe^{3+} has a negligible effect on the $P2_1nm$-$Pnnm$ transition in δ-AlOOH. The variation of unit-cell parameters and volume resulting from X-ray diffraction analyses were fitted using the 3rd-order Birch-Murnaghan EoS (BM3) (Section 2.4). In this process, measured points close to the transition pressure were excluded to avoid any contribution to the EoS from volume data, which may be affected by the onset of the transition. As displayed in Figure 3.4, normalized volumes show a deviation from the EoS fit while approaching the transition pressure, suggesting a softening of the bulk modulus. Axial compressibilities show that the b-axis is the most affected by the softening (Figure 3.4).

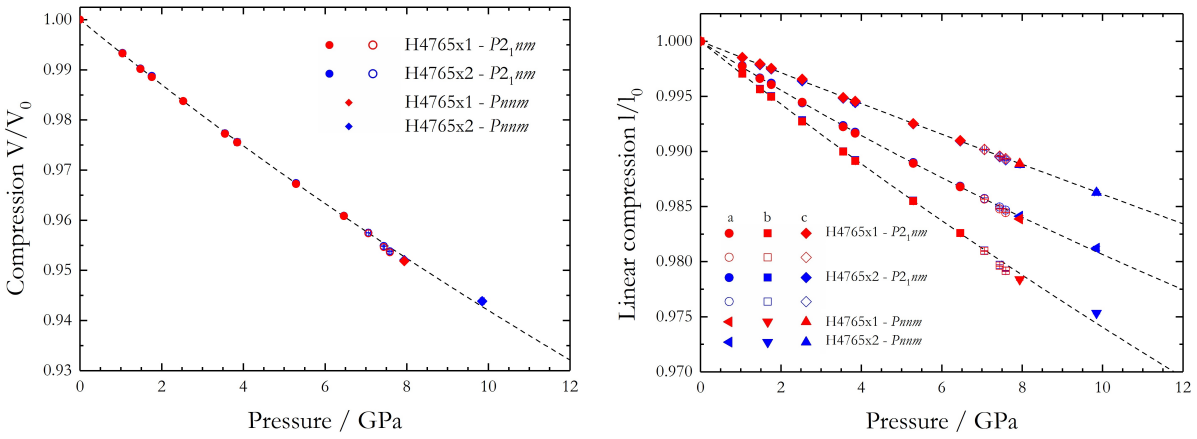

Figure 3.4: Variation with pressure of (a) the unit-cell volume and (b) linear compressibilites of δ-(Al,Fe)OOH. The values of each crystal have been normalized with respect to those measured at room pressure. Open symbols refer to data close to the $P2_1nm$ to $Pnnm$ transition pressure and they were not considered in the BM3 EoS fit.

Most of the C_{ij} constrained at ambient conditions are in agreement with those predicted by theoretical calculations. Differences are found for the stiffnesses along the a- and b-axis, C_{11} and C_{22} respectively. In our case, C_{11} is stiffer by about 20% with respect to C_{22}, while theoretical studies report very similar values. C_{ij} pressure derivatives were estimated using Equation 2.31, and also in this case, measured points close to the transition pressure were excluded from the fit to evaluate the effect of the softening on the individual C_{ij}. We found that C_{22}, C_{12} and C_{23} show a major softening when approaching the transition pressure, in agreement with our X-ray diffraction results. As a consequence, the softening affects the bulk modulus, while the shear modulus smoothly increases with pressure (Figure 3.5). After the phase transition, the bulk modulus shows a substantial increase with respect to the last measured pressure point before the softening. The soft-

ening is ultimately reflected in the compressional velocity, while the average shear velocity shows a linear increase with pressure (Figure 3.5).

This study shows that an elastic softening marks the change in the hydrogen bond configurations in δ-(Al,Fe)OOH, and could be a precursor of the hydrogen bond symmetrization. Other hydroxide phases are expected to have a pressure-induced symmetrization of their hydrogen bonds, and can be subjected to a softening of their elastic moduli, and in turn, of their aggregate velocities.

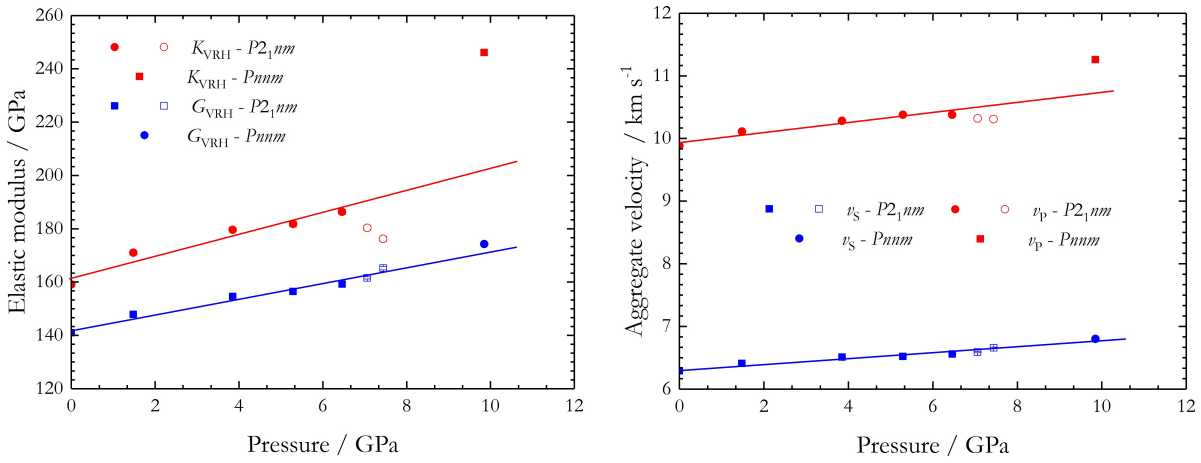

Figure 3.5: Variation with pressure of (a) aggregate elastic moduli and (b) the aggregate velocities of δ-(Al,Fe)OOH. Open symbols refer to data close to the $P2_1nm$ to $Pnnm$ transition pressure and they were not considered in the fit.

References

Abramov, O. and Mojzsis, S. J. (2009). Microbial habitability of the Hadean Earth during the late heavy bombardment. *Nature*, 459(7245):419–422. doi: 10.1038/nature08015.

Alexander, C. M. O., Bowden, R., Fogel, M. L., Howard, K. T., Herd, C. D. K., and Nittler, L. R. (2012). The provenances of asteroids, and their contributions to the volatile inventories of the terrestrial planets. *Science*, 337(6095):721–723. doi: 10.1126/science.1223474.

Alt, J. C., Honnorez, J., Laverne, C., and Emmermann, R. (1986). Hydrothermal alteration of a 1 km section through the upper oceanic crust, Deep Sea Drilling Project Hole 504B: Mineralogy, chemistry and evolution of seawater-basalt interactions. *Journal of Geophysical Research: Solid Earth*, 91(B10):10309–10335. doi: 10.1029/JB091iB10p10309.

Altwegg, K., Balsiger, H., Bar-Nun, A., Berthelier, J. J., Bieler, A., Bochsler, P., Briois, C., Calmonte, U., Combi, M., Keyser, J. D., Eberhardt, P., Fiethe, B., Fuselier, S., Gasc, S., Gombosi, T. I., Hansen, K. C., Hässig, M., Jäckel, A., Kopp, E., Korth, A., LeRoy, L., Mall, U., Marty, B., Mousis, O., Neefs, E., Owen, T., Rème, H., Rubin, M., Sémon, T., Tzou, C.-Y., Waite, H., and Wurz, P. (2015). 67P/Churyumov-Gerasimenko, a Jupiter family comet with a high D/H ratio. *Science*, 347(6220). doi: 10.1126/science.1261952.

Anderson, D. L., Sammis, C. G., and Phinney, R. A. (1969). Brillouin scattering-a new geophysical tool. In *The Application of Modern Physics to Earth and Planetary Interiors*. Wiley, New York.

Angel, R. J. (2000). Equations of State. *Reviews in Mineralogy and Geochemistry*, 41(1):35–59. doi: 10.2138/rmg.2000.41.2.

Angel, R. J. (2003). Automated profile analysis for single-crystal diffraction data. *Journal of Applied Crystallography*, 36(2):295–300. doi: 10.1107/S0021889803001134.

Angel, R. J., Bujak, M., Zhao, J., Gatta, G. D., and Jacobsen, S. D. (2007). Effective hydrostatic limits of pressure media for high-pressure crystallographic studies. *Journal of Applied Crystallography*, 40(1):26–32. doi: 10.1107/S0021889806045523.

Angel, R. J. and Finger, L. W. (2011). *SINGLE*: a program to control single-crystal diffractometers. *Journal of Applied Crystallography*, 44(1):247–251. doi: 10.1107/S0021889810042305.

Asimow, P. D. and Langmuir, C. (2003). The importance of water to oceanic mantle melting regimes. *Nature*, 421(6925):815. doi: 10.1038/nature01429.

Aubaud, C., Hauri, E. H., and Hirschmann, M. M. (2004). Hydrogen partition coefficients between nominally anhydrous minerals and basaltic melts. *Geophysical Research Letters*, 31(20). doi: 10.1029/2004GL021341.

Bebout, G. E. (1995). The impact of subduction-zone metamorphism on mantle-ocean chemical cycling. *Chemical Geology*, 126(2):191–218. doi: 10.1016/0009-2541(95)00118-5.

Birch, F. (1947). Finite elastic strain of cubic crystals. *Physical Review*, 71:809–824. doi: 10.1103/PhysRev.71.809.

Birch, F. (1952). Elasticity and constitution of the Earth's interior. *Journal of Geophysical Research (1896-1977)*, 57(2):227–286. doi: 10.1029/JZ057i002p00227.

Bockelée-Morvan, D., Crovisier, J., Mumma, M., and Weaver, H. A. (2004). The composition of cometary volatiles. In *Comets II*, volume 5, pages 391–423. University Arizona Press.

Boehler, R. and De Hantsetters, K. (2004). New anvil designs in diamond-cells. *High Pressure Research*, 24(3):391–396. doi: 10.1080/08957950412331323924.

Boehnke, P. and Harrison, T. M. (2016). Illusory late heavy bombardments. *Proceedings of the National Academy of Sciences*, 113(39):10802–10806. doi: 10.1073/pnas.1611535113.

Boffa-Ballaran, T., Kurnosov, A., and D, T. (2013). Single-crystal X-ray diffraction at extreme conditions: A review. *High Pressure Research*, 33(3):453–465. doi: 10.1080/08957959.2013.834052.

Bolfan-Casanova, N. (2005). Water in the Earth's mantle. *Mineralogical Magazine*, 69(3):229–257.

Bottke, W. F. and Norman, M. D. (2017). The late heavy bombardment. *Annual Review of Earth and Planetary Sciences*, 45(1):619–647. doi: 10.1146/annurev-earth-063016-020131.

Bragg, W. L. (1914). The analysis of crystals by the X-ray spectrometer. *Proceedings Of The Royal Society A*, 89(613):468–489.

Brandenburg, J. P. and van Keken, P. E. (2007). Deep storage of oceanic crust in a vigorously convecting mantle. *Journal of Geophysical Research: Solid Earth*, 112(B6). doi: 10.1029/2006JB004813.

Buchen, J. (2018). *The Elastic Properties of Wadsleyite and Stishovite at High Pressures : Tracing Deep Earth Material Cycles.* PhD thesis, Bayreuther Graduiertenschule für Mathematik und Naturwissenschaften (BayNAT), Bayreuth. doi: 10.15495/EPub_UBT_00004410.

Buchen, J., Marquardt, H., Speziale, S., Kawazoe, T., Boffa Ballaran, T., and Kurnosov, A. (2018). High-pressure single-crystal elasticity of wadsleyite and the seismic signature of water in the shallow transition zone. *Earth and Planetary Science Letters*, 498:77–87. doi: 10.1016/j.epsl.2018.06.027.

Busing, W. R. and Levy, H. A. (1967). Angle calculations for 3- and 4-circle X-ray and neutron diffractometers. *Acta Crystallographica*, 22(4):457–464. doi: 10.1107/S0365110X67000970.

Campione, M. and Capitani, G. C. (2013). Subduction-zone earthquake complexity related to frictional anisotropy in antigorite. *Nature Geoscience*, 6(10):847. doi: 10.1038/ngeo1905.

Chen, M., Goresy, A. E., and Gillet, P. (2004). Ringwoodite lamellae in olivine: Clues to olivine–ringwoodite phase transition mechanisms in shocked meteorites and subducting slabs. *Proceedings of the National Academy of Sciences*, 101(42):15033–15037. doi: 10.1073/pnas.0405048101.

Chen, M., Sharp, T. G., Goresy, A. E., Wopenka, B., and Xie, X. (1996). The majorite-pyrope + magnesiowüstite assemblage: Constraints on the history of shock veins in chondrites. *Science*, 271(5255):1570–1573. doi: 10.1073/pnas.0405048101.

Chen, M., Xie, X., El Goresy, A., Wopenka, B., and Sharp, T. G. (1998). Cooling rates in the shock veins of chondrites: constraints on the $(Mg, Fe)_2SiO_4$ polymorph transformations. *Science in China Series D: Earth Sciences*, 41(5):522–528. doi: 10.1007/BF02877743.

Chyba, C. F. (1990). Impact delivery and erosion of planetary oceans in the early inner Solar System. *Nature*, 343(6254):129–133. doi: 10.1038/343129a0.

Chyba, C. F. (1991). Terrestrial mantle siderophiles and the lunar impact record. *Icarus*, 92(2):217 – 233. doi: 10.1016/0019-1035(91)90047-W.

Clayton, R. N., Mayeda, T. K., and Rubin, A. E. (1984). Oxygen isotopic compositions of enstatite chondrites and aubrites. *Journal of Geophysical Research: Solid Earth*, 89(S01):C245–C249. doi: 10.1029/JB089iS01p0C245.

Cliff, G. and Lorimer, G. (1975). The quantitative analysis of thin specimens. *Journal of Microscopy*, 103(2):203–207.

Cortona, P. (2017). Hydrogen bond symmetrization and elastic constants under pressure of δ-AlOOH. *Journal of Physics: Condensed Matter*, 29(32):325505. doi: 10.1088/1361-648x/aa791f.

Crichton, W. and Ross, N. (2000). Equation of state of phase E. *Mineralogical Magazine*, 424:561-567. doi: 10.1180/002646100549427.

Dai, C., Jin, X., Fu, S., Shi, S., and Wang, D. (1997). The equation-of-states of Jilin ordinary chondrite and Nandan iron meteorite. *Science in China Series D: Earth Sciences*, 40(4):403–410. doi: 10.1007/BF02877572.

Dalrymple, G. B. and Ryder, G. (1993). $^{40}Ar/^{39}Ar$ age spectra of Apollo 15 impact melt rocks by laser step-heating and their bearing on the history of lunar basin formation. *Journal of Geophysical Research: Planets*, 98(E7):13085–13095. doi: 10.1029/93JE01222.

Dalrymple, G. B. and Ryder, G. (1996). $Argon^{40}/argon^{39}$ age spectra of Apollo 17 highlands breccia samples by laser step heating and the age of the Serenitatis basin. *Journal of Geophysical Research: Planets*, 101(E11):26069–26084. doi: 10.1029/96JE02806.

Dauphas, N. (2017). The isotopic nature of the Earth's accreting material through time. *Nature*, 541(7638). doi: 10.1038/nature20830.

Dauphas, N., Marty, B., and Reisberg, L. (2002). Inference on terrestrial genesis from molybdenum isotope systematics. *Geophysical Research Letters*, 29(6):8–1–8–3. doi: 10.1029/2001GL014237.

Dewaele, A., Torrent, M., Loubeyre, P., and Mezouar, M. (2008). Compression curves of transition metals in the Mbar range: Experiments and projector augmented-wave calculations. *Physical Review B*, 78:104102. doi: 10.1103/PhysRevB.78.104102.

Dilek, Y. and Furnes, H. (2014). Ophiolites and their origins. *Elements*, 10(2):93–100. doi: 10.2113/GSELEMENTS.10.2.93.

Dowty, E., Prinz, M., and Keil, K. (1973). Composition, mineralogy, and petrology of 28 mare basalts from Apollo 15 rake samples. In *Lunar and Planetary Science Conference Proceedings*, volume 1, pages 423–444. New York, Pergamon Press, Inc.

Duan, Y., Sun, N., Wang, S., Li, X., Guo, X., Ni, H., Prakapenka, V. B., and Mao, Z. (2018). Phase stability and thermal equation of state of δ-AlOOH: Implication for water transportation to the Deep Lower Mantle. *Earth and Planetary Science Letters*, 494:92–98. doi: 10.1016/j.epsl.2018.05.003.

Eliezer, S., Ghatak, A., and Hora, H. (1986). *An Introduction to Equations of State: Theory and Applications*. Cambridge University Press. doi: 10.1017/S1323358000021962.

Every, A. G. (1980). General closed-form expressions for acoustic waves in elastically anisotropic solids. *Physical Review B*, 22:1746–1760. doi: 10.1103/PhysRevB.22.1746.

Faccenda, M. (2014). Water in the slab: A trilogy. *Tectonophysics*, 614:1–30. doi: 10.1016/j.tecto.2013.12.020.

Fernandes, V., Fritz, J., Weiss, B., Garrick-Bethell, I., and Shuster, D. (2013). The bombardment history of the Moon as recorded by ^{40}ar-^{39}ar chronology. *Meteoritics & Planetary Science*, 48(2):241–269.

Forman, R. A., Piermarini, G. J., Barnett, J. D., and Block, S. (1972). Pressure measurement made by the utilization of ruby sharp-line luminescence. *Science*, 176(4032):284–285. doi: 10.1126/science.176.4032.284.

Frost, D. J. (1999). The stability of dense hydrous magnesium silicates in Earth's transition zone and lower mantle. *Mantle Petrology: Field Observations and High Pressure Experimentation: A Tribute to Francis R.(Joe) Boyd. The Geochemical Society*, pages 283–296. doi: 10.1029/2003JB002413.

Fukao, Y. and Obayashi, M. (2013). Subducted slabs stagnant above, penetrating through, and trapped below the 660 km discontinuity. *Journal of Geophysical Research: Solid Earth*, 118(11):5920–5938. doi: 10.1002/2013JB010466.

Giacovazzo, C., Monaco, H., Artioli, G., Viterbo, D., Ferraris, G., Gilli, G., Zanotti, G., and Catti, M. (2011). *Fundamentals of Crystallography*. Oxford University Press. doi: 10.1093/acprof:oso/9780199573653.001.0001.

Glikson, A. Y. (2001). The astronomical connection of terrestrial evolution: Crustal effects of post-3.8 Ga mega-impact clusters and evidence for major 3.2±0.1 Ga bombardment of the Earth–Moon system. *Journal of Geodynamics*, 32(1-2):205–229. doi: 10.1016/S0264-3707(01)00029-1.

Gomes, R., Levison, H. F., Tsiganis, K., and Morbidelli, A. (2005). Origin of the cataclysmic Late Heavy Bombardment period of the terrestrial planets. *Nature*, 435(7041):466–469. doi: 10.1038/nature03676.

Greenwood, R. C., Barrat, J.-A., Miller, M. F., Anand, M., Dauphas, N., Franchi, I. A., Sillard, P., and Starkey, N. A. (2018). Oxygen isotopic evidence for accretion of Earth's water before a high-energy Moon-forming giant impact. *Science Advances*, 4(3):eaao5928. doi: 10.1126/sciadv.aao5928.

Grimsditch, M., Guedes, I., Vavassori, P., Metlushko, V., Ilic, B., Neuzil, P., and Kumar, R. (2001). Brillouin scattering and diffracted magneto-optical Kerr effect from arrays of dots and antidots. *Journal of Applied Physics*, 89(11):7096–7100. doi: 10.1063/1.1359789.

Hacker, B. R., Peacock, S. M., Abers, G. A., and Holloway, S. D. (2003). Subduction factory 2. Are intermediate-depth earthquakes in subducting slabs linked to metamorphic dehydration reactions? *Journal of Geophysical Research: Solid Earth*, 108(B1). doi: 10.1029/2001JB001129.

Hiesinger, H. and Head, J. W. (2006). New views of lunar geoscience: An introduction and overview. *Reviews in Mineralogy and Geochemistry*, 60(1):1–81. doi: 10.2138/rmg.2006.60.1.

Hill, R. (1952). The elastic behaviour of a crystalline aggregate. *Proceedings of the Physical Society. Section A*, 65(5):349–354. doi: 10.1088/0370-1298/65/5/307.

Hirth, G. and Kohlstedt, D. L. (1996). Water in the oceanic upper mantle: Implications for rheology, melt extraction and the evolution of the lithosphere. *Earth and Planetary Science Letters*, 144(1-2):93–108. doi: 10.1016/0012-821X(96)00154-9.

Hutko, A. R., Lay, T., Garnero, E. J., and Revenaugh, J. (2006). Seismic detection of folded, subducted lithosphere at the core–mantle boundary. *Nature*, 441(7091):333–336. doi: 10.1038/nature04757.

Ildefonse, B., Rona, P. A., and Blackman, D. (2007). Drilling the crust at mid-ocean ridges: An "In Depth" perspective. *Oceanography*, 20(1):66–77. doi: 10.5670/oceanog.2007.81.

Irifune, T., Kubo, N., Isshiki, M., and Yamasaki, Y. (1998). Phase transformations in serpentine and transportation of water into the lower mantle. *Geophysical Research Letters*, 25(2):203–206. doi: 10.1029/97GL03572.

Janecky, D. and Seyfried, W. (1986). Hydrothermal serpentinization of peridotite within the oceanic crust: experimental investigations of mineralogy and major element chemistry. *Geochimica et Cosmochimica Acta*, 50(7):1357–1378. doi: 10.1016/0016-7037(86)90311-X.

Jessberger, E., Huneke, J., Podosek, F., and Wasserburg, G. (1974). High resolution argon analysis of neutron-irradiated Apollo 16 rocks and separated minerals. *Lunar and Planetary Science Conference Proceedings*, 5:1419–1449.

Jung, H., Green Ii, H. W., and Dobrzhinetskaya, L. F. (2004). Intermediate-depth earthquake faulting by dehydration embrittlement with negative volume change. *Nature*, 428(6982):545. doi: 10.1038/nature02412.

Kaneko, S., Miyahara, M., Ohtani, E., Arai, T., Hirao, N., and Sato, K. (2015). Letter. Discovery of stishovite in Apollo 15299 sample. *American Mineralogist*, 100(5-6):1308–1311. doi: 10.2138/am-2015-5290.

Kantor, I., Prakapenka, V., Kantor, A., Dera, P., Kurnosov, A., Sinogeikin, S., Dubrovinskaia, N., and Dubrovinsky, L. (2012). BX90: A new diamond anvil cell design for X-ray diffraction and optical measurements. *Review of Scientific Instruments*, 83(12):125102. doi: 10.1063/1.4768541.

Kanzaki, M. (1991). Stability of hydrous magnesium silicates in the mantle transition zone. *Physics of the Earth and Planetary Interiors*, 66(3-4):307–312. doi: 10.1016/0031-9201(91)90085-V.

Karato, S.-i. (2008). *Deformation of Earth Materials. An Introduction to the Rheology of Solid Earth*. Cambridge University Press. doi: 10.1017/CBO9780511804892.

Kawazoe, T., Ohira, I., Ishii, T., Ballaran, T., Mccammon, C., Suzuki, A., and Ohtani, E. (2017). Single crystal synthesis of δ-(Al,Fe)OOH. *American Mineralogist*, 102:1953–1956. doi: 10.2138/am-2017-6153.

Keppler, H. and Frost, D. (2005). Introduction to minerals under extreme conditions. In *Mineral Behaviour at Extreme Conditions*, pages 1–30. Eötvös University Press, Budapest. doi: 10.1180/EMU-notes.7.1.

King, H. E. and Finger, L. W. (1979). Diffracted beam crystal centering and its application to high-pressure crystallography. *Journal of Applied Crystallography*, 12(4):374–378. doi: 10.1107/S0021889879012723.

Klotz, S., Chervin, J.-C., Munsch, P., and Marchand, G. L. (2009). Hydrostatic limits of 11 pressure transmitting media. *Journal of Physics D: Applied Physics*, 42(7):075413. doi: 10.1088/0022-3727/42/7/075413.

Kohlstedt, D., Keppler, H., and Rubie, D. (1996). Solubility of water in the α, β and γ phases of $(Mg,Fe)_2SiO_4$. *Contributions to Mineralogy and Petrology*, 123(4):345–357. doi: 10.1007/s004100050161.

Komabayashi, T., Omori, S., and Maruyama, S. (2005). Experimental and theoretical study of stability of dense hydrous magnesium silicates in the deep upper mantle. *Physics of the Earth and Planetary Interiors*, 153(4):191–209. doi: 10.1016/j.pepi.2005.07.001.

Kudoh, Y., Finger, L., Hazen, R., Prewitt, C., Kanzaki, M., and Veblen, D. (1993). Phase E: A high pressure hydrous silicate with unique crystal chemistry. *Physics and Chemistry of Minerals*, 19(6):357–360. doi: 10.1007/BF00202972.

Kuribayashi, T., Sano-Furukawa, A., and Nagase, T. (2014). Observation of pressure-induced phase transition of δ-AlOOH by using single-crystal synchrotron X-ray diffraction method. *Physics and Chemistry of Minerals*, 41(4):303–312. doi: 10.1007/s00269-013-0649-6.

Kurnosov, A., Kantor, I., Boffa Ballaran, T., Lindhardt, S., Dubrovinsky, L., Kuznetsov, A., and Zehnder, B. H. (2008). A novel gas-loading system for mechanically closing of various types of diamond anvil cells. *Review of Scientific Instruments*, 79(4):045110. doi: 10.1063/1.2902506.

Kurnosov, A., Marquardt, H., Frost, D. J., Ballaran, T. B., and Ziberna, L. (2017). Evidence for a Fe^{3+}-rich pyrolitic lower mantle from (Al,Fe)-bearing bridgmanite elasticity data. *Nature*, 543(7646):543–546. doi: 10.1038/nature21390.

Langenhorst, F. and Hornemann, U. (2005). Shock experiments on minerals: Basic physics and techniques. In *EMU Notes in Mineralogy 7(15)*, pages 357–387. Heidelberg, Germany. doi: 10.1180/EMU-notes.7.15.

Lécuyer, C., Gillet, P., and Robert, F. (1998). The hydrogen isotope composition of seawater and the global water cycle. *Chemical Geology*, 145(3-4):249–261. doi: 10.1016/S0009-2541(97)00146-0.

Lindsay, S. M., Anderson, M. W., and Sandercock, J. R. (1981). Construction and alignment of a high performance multipass vernier tandem Fabry–Perot interferometer. *Review of Scientific Instruments*, 52(10):1478–1486. doi: 10.1063/1.1136479.

Litasov, K. D. and Ohtani, E. (2007). Effect of water on the phase relations in Earth's mantle and deep water cycle. In *Advances in High Pressure Mineralogy*, volume 421, pages 115–156. Geological Society of America. doi: 10.1130/2007.2421(08).

Liu, L.-g., Okamoto, K., Yang, Y.-j., Chen, C.-c., and Lin, C.-C. (2004). Elasticity of single-crystal phase D (a dense hydrous magnesium silicate) by Brillouin spectroscopy. *Solid State Communications*, 132(8):517–520. doi: 10.1016/j.ssc.2004.09.005.

Liu, X., Matsukage, K. N., Nishihara, Y., Suzuki, T., and Takahashi, E. (2019). Stability of the hydrous phases of Al-rich phase D and Al-rich phase H in deep subducted oceanic crust. *American Mineralogist*, 104(1):64–72. doi: 10.2138/am-2019-6559.

Lucey, P., Korotev, R., Gillis, J., Taylor, L., Lawrence, D., Campbell, B., Elphic, R., Feldman, B., Hood, L., Hunten, D., Mendillo, M., Noble, S., Papike, J., Reedy, R., Lawson, S., Prettyman, T., Gasnault, O., and Maurice, S. (2006). Understanding the lunar surface and Space-Moon interactions. *Reviews in Mineralogy and Geochemistry*, 60:83–220. doi: 10.1515/9781501509537-006.

Mainprice, D. and Ildefonse, B. (2009). Seismic anisotropy of subduction zone minerals–contribution of hydrous phases. In *Subduction Zone Geodynamics*, pages 63–84. Springer. doi: 10.1007/978-3-540-87974-9.

Mao, H. K., Xu, J., and Bell, P. M. (1986). Calibration of the ruby pressure gauge to 800 kbar under quasi-hydrostatic conditions. *Journal of Geophysical Research: Solid Earth*, 91(B5):4673–4676. doi: 10.1029/JB091iB05p04673.

Marchi, S., Bottke, W. F., Elkins-Tanton, L. T., Bierhaus, M., Wuennemann, K., Morbidelli, A., and Kring, D. A. (2014). Widespread mixing and burial of Earth's Hadean crust by asteroid impacts. *Nature*, 511(7511):578–582. doi: 10.1038/nature13539.

Marquardt, H. and Marquardt, K. (2012). Focused ion beam preparation and characterization of single-crystal samples for high-pressure experiments in the diamond-anvil cell. *American Mineralogist*, 97(2-3):299–304. doi: 10.2138/am.2012.3911.

Marquardt, H., Speziale, S., Reichmann, H. J., Frost, D. J., Schilling, F. R., and Garnero, E. J. (2009). Elastic shear anisotropy of ferropericlase in Earth's lower mantle. *Science*, 324(5924):224–226. doi: 10.1126/science.1169365.

Marty, B. (2012). The origins and concentrations of water, carbon, nitrogen and noble gases on Earth. *Earth and Planetary Science Letters*, 313-314:56–66. doi: 10.1016/j.epsl.2011.10.040.

Mashino, I., Murakami, M., and Ohtani, E. (2016). Sound velocities of δ-AlOOH up to core-mantle boundary pressures with implications for the seismic anomalies in the deep mantle. *Journal of Geophysical Research: Solid Earth*, 121(2):595–609. doi: 10.1002/2015JB012477.

McKay, D., Bogard, D., Morris, R., Korotev, R., Wentworth, S., and Johnson, P. (1989). Apollo 15 regolith breccias: window to a KREEP regolith. *Lunar and Planetary Science Conference Proceedings*, 19:19–41.

Meier, T., Petitgirard, S., Khandarkhaeva, S., and Dubrovinsky, L. (2018). Observation of nuclear quantum effects and hydrogen bond symmetrisation in high pressure ice. *Nature Communications*, 9(1):1–7. doi: 10.1038/s41467-018-05164-x.

Melosh, H. (1989). *Impact cratering : A geologic process*. New York, Oxford University Press. doi: 10.1017/S0016756800007068.

Melosh, H. (2013). The contact and compression stage of impact cratering. In *Impact cratering: Processes and products*, pages 32–42. Wiley-Blackwell.

Menikoff, R. (2007). Empirical equations of state for solids. In *ShockWave Science and Technology Reference Library*, pages 143–188. Springer, Berlin, Heidelberg. doi: 10.1007/978-3-540-68408-4.

Mercer, C. M., Young, K. E., Weirich, J. R., Hodges, K. V., Jolliff, B. L., Wartho, J.-A., and van Soest, M. C. (2015). Refining lunar impact chronology through high spatial resolution 40Ar/39Ar dating of impact melts. *Science Advances*, 1(1). doi: 10.1126/sciadv.1400050.

Michibayashi, K., Tasaka, M., Ohara, Y., Ishii, T., Okamoto, A., and Fryer, P. (2007). Variable microstructure of peridotite samples from the southern Mariana Trench: Evidence of a complex tectonic evolution. *Tectonophysics*, 444(1):111–118. doi: 10.1016/j.tecto.2007.08.010.

Miyahara, M., Kaneko, S., Ohtani, E., Sakai, T., Nagase, T., Kayama, M., Nishido, H., and Hirao, N. (2013). Discovery of seifertite in a shocked lunar meteorite. *Nature Communications*, 4(1):1737. doi: 10.1038/ncomms2733.

Miyahara, M., Ohtani, E., Goresy, A. E., Ozawa, S., and Gillet, P. (2016). Phase transition processes of olivine in the shocked Martian meteorite Tissint: Clues to origin of ringwoodite-, bridgmanite- and magnesiowüstite-bearing assemblages. *Physics of the Earth and Planetary Interiors*, 259:18 – 28. doi: 10.1016/j.pepi.2016.08.006.

Miyahara, M., Ohtani, E., Ozawa, S., Kimura, M., El Goresy, A., Sakai, T., Nagase, T., Hiraga, K., Hirao, N., and Ohishi, Y. (2011). Natural dissociation of olivine to (Mg,Fe)SiO_3 perovskite and magnesiowüstite in a shocked Martian meteorite. *Proceedings of the National Academy of Sciences*, 108(15):5999–6003. doi: 10.1073/pnas.1016921108.

Morbidelli, A., Chambers, J., Lunine, J. I., Petit, J. M., Robert, F., Valsecchi, G. B., and Cyr, K. E. (2000). Source regions and timescales for the delivery of water to the Earth. *Meteoritics & Planetary Science*, 35(6):1309–1320. doi: 10.1111/j.1945-5100.2000.tb01518.x.

Namouni, F., Luciani, J.-F., and Pellat, R. (1996). The formation of planetary cores: a numerical approach. *Astronomy and Astrophysics - A&A*, 307:972–980.

Nastasi, M., Mayer, J., and Hirvonen, J. K. (1996). *Ion-Solid Interactions: Fundamentals and Applications*. Cambridge University Press. doi: 10.1017/CBO9780511565007.

Neukum, G. and Ivanov, B. (1994). Crater size distributions and impact probabilities on Earth from lunar, terrestrial planeta, and asteroid cratering data. In *Hazards Due to Comets and Asteroids*, pages 359–416. University of Arizona Press.

Newbury, D. E. and Ritchie, N. W. (2013). Is Scanning Electron Microscopy/Energy Dispersive X-ray Spectrometry (SEM/EDS) quantitative? *Scanning*, 35(3):141–168. doi: 10.1002/sca.21041.

Nishi, M., Irifune, T., Tsuchiya, J., Tange, Y., Nishihara, Y., Fujino, K., and Higo, Y. (2014). Stability of hydrous silicate at high pressures and water transport to the deep lower mantle. *Nature Geoscience*, 7(3):224–227. doi: 10.1038/ngeo2074.

Nishi, M., Kuwayama, Y., Tsuchiya, J., and Tsuchiya, T. (2017). The pyrite-type high-pressure form of FeOOH. *Nature*, 547(7662):205–208. doi: 10.1038/nature22823.

Nishi, M., Tsuchiya, J., Kuwayama, Y., Arimoto, T., Tange, Y., Higo, Y., Hatakeyama, T., and Irifune, T. (2019). Solid solution and compression behavior of hydroxides in the lower mantle. *Journal of Geophysical Research: Solid Earth*, 124(10):10231–10239. doi: 10.1029/2019JB018146.

Nutman, A. P., Bennett, V. C., Friend, C. R., Van Kranendonk, M. J., and Chivas, A. R. (2016). Rapid emergence of life shown by discovery of 3,700-million-year-old microbial structures. *Nature*, 537(7621):535–538. doi: 10.1038/nature19355.

Nye, J. (1957). *Physical Properties of Crystals: Their Representation by Tensors and Matrices*. Oxford University Press.

O'Brien, D. P., Izidoro, A., Jacobson, S. A., Raymond, S. N., and Rubie, D. C. (2018). The delivery of water during terrestrial planet formation. *Space Science Reviews*, 214(1):47. doi: 10.1007/s11214-018-0475-8.

Ohira, I., Jackson, J. M., Solomatova, N. V., Sturhahn, W., Finkelstein, G. J., Kamada, S., Kawazoe, T., Maeda, F., Hirao, N., Nakano, S., Toellner, T. S., Suzuki, A., and Ohtani, E. (2019). Compressional behavior and spin state of δ-(Al,Fe)OOH at high pressures. *American Mineralogist*, 104(9):1273–1284. doi: 10.2138/am-2019-6913.

Ohtani, E. (2005). Water in the mantle. *Elements*, 1(1):25–30. doi: 10.2113/gselements.1.1.25.

Ohtani, E., Litasov, K., Hosoya, T., Kubo, T., and Kondo, T. (2004). Water transport into the deep mantle and formation of a hydrous transition zone. *Physics of the Earth and Planetary Interiors*, 143-144:255–269. doi: 10.1016/j.pepi.2003.09.015.

Ohtani, E., Litasov, K., Suzuki, A., and Kondo, T. (2001). Stability field of new hydrous phase, δ-AlOOH, with implications for water transport into the deep mantle. *Geophysical Research Letters*, 28(20):3991–3993. doi: 10.1029/2001GL013397.

Orloff, J., Utlaut, M., Swanson, L., and Wagner, A. (2003). *High resolution focused ion beams: FIB and its applications*. Kluwer Academic/Plenum Publisher.

Osinski, G. R. and Pierazzo, E. (2013). Impact cratering: Processes and products. In *Impact cratering: Processes and products*, page 1–20. University Arizona Press. doi: 10.1002/9781118447307.

Owen, T. and Bar-Nun, A. (1995). Comets, impacts, and atmospheres. *Icarus*, 116(2):215 – 226. doi: 10.1006/icar.1995.1122.

Ozawa, S., Ohtani, E., Miyahara, M., Suzuki, A., Kimura, M., and Ito, Y. (2009). Transformation textures, mechanisms of formation of high-pressure minerals in shock melt veins of L6 chondrites, and pressure-temperature conditions of the shock events. *Meteoritics & Planetary Science*, 44(11):1771–1786. doi: 10.1111/j.1945-5100.2009.tb01206.x.

Pacalo, R. E. G. and Weidner, D. J. (1996). Elasticity of superhydrous B. *Physics and Chemistry of Minerals*, 23(8):520–525. doi: 10.1007/BF00242001.

Pamato, M., Myhill, B., Ballaran, T., Frost, D., Heidelbach, F., and Miyajima, N. (2015). Lower-mantle water reservoir implied by the extreme stability of a hydrous aluminosilicate. *Nature Geoscience*, 8:75–79. doi: 10.1038/ngeo2306.

Peacock, S. M. (1990). Fluid processes in subduction zones. *Science*, 248(4953):329–337. doi: 10.1126/science.248.4953.329.

Pearson, D., Brenker, F., Nestola, F., McNeill, J., Nasdala, L., Hutchison, M., Matveev, S., Mather, K., Silversmit, G., Schmitz, S., et al. (2014). Hydrous mantle transition zone indicated by ringwoodite included within diamond. *Nature*, 507(7491):221–224. doi: 10.1038/nature13080.

Pennycook, S. J. and Jesson, D. E. (1990). High-resolution incoherent imaging of crystals. *Physical Review Letters*, 64:938–941. doi: 10.1103/PhysRevLett.64.938.

Pillai, S. B., Jha, P. K., Padmalal, A., Maurya, D. M., and Chamyal, L. S. (2018). First principles study of hydrogen bond symmetrization in δ-AlOOH. *Journal of Applied Physics*, 123(11):115901. doi: 10.1063/1.5019586.

Poirier, J.-P. (2000). *Introduction to the Physics of the Earth's Interior*. Cambridge University Press. doi: 10.1017/CBO9781139164467.

Presnall, D. C. and Walter, M. J. (1993). Melting of forsterite, Mg_2SiO_4, from 9.7 to 16.5 GPa. *Journal of Geophysical Research: Solid Earth*, 98(B11):19777–19783. doi: 10.1029/93JB01007.

Reed, S. J. B. (2005). *Electron Microprobe Analysis and Scanning Electron Microscopy in Geology*. Cambridge University Press. doi: 10.1017/CBO9780511610561.

Rosa, A. D., Sanchez-Valle, C., and Ghosh, S. (2012). Elasticity of phase D and implication for the degree of hydration of deep subducted slabs. *Geophysical Research Letters*, 39(6). doi: 10.1029/2012GL050927.

Rosa, A. D., Sanchez-Valle, C., Wang, J., and Saikia, A. (2015). Elasticity of superhydrous phase B, seismic anomalies in cold slabs and implications for deep water transport. *Physics of the Earth and Planetary Interiors*, 243:30 – 43. doi: 10.1016/j.pepi.2015.03.009.

Ryder, G., Koeberl, C., and Mojzsis, S. J. (2000). Heavy bombardment of the Earth at 3.85 Ga: The search for petrographic and geochemical evidence. In *Origin of the Earth and Moon*, volume 475, pages 475–492. University of Arizona Press.

Sanchez-Valle, C., Sinogeikin, S. V., Smyth, J. R., and Bass, J. D. (2006). Single-crystal elastic properties of dense hydrous magnesium silicate phase A. *American Mineralogist*, 91(5-6):961–964. doi: 10.2138/am.2006.2193.

Sanchez-Valle, C., Sinogeikin, S. V., Smyth, J. R., and Bass, J. D. (2008). Sound velocities and elasticity of DHMS phase A to high pressure and implications for seismic velocities and anisotropy in subducted slabs. *Physics of the Earth and Planetary Interiors*, 170(3):229 – 239. doi: 10.1016/j.pepi.2008.07.015.

Sano, A., Ohtani, E., Kubo, T., and Funakoshi, K. (2004). In situ X-ray observation of decomposition of hydrous aluminum silicate $AlSiO_3OH$ and aluminum oxide hydroxide d-AlOOH at high pressure and temperature. *Journal of Physics and Chemistry of Solids*, 65(8):1547–1554. doi: 10.1016/j.jpcs.2003.12.015.

Sano-Furukawa, A., Hattori, T., Komatsu, K., Kagi, H., Nagai, T., Molaison, J. J., dos Santos, A. M., and Tulk, C. A. (2018). Direct observation of symmetrization of hydrogen bond in δ-AlOOH under mantle conditions using neutron diffraction. *Scientific Reports*, 8(1):1–9. doi: 10.1038/s41598-018-33598-2.

Sano-Furukawa, A., Kagi, H., Nagai, T., Nakano, S., Fukura, S., Ushijima, D., Iizuka, R., Ohtani, E., and Yagi, T. (2009). Change in compressibility of δ-AlOOH and δ-AlOOD at high pressure: A study of isotope effect and hydrogen-bond symmetrization. *American Mineralogist*, 94(8-9):1255–1261. doi: 10.2138/am.2009.3109.

Sano-Furukawa, A., Ohtani, E., Kondo, T., Hirao, N., Sakai, T., Sata, N., Ohishi, Y., and Kikegawa, T. (2008). Aluminous hydrous mineral δ-AlOOH as a carrier of hydrogen into the core-mantle boundary. *Geophysical Research Letters*, 35(3). doi: 10.1029/2007GL031718.

Schaeffer, G. and Schaeffer, O. (1977). $^{39}Ar/^{40}Ar$ of lunar rocks. *Lunar and Planetary Science Conference Proceedings*, 8:2253–2300.

Schlichting, H. E., Sari, R., and Yalinewich, A. (2015). Atmospheric mass loss during planet formation: The importance of planetesimal impacts. *Icarus*, 247:81 – 94. doi: 10.1016/j.icarus.2014.09.053.

Schmidt, M. W. and Poli, S. (1998). Experimentally based water budgets for dehydrating slabs and consequences for arc magma generation. *Earth and Planetary Science Letters*, 163(1):361–379. doi: 10.1016/S0012-821X(98)00142-3.

Schmitt, D. R. and Ahrens, T. J. (1983). Temperatures of shock-induced shear instabilities and their relationship to fusion curves. *Geophysical Research Letters*, 10(11):1077–1080. doi: 10.1029/GL010i011p01077.

Schulze, K., Buchen, J., Marquardt, K., and Marquardt, H. (2017). Multi-sample loading technique for comparative physical property measurements in the diamond-anvil cell. *High Pressure Research*, 37(2):159–169. doi: 10.1080/08957959.2017.1299719.

Schulze, K., Marquardt, H., Kawazoe, T., Ballaran, T. B., McCammon, C., Koch-Müller, M., Kurnosov, A., and Marquardt, K. (2018). Seismically invisible water in Earth's transition zone? *Earth and Planetary Science Letters*, 498:9 – 16. doi: 10.1016/j.epsl.2018.06.021.

Sleep, N. H., Zahnle, K. J., Kasting, J. F., and Morowitz, H. J. (1989). Annihilation of ecosystems by large asteroid impacts on the early Earth. *Nature*, 342(6246):139–142. doi: 10.1038/342139a0.

Speziale, S., Marquardt, H., and Duffy, T. S. (2014). Brillouin scattering and its application in Geosciences. *Reviews in Mineralogy and Geochemistry*, 78(1):543–603. doi: 10.2138/rmg.2014.78.14.

Spurr, J. (1949). *Geology Applied to Selenology*. Rumford.

Stöffler, D. (2006). Cratering history and lunar chronology. *Reviews in Mineralogy and Geochemistry*, 60:519–596. doi: 10.2138/rmg.2006.60.05.

Stixrude, L. and Lithgow-Bertelloni, C. (2005). Thermodynamics of mantle minerals — I. Physical properties. *Geophysical Journal International*, 162(2):610–632. doi: 10.1111/j.1365-246X.2005.02642.x.

Stöffler, D. (2006). Cratering history and lunar chronology. *Reviews in Mineralogy and Geochemistry*, 60:519–596. doi: 10.2138/rmg.2006.60.05.

Stöffler, D. and Ryder, G. (2001). Stratigraphy and isotope ages of lunar geologic units: Chronological standard for the inner solar system. In *Chronology and evolution of Mars*, pages 9–54. Springer.

Swann, G., Bailey, N., Batson, R., Freeman, V., Hait, M., Head, J., Holt, H., Howard, K., Irwin, J., Larson, K., et al. (1972). Apollo 15 preliminary science report. *NASA SP-289*, pages 5–1–5–112.

Tera, F., Papanastassiou, D. A., and Wasserburg, G. J. (1974). Isotopic evidence for a terminal lunar cataclysm. *Earth and Planetary Science Letters*, 22(1):1–21. doi: 10.1016/0012-821X(74)90059-4.

Thompson, A. B. (1992). Water in the Earth's upper mantle. *Nature*, 358(6384):295–302. doi: 10.1038/358295a0.

Tomioka, N., Okuchi, T., Purevjav, N., Abe, J., and Harjo, S. (2016). Hydrogen sites in the dense hydrous magnesian silicate phase E: A pulsed neutron powder diffraction study. *Physics and Chemistry of Minerals*, 43(4):267–275. doi: 10.1007/s00269-015-0791-4.

Trots, D. M., Kurnosov, A., Ballaran, T. B., Tkachev, S., Zhuravlev, K., Prakapenka, V., Berkowski, M., and Frost, D. J. (2013). The Sm:YAG primary fluorescence pressure scale. *Journal of Geophysical Research: Solid Earth*, 118(11):5805–5813. doi: 10.1002/2013JB010519.

Trots, D. M., Kurnosov, A., Vasylechko, L., Berkowski, M., Boffa Ballaran, T., and Frost, D. J. (2011). Elasticity and equation of state of $Li_2B_4O_7$. *Physics and Chemistry of Minerals*, 38(7):561. doi: 10.1007/s00269-011-0428-1.

Tschauner, O., Huang, S., Greenberg, E., Prakapenka, V. B., Ma, C., Rossman, G. R., Shen, A. H., Zhang, D., Newville, M., Lanzirotti, A., and Tait, K. (2018). Ice-VII inclusions in diamonds: Evidence for aqueous fluid in Earth's deep mantle. *Science*, 359(6380):1136–1139. doi: 10.1126/science.aao3030.

Tsuchiya, J. and Tsuchiya, T. (2009). Elastic properties of δ-AlOOH under pressure: First principles investigation. *Physics of The Earth and Planetary Interiors*, 174:122–127. doi: 10.1016/j.pepi.2009.01.008.

Turner, G., Cadogan, P., and Yonge, C. J. (1973). Argon selenochronology. *Lunar and Planetary Science Conference Proceedings*, 4:1889.

Ulmer, P. and Trommsdorff, V. (1995). Serpentine stability to mantle depths and subduction-related magmatism. *Science*, 268(5212):858–861. doi: 10.1126/science.268.5212.858.

Van Keken, P. E., Hauri, E. H., and Ballentine, C. J. (2002). Mantle mixing: The generation, preservation, and destruction of chemical heterogeneity. *Annual Review of Earth and Planetary Sciences*, 30(1):493–525. doi: 10.1146/annurev.earth.30.091201.141236.

Walsh, K. J., Morbidelli, A., Raymond, S. N., O'Brien, D. P., and Mandell, A. M. (2011). A low mass for Mars from Jupiter's early gas-driven migration. *Nature*, 475(7355):206–209. doi: 10.1038/nature10201.

Warren, P. and Taylor, G. (2014). The Moon. In *Treatise on Geochemistry*, pages 213–242. Elsevier.

Watt, J. P., Davies, G. F., and O'Connell, R. J. (1976). The elastic properties of composite materials. *Reviews of Geophysics*, 14(4):541–563. doi: 10.1029/RG014i004p00541.

Weidenschilling, S. J., Spaute, D., Davis, D. R., Marzari, F., and Ohtsuki, K. (1997). Accretional evolution of a planetesimal swarm. *Icarus*, 128(2):429–455. doi: 10.1006/icar.1997.5747.

Wetherill, G. W. (1975). Late heavy bombardment of the moon and terrestrial planets. *Lunar and Planetary Science Conference Proceedings*, 6:1539–1561.

Whitfield, C. H., Brody, E. M., and Bassett, W. A. (1976). Elastic moduli of NaCl by Brillouin scattering at high pressure in a diamond anvil cell. *Review of Scientific Instruments*, 47(8):942–947. doi: 10.1063/1.1134778.

Wilhelms, D. E., John, F., and Trask, N. J. (1987). *The Geologic History of the Moon*. United States Government Printing Office.

Williams, D. B. and Carter, C. B. (1996). *Transmission Electron Microscopy: A Textbook for Materials Science*. Springer.

Wirth, R. (2009). Focused Ion Beam (FIB) combined with SEM and TEM: Advanced analytical tools for studies of chemical composition, microstructure and crystal structure in geomaterials on a nanometre scale. *Chemical Geology*, 261(3-4):217–229. doi: 10.1016/j.chemgeo.2008.05.019.

Wirth, R., Vollmer, C., Brenker, F., Matsyuk, S., and Kaminsky, F. (2007). Inclusions of nanocrystalline hydrous aluminium silicate "Phase Egg" in superdeep diamonds from Juina (Mato Grosso State, Brazil). *Earth and Planetary Science Letters*, 259(3):384 – 399. doi: 10.1016/j.epsl.2007.04.041.

Xu, C., Nishi, M., and Inoue, T. (2019). Solubility behavior of δ-AlOOH and ε-FeOOH at high pressures. *American Mineralogist*, 104(10):1416–1420. doi: 10.2138/am-2019-7064.

Zha, C.-s., Duffy, T. S., Downs, R. T., Mao, H.-k., and Hemley, R. J. (1998). Brillouin scattering and X-ray diffraction of San Carlos olivine: direct pressure determination to 32 GPa. *Earth and Planetary Science Letters*, 159(1):25–33. doi: 10.1016/S0012-821X(98)00063-6.

Zhao, D. (2015). Subduction zone tomography. In *Multiscale Seismic Tomography*, pages 55–95. Springer Japan. doi: 10.1007/978-4-431-55360-1_3.

4 | Satta *et al.*, Submitted Manuscript

Confidential manuscript submitted to *PNAS*

Natural Incongruent Melting of Olivine in a Regolith Breccia Provides New Insights for Collisions on the Moon's Surface

Niccolò Satta[1,*], Masaaki Miyahara[2], Shin Ozawa[3], Hauke Marquardt[4], Masahiko Nishijima[5], Tomoko Arai[6] and Eiji Ohtani[3]

[1]Bayerisches Geoinstitut, Universität Bayreuth, D-95440 Bayreuth, Germany

[2]Department of Earth and Planetary Systems Science, Graduate School of Science, Hiroshima University, Higashi-Hiroshima 739-8526, Japan

[3]Department of Earth Science, Graduate School of Science, Tohoku University, Sendai 980-8578, Japan

[4]Department of Earth Sciences, University of Oxford, Oxford OX1 3AN, United Kingdom

[5]Institute for Materials Research, Tohoku University, Sendai 980-8577, Japan

[6]Planetary Exploration Research Center, Chiba Institute of Technology, Chiba 275-0016, Japan

Corresponding author: Niccolò Satta (niccolo.satta@uni-bayreuth.de)

Significance Statement

The present-day architecture of the Solar System is the result of countless collisions between cosmic bodies. During impacts, the energy released by shock waves triggers pressures and temperatures comparable to those of planetary interiors. Minerals can form during impacts, and through their identification, it is possible to establish impact pressure and temperature conditions. In this study, we describe the presence of the mineral ferropericlase (typically confined to depths >660 km in the Earth), found in a lunar rock. The lunar ferropericlase formed as result of a shock-induced process never observed before in natural samples. This study provides a new understanding for impacts on the Moon's surface, and has implications regarding the present knowledge of the evolution of the Earth-Moon system.

Abstract

The Apollo 15 mission has returned various samples of regolith breccias to the Earth – typical lunar rocks lithified by impacts on the Moon's surface. Here, we report our observations of shock-induced features recorded in the Apollo Sample 15299. We observe the presence of ferropericlase crystals confined in a shock-melt pocket, and found that their formation is related to a shock-induced incongruent melting of olivine. While predicted by experiments, this phenomenon has never been observed in a natural sample. The incongruent melting of olivine provides an important signature of melting under high-pressure conditions, and allows for tracing the pressure (P) - temperature (T) history of the studied regolith breccia during the impact event. Our results show the studied lunar breccia has been subjected to high temperatures during a low magnitude impact event. We attribute the observed impact conditions, that differ substantially from those on meteorites, to the porous nature of the lunar regolith. Our findings suggest that a re-evaluation of the current ^{40}Ar- ^{39}Ar database is necessary to constrain the age of the main lunar impact basins.

Introduction

The formation and evolution of planets in the Solar System, and likely beyond, is largely controlled by collisional processes. Collisions between rocky bodies trigger propagating shock waves that cause a temporary, but rapid increase in pressure (P) and temperature (T). The study of mineralogical and textural features in shocked rocks can provide crucial insights into the P-T conditions triggered by impact events. The large presence of impact craters on the Moon's surface provides evidence for a long history of these events. Shock-related, high-pressure transformations have been broadly described for several different minerals in different lunar meteorites (Miyahara

et al., 2013; Ohtani et al., 2011). However, the description of high-pressure polymorphs in lunar regolith breccias is limited to a single case (Kaneko et al., 2015).

Olivine [α-$(Mg,Fe)_2SiO_4$] is the most common rock-forming mineral of Earth's upper mantle. Olivine is integral to a variety of geological processes that shape our planet, regulating surficial processes through its alteration (Moody, 1976), and playing an active role in the dynamics of the Earth's mantle (Helffrich & Wood, 2001; Karato & Wu, 1993). Along the mantle geotherm, olivine transforms into wadsleyite [β-$(Mg,Fe)_2SiO_4$] at ~ 410 kilometres depth, and wadsleyite transforms into ringwoodite [γ-$(Mg,Fe)_2SiO_4$] at larger depths (~510 km). At lower mantle depths (> 660 km), olivine dissociates to form an assemblage of (Mg,Fe)O ferropericlase + $(Mg,Fe)SiO_3$ bridgmanite at pressure >23 GPa and temperature >1900 K. Shock-induced phase transitions of olivine into wadsleyite and/or ringwoodite, as well as the dissociation into (Mg,Fe)O ferropericlase + $(Mg,Fe)SiO_3$, have been previously reported in heavily shocked meteorites and used to constrain the *P-T*-conditions of the associated impact event (Miyahara et al., 2011, 2016).

While this phase transition sequence is expected along a typical geotherm, laboratory experiments have shown that olivine can melt incongruently at pressures as low as 10 GPa when subjected to higher temperatures (> ~2200 K), eventually leading to the formation of (Mg,Fe)O ferropericlase + liquid (Ohtani et al., 1998; Presnall & Walter, 1993). The observation of an incongruent melting of olivine, however, has never been observed in any natural sample.

Materials and Methods

The Apollo section 15299,247 obtained from a chip of the Apollo sample 15299 was studied in this work. A petrographic description of the Apollo sample 15299 can be found in Juan et al. (1972). Detailed textural observations of the section were carried out using a field-emission gun

scanning electron microscope (FEG-SEM) JEOL JSM-7000F, with an accelerating voltage of 15 kV. Identification of the minerals were based on micro-Raman spectroscopy which indicated no evidence for existence of the high-pressure polymorphs of olivine and pyroxene. We employed an FIB system (FEI Quanta 200 3D) to cut and polish thin films from the original sample. In this process, a gallium (Ga^+) ion beam (accelerating voltage of 30 kV) with low-current was used to remove bulk materials and polish the TEM lamella to a final thickness of 100 nm. Polished lamella was placed on a molybdenum grid for TEM observations using a manipulator (Omni Probe) implemented in the FIB system. Charging effects were minimized by carbon-coating the original section. High-Angle Annular Dark Field (HAADF) and transmission electron images, as well as Selected Area Electron Diffraction (SAED) patterns were acquired using a transmission electron microscope (JEOL 2100F) operating at 200 kV. Both the camera length and wavelength of the electron beam for SAED analyses were calibrated using a gold particle. Chemical analyses were carried out in Scanning Transmission Electron Microscope (STEM) mode using a JEOL JEM-2100F TEM equipped with an Energy Dispersive Spectrometer (EDS). Resulting compositions were calibrated following experimentally determined *k* factors [San Carlos olivine, (Mg,Fe)O, and pyrope]. Relative standard uncertainties of the major elements are typically within the 5%.

Results and Discussion

The Apollo sample 15299 is a regolith breccia which was collected near the northern slope of the Hadley Delta during the Apollo 15 mission (Swann et al., 1972). Here we studied the polished section 15299,247 obtained from the Apollo sample 15299. This section is characterized by two distinct lithological domains: (i) a basaltic equigranular aggregate of relatively unfractured phenocrystals (~500 μm across) and (ii) a typical regolith mafic melt breccia with highly fractured,

coarse crystalline grains with small dimensions (~100 μm on average). The basaltic domain represents about 80 vol% of the here-studied section, and mainly consists of the rock-forming minerals low-Ca pyroxene and anorthitic plagioclase. Olivine is present in minor quantities, while chromite and ilmenite appear only as accessory components. Our petrographic description is consistent with previous investigations on a different polished section of the same Apollo sample 15299, in which shock-related stishovite formation was described (Kaneko et al., 2015). Under a light microscope, the polished section 15299,247 shows minor shock-induced features such as shock-melt veins (with a maximum width of 50 μm), and small shock-melt pockets (2000-3000 μm^2), Figure 1.

We focused on an isolated shock-melt pocket, confined entirely in a fractured olivine grain. The interface between the host grain and the pocket appear to be very sharp. High-magnification field emission Scanning Electron Microscopy (SEM) imaging (Figure 1b) suggests the presence of two distinct mineral assemblages located in the outer and inner region of a branch of the shock-melt pocket. In particular, the outer region, i.e. along the rim with the host olivine grain, shows the presence of two components distinguishable as bright spherules (~50 nm in diameter) and darkish grains (100-500 nm in size). On the other hand, the inner region of the pocket does not show any clear evidence of the presence of bright spherules, but only of darkish grains. The bulk compositions of the inner and outer regions, determined by SEM-Energy Dispersive Spectrometry (SEM-EDS) analyses, appear to be nearly identical to the host olivine grain (Table 1).

The internal textural features of the shock-melt pocket were exposed and imaged by transmission electron microscopy (TEM) (Figure 1c). Various areal and punctual chemical analyses were collected in scanning mode (STEM-EDS) and the results are in agreement with SEM-EDS results (Table 2). Selected Area Electron Diffraction (SAED) investigations identified the bright spherules

125 and darkish grains in the outer region of the pocket as ferropericlase and olivine crystals,
126 respectively. The darkish grains contained in the inner region were identified as olivine crystals.
127 According to the STEM-EDS results, the olivines contained in both outer and inner regions have
128 chemical compositions similar to the host olivine grain (Table 2). SAED and STEM-EDS analyses
129 determined that ferropericlase has lattice parameter a = 4.28(1) Å, and magnesium number (Mg#
130 = Mg/(Mg+Fe)x100) of 48. More information can be found in the Supplementary Information.
131 Due to the the small size of the ferropericlase grains (50 nm in average), STEM-EDS analyses
132 returned only semi-quantitative compositions. The chemical composition dependence of lattice
133 parameter in ferropericlase follows the relation constrained by previous experimental
134 investigations (Dubrovinsky et al., 2000). STEM-EDS on the outer region matrix highlighted the
135 presence of regions with a silica content that exceeds the stoichiometric amount for olivine.
136 Furthermore, these Si-rich regions (hereafter referred to as Si pockets) are enriched in Fe, therefore
137 excluding the possibility that this excess in silica arises from a convolution between olivinic and
138 pyroxenitic components. Elemental maps collected in the outer region support the STEM-EDS
139 analyses (Figure 2). The Si content decreases from silica pockets to olivine to ferropericlase. The
140 Mg-content in olivine is comparable to the one in ferropericlase, but is larger than the one in the
141 silica pockets, while the Fe content is higher in ferropericlase than in silica pockets and olivine.
142 The partitioning of Fe and Mg between ferropericlase, melt and olivine is in agreement with
143 previous experimental studies (Trønnes, 2000).
144
145 **First evidence for incongruent melting of olivine in a natural sample**
146 We observed the presence of an assemblage constituted of (Mg,Fe)O ferropericlase +
147 $(Mg,Fe)_2SiO_4$ olivine along the interface between a shock-melt pocket and its host olivine. The

chemical similarity between the host olivine and the olivine crystals entrained in the shock-melt pocket suggests that the latter are fragments of the host grain. Natural ferropericlase in shocked samples has been thus far interpreted to be the result of (i) the crystallization from a melt (Chen et al., 1996), or (ii) solid state reactions (Miyahara et al., 2011). TEM observations indicate that the here-studied shock-melt pocket does not show any chemical or textural features which support the presence of an either vitreous or crystalline $(Mg,Fe)SiO_3$ component. Therefore, it is unlikely that the ferropericlase crystallized from a congruent melt. Furthermore, the nm-size nature of the (Mg,Fe)O ferropericlase crystals accounts for a rapid solidification of the shock-melt pocket. In fact, given its branched geometry, and a thickness of about 10 μm, the shock-melt pocket would have most likely quenched by heat conduction within microseconds, and before shock pressure release (Langenhorst & Poirier, 2000; Shaw & Walton, 2013). We found that Fe was partitioned into (Mg,Fe)O ferropericlase, implying that atomic diffusion occured during the formation of ferropericlase. This suggests that (Mg,Fe)O ferropericlase did not form as dissociation product of $(Mg,Fe)_2SiO_4$ polymorphs, but rather, was the result of the crystallization from a melt. Moreover, natural wadsleyite and ringwoodite crystals are typically found within shock-induced features and along grain boundaries (Chen et al., 2004; Yin et al., 2018). The microsecond-quench of the studied shock-melt pocket would have inhibited the back transformation of these high-pressure polymorphs into olivine, which occurs on the time-scale of seconds (Chen et al., 1998). We found no evidence supporting the presence of wadsleyite and/or ringwoodite, nor their back transformation into olivine. Therefore, it is likely that the conditions necessary for their formation were not reached during the impact event. All the above observations indicate a different process leading to ferropericlase formation in our sample. We infer that this process is the formation from an incongruent melt of olivine, which has been documented by experiments to occur at relatively

low pressure (~10 GPa) with temperatures above 2200 K (Ohtani et al., 1998; Presnall & Walter, 1993). This process would allow (Mg,Fe)O ferropericlase to form from the incongruent melt, which enables efficient chemical equilibration, retaining the silica component in the fluid. Our hypothesis is consistent with all the observations, in particular the absence of a $(Mg,Fe)SiO_3$ component and γ-, β-polymorphs of olivine. Our hypothesis is further supported by the presence of Si pockets within the (Mg,Fe)O ferropericlase + $(Mg,Fe)_2SiO_4$ olivine assemblage, which were identified along the interface with the host olivine grain. We therefore conclude that (Mg,Fe)O ferropericlase formed as result of the incongruent melting of olivine before pressure release, while the Si pockets indicate a quenched fluid resulting from the melting process. This finding constitutes the first documentation of incongruent melting of olivine in any natural sample and puts tight constraints on the *P-T* conditions reached during the impact event.

Impact conditions and implication for the collisional history of the Moon

The incongruent melting of $(Mg,Fe)_2SiO_4$ olivine is confined to a small *P-T* region (Ohtani et al., 1998; Presnall & Walter, 1993). Therefore, the presence of the (Mg,Fe)O ferropericlase + (Mg,Fe)2SiO4 olivine assemblage within the shock-melt pocket tightly constrains the *P-T* conditions reached during the impact event. Figure 3 shows phase relations in the Mg_2SiO_4 system (Presnall & Walter, 1993) together with the stability field of stishovite (Schmitt & Ahrens, 1983). Based on our observations, the shock pressure can be estimated to be at least 10 GPa, while shock temperatures were at least ~2200 K. These *P-T* are consistent with the finding of stishovite, previously observed in a different polished section of the Apollo sample 15299 (Kaneko et al., 2015). Our observations therefore suggest that the Apollo 15299 sample experienced a significantly different *P-T* path with respect to those of other extra-terrestrial samples (Figure 3).

194 Across the first few kilometres depth, the Moon's surface is characterized by a layer of
195 unconsolidated and porous material, shattered by countless impact events (Huang & Wieczorek,
196 2012). Lunar rocks lithified by shock compression (i.e., regolith breccias), are characterized by
197 shock-related microfractures which cause pervasive porosities of 15-22% (Kiefer et al., 2012),
198 typically higher than those of meteorites (Consolmagno et al., 2008; Warren, 2001). We estimated
199 the fracture porosity of the basaltic domain of the investigated sample to be about 17% (Figure S1
200 and S2). The first stage of shock compression of a porous material is characterized by a collapse
201 of the initial porosity. Therefore, porosity has a strong effect on the response of a material to shock
202 compression. Thus, porosity collapse can significantly contributes to a waste heat increase,
203 enhancing the shock temperature (Sharp & De Carli, 2006). Furthermore, the textural complexity
204 of a porous material may lead to a heterogeneous distribution of the energy during shock
205 compression, resulting in localized spikes in the *P-T* conditions experienced by the material during
206 the shock event (Kieffer, 1971). Shock-melt veins and pockets commonly display a sequence of
207 microtextures and mineral assemblages that reflect a thermal gradient (i.e., the closer to the center
208 the higher the temperature (Miyahara et al., 2011). The here-studied shock-melt pocket shows an
209 unusual relation between the expected thermal evolution and the mineral assemblages contained
210 in the shock-melt pocket. In particular, the inner region of the pocket is characterized only by
211 fragments of the host olivine, while the (Mg,Fe)O ferropericlase + $(Mg,Fe)_2SiO_4$ olivine
212 assemblage is localized along the interface with the host olivine. The spatial relation between these
213 two distinct mineral assemblages suggests that the rim with the host olivine was hotter than the
214 center of the pocket, implying an unusual evolution of the temperature from the center of the
215 pocket toward the host olivine. We infer that thermal gradient and corresponding mineral
216 assemblages may be the result of a complex system of microfractures which characterized the host

grain prior to the shock event. Frictional heat associated with the collapse of the initial porosity during the shock compression, may be the cause for the localized spikes in shock temperature, enabling the olivine contained in the Apollo section 15299,247 to melt incongruently. The reconstruction of the main collisional events in the history of the Moon is mostly based on the interpretation of thermal disturbances to the ^{40}Ar-^{39}Ar system in regolith breccias (Dalrymple & Ryder, 1993, 1996; Norman et al., 2006). An exposure to elevated temperatures significantly disturbs the ^{40}Ar-^{39}Ar system by inducing a total (or partial) loss of ^{40}Ar (^{40}Ar*), that results in a total (or partial) reset of the isotopic clock. For this reason, isotopic resetting in the 40Ar-39 system can be directly linked to impact events, and help to describe the collisional history of regolith breccias (Mercer et al., 2015). Our findings demonstrate that the porous lunar regolith can be exposed to elevated temperature even during low magnitude impact events. Therefore, partial resetting in the ^{40}Ar-^{39}Ar isotopic clock recorded in regolith breccias might not require impacts of large magnitude, as previously suggested (e.g., Ryder et al., 1991). Our results imply that a re-evaluation of the current ^{40}Ar-^{39}Ar dataset that takes into account the peculiar behavior of the lunar regolith under shock compression is necessary to better constrain the collisional history of the Moon. On the other hand, our finding suggests that thermal disturbances to the ^{40}Ar-^{39}Ar system can be recorded in low-shocked regolith breccias, which therefore constitute an additional source of information to constrain the age of impact events on the Moon's surface.

Acknowledgements

We are grateful to the NASA's Johnson Space Center for providing us a chance to study the Apollo section 15299,247 with T. Arai as a primary investigator. We appreciate T. Miyazaki of Tohoku University for his assistance of the TEM works. N.Satta thanks T. Boffa Ballaran and N.

240 Miyashima of Bayeriches Geoinstitut and with their helpful discussions on TEM analyses. N. Satta
241 was supported by the International Research Training Group "Deep Earth Volatile Cycles" (GRK
242 2156/1). Eiji Ohtani was supported by Kakenhi Grant 15H05748.

243

244 **Contributions**

245 E. Ohtani, T.Arai, N. Satta and H. Marquardt conceived this study. T. Arai and E. Ohtani
246 selected the sample. N. Satta, M. Mayahara, S. Ozawa, and E. Ohtani were involved in the
247 collection, analysis and interpretation of the data. M. Nishijima operated the focused ion beam.
248 N. Satta, M. Mayahara and E. Ohtani wrote the manuscript with input from all authors.

249

250 **References**

251 Chen, M., Goresy, A. E., & Gillet, P. (2004). Ringwoodite lamellae in olivine: Clues to olivine–
252 ringwoodite phase transition mechanisms in shocked meteorites and subducting slabs.
253 *Proceedings of the National Academy of Sciences*, *101*(42), 15033–15037.
254 https://doi.org/10.1073/pnas.0405048101
255 Chen, M., Sharp, T. G., Goresy, A. E., Wopenka, B., & Xie, X. (1996). The Majorite-Pyrope +
256 Magnesiowüstite Assemblage: Constraints on the History of Shock Veins in Chondrites.
257 *Science*, *271*(5255), 1570–1573. https://doi.org/10.1126/science.271.5255.1570
258 Chen, M., Xie, X., El Goresy, A., Wopenka, B., & Sharp, T. G. (1998). Cooling rates in the
259 shock veins of chondrites: Constraints on the (Mg, Fe)2SiO4 polymorph transformations.
260 *Science in China Series D: Earth Sciences*, *41*(5), 522–528.
261 https://doi.org/10.1007/BF02877743

262 Consolmagno, G. J., Britt, D. T., & Macke, R. J. (2008). The significance of meteorite density
263 and porosity. *Geochemistry*, *68*(1), 1–29. https://doi.org/10.1016/j.chemer.2008.01.003
264 Dalrymple, G. B., & Ryder, G. (1993). ^{40}Ar/^{39}Ar age spectra of Apollo 15 impact melt rocks by
265 laser step-heating and their bearing on the history of lunar basin formation. *Journal of*
266 *Geophysical Research*, *98*(E7), 13085. https://doi.org/10.1029/93JE01222
267 Dalrymple, G. B., & Ryder, G. (1996). Argon-40/argon-39 age spectra of Apollo 17 highlands
268 breccia samples by laser step heating and the age of the Serenitatis basin. *Journal of*
269 *Geophysical Research: Planets*, *101*(E11), 26069–26084.
270 https://doi.org/10.1029/96JE02806
271 Dubrovinsky, L. S., Dubrovinskaia, N. A., Saxena, S. K., Annersten, H., Hålenius, E., Harryson,
272 H., Tutti, F., Rekhi, S., & Bihan, T. L. (2000). Stability of Ferropericlase in the Lower
273 Mantle. *Science*, *289*(5478), 430–432. https://doi.org/10.1126/science.289.5478.430
274 Helffrich, G. R., & Wood, B. J. (2001). The Earth's mantle. *Nature*, *412*(6846), 501–507.
275 https://doi.org/10.1038/35087500
276 Huang, Q., & Wieczorek, M. A. (2012). Density and porosity of the lunar crust from gravity and
277 topography. *Journal of Geophysical Research: Planets*, *117*(E5).
278 https://doi.org/10.1029/2012JE004062
279 Juan, V. C., Chen, J. C., Huang, C. K., Chen, P. Y., & Lee, C. M. W. (1972). *Petrology and*
280 *chemistry of some Apollo 15 crystalline rocks*. 110–115.
281 Kaneko, S., Miyahara, M., Ohtani, E., Arai, T., Hirao, N., & Sato, K. (2015). Discovery of
282 stishovite in Apollo 15299 sample. *American Mineralogist*, *100*(5–6), 1308–1311.
283 https://doi.org/10.2138/am-2015-5290

284 Karato, S., & Wu, P. (1993). Rheology of the Upper Mantle: A Synthesis. *Science*, *260*(5109),
285 771–778. https://doi.org/10.1126/science.260.5109.771
286 Kiefer, W. S., Macke, R. J., Britt, D. T., Irving, A. J., & Consolmagno, G. J. (2012). The density
287 and porosity of lunar rocks: THE DENSITY AND POROSITY OF LUNAR ROCKS.
288 *Geophysical Research Letters*, *39*(7), n/a-n/a. https://doi.org/10.1029/2012GL051319
289 Kieffer, S. W. (1971). Shock metamorphism of the Coconino Sandstone at Meteor Crater,
290 Arizona. *Journal of Geophysical Research (1896-1977)*, *76*(23), 5449–5473.
291 https://doi.org/10.1029/JB076i023p05449
292 Langenhorst, F., & Poirier, J.-P. (2000). Anatomy of black veins in Zagami: Clues to the
293 formation of high-pressure phases. *Earth and Planetary Science Letters*, *184*(1), 37–55.
294 https://doi.org/10.1016/S0012-821X(00)00317-4
295 Mercer, C. M., Young, K. E., Weirich, J. R., Hodges, K. V., Jolliff, B. L., Wartho, J.-A., & van
296 Soest, M. C. (2015). Refining lunar impact chronology through high spatial resolution
297 40Ar/39Ar dating of impact melts. *Science Advances*, *1*(1).
298 https://doi.org/10.1126/sciadv.1400050
299 Miyahara, M., Kaneko, S., Ohtani, E., Sakai, T., Nagase, T., Kayama, M., Nishido, H., & Hirao,
300 N. (2013). Discovery of seifertite in a shocked lunar meteorite. *Nature Communications*,
301 *4*(1), 1737. https://doi.org/10.1038/ncomms2733
302 Miyahara, M., Ohtani, E., Goresy, A. [El, Ozawa, S., & Gillet, P. (2016). Phase transition
303 processes of olivine in the shocked Martian meteorite Tissint: Clues to origin of
304 ringwoodite-, bridgmanite- and magnesiowüstite-bearing assemblages. *Physics of the*
305 *Earth and Planetary Interiors*, *259*, 18–28. https://doi.org/10.1016/j.pepi.2016.08.006

306 Miyahara, M., Ohtani, E., Ozawa, S., Kimura, M., El Goresy, A., Sakai, T., Nagase, T., Hiraga,
307 K., Hirao, N., & Ohishi, Y. (2011). Natural dissociation of olivine to (Mg,Fe)SiO3
308 perovskite and magnesiowüstite in a shocked Martian meteorite. *Proceedings of the*
309 *National Academy of Sciences*, *108*(15), 5999–6003.
310 https://doi.org/10.1073/pnas.1016921108
311 Moody, J. B. (1976). Serpentinization: A review. *Lithos*, *9*(2), 125–138.
312 Norman, M. D., Duncan, R. A., & Huard, J. J. (2006). Identifying impact events within the lunar
313 cataclysm from 40Ar–39Ar ages and compositions of Apollo 16 impact melt rocks.
314 *Geochimica et Cosmochimica Acta*, *70*(24), 6032–6049.
315 https://doi.org/10.1016/j.gca.2006.05.021
316 Ohtani, E., Moriwaki, K., Kato, T., & Onuma, K. (1998). Melting and crystal–liquid partitioning
317 in the system Mg2SiO4–Fe2SiO4 to 25 GPa. *Physics of the Earth and Planetary*
318 *Interiors*, *107*(1), 75–82. https://doi.org/10.1016/S0031-9201(97)00125-8
319 Ohtani, E., Ozawa, S., Miyahara, M., Ito, Y., Mikouchi, T., Kimura, M., Arai, T., Sato, K., &
320 Hiraga, K. (2011). Coesite and stishovite in a shocked lunar meteorite, Asuka-881757,
321 and impact events in lunar surface. *Proceedings of the National Academy of Sciences*,
322 *108*(2), 463–466. https://doi.org/10.1073/pnas.1009338108
323 Ozawa, S., Ohtani, E., Miyahara, M., Suzuki, A., Kimura, M., & Ito, Y. (2009). Transformation
324 textures, mechanisms of formation of high-pressure minerals in shock melt veins of L6
325 chondrites, and pressure-temperature conditions of the shock events. *Meteoritics &*
326 *Planetary Science*, *44*(11), 1771–1786. https://doi.org/10.1111/j.1945-
327 5100.2009.tb01206.x

328 Presnall, D. C., & Walter, M. J. (1993). Melting of forsterite, Mg2SiO4, from 9.7 to 16.5 GPa.
329 *Journal of Geophysical Research: Solid Earth*, *98*(B11), 19777–19783.
330 https://doi.org/10.1029/93JB01007
331 Ryder, G., Bogard, D., & Garrison, D. (1991). Probable age of Autolycus and calibration of lunar
332 stratigraphy. *Geology*, *19*(2), 143–146. https://doi.org/10.1130/0091-
333 7613(1991)019<0143:PAOAAC>2.3.CO;2
334 Schmitt, D. R., & Ahrens, T. J. (1983). Temperatures of shock-induced shear instabilities and
335 their relationship to fusion curves. *Geophysical Research Letters*, *10*(11), 1077–1080.
336 https://doi.org/10.1029/GL010i011p01077
337 Sharp, T. G., & De Carli, P. S. (2006). Shock Effects in Meteorites. In *Meteorites and the Early*
338 *Solar System II* (pp. 653–677). http://adsabs.harvard.edu/abs/2006mess.book..653S
339 Shaw, C. S. J., & Walton, E. (2013). Thermal modeling of shock melts in Martian meteorites:
340 Implications for preserving Martian atmospheric signatures and crystallization of high-
341 pressure minerals from shock melts. *Meteoritics & Planetary Science*, *48*(5), 758–770.
342 https://doi.org/10.1111/maps.12100
343 Swann, G. A., Bailey, N. G., Batson, R. M., Freeman, V. L., Hait, M. H., Head, J. W., Holt, H.
344 E., Howard, K. A., Irwin, J. B., Larson, K. B., Muehlberger, W. R., Reed, V. S.,
345 Rennilson, J. J., Schaber, G. G., Scott, D. R., Silver, L. T., Sutton, R. L., Ulrich, G. E.,
346 Wilshire, H. G., & Wolfe, E. W. (1972). Preliminary geologic investigation of the Apollo
347 15 landing site. In *Apollo 15 Preliminary Science Report* (Vols 5–1). National
348 Aeronautics and Space Administration.

Trønnes, R. G. (2000). Melting relations and major element partitioning in an oxidized bulk Earth model composition at 15–26 GPa. *Lithos*, *53*(3), 233–245. https://doi.org/10.1016/S0024-4937(00)00027-X

Warren, P. H. (2001). Porosities of lunar meteorites: Strength, porosity, and petrologic screening during the meteorite delivery process. *Journal of Geophysical Research: Planets*, *106*(E5), 10101–10111. https://doi.org/10.1029/2000JE001283

Yin, F., Liao, Z., Hursthouse, A., & Dai, D. (2018). Shock-Induced Olivine-Ringwoodite Transformation in the Shock Vein of Chondrite GRV053584. *Minerals*, *8*(4), 139. https://doi.org/10.3390/min8040139

359 **Table 1.** Chemical compositions obtained by SEM-EDS.

		SEM-EDS	
Oxides	**Host Ol**	**Inner region**	**Outer region**
SiO_2	37.5(2)	37.6(1)	37.6(2)
Al_2O_3	0.06(5)	0.2(1)	0.3(1)
FeO	27.9(2)	26(1)	27.8(9)
MgO	34.3(3)	35.8(1)	33.8(9)
CaO	0.2(1)	0.5(1)	0.6(1)
n	6	5	6

360 Numbers in parenthesis are standard deviations corresponding to the last digit. Analyses are normalized to

361 100%. All Fe is assumed ferrous.

362 **Table 2.** Chemical compositions obtained by STEM-EDS.

		Inner region	Outer region		
Oxides (wt%)	**Host Ol**	**Ol**	**Ol**	**Fp***	**Si pockets**
SiO_2	37.2(4)	39.1(1)	40.1(4)	-	47.3
FeO	28.3(9)	24.2(24)	24.6(11)	65.4	27.3
MgO	34.5(1)	36.7(28)	34.7(7)	34.6	24
CaO	-	-	-	-	1.4
n	2	9	2	1	1

363 Numbers in parenthesis are standard deviations corresponding to the last digit. Analyses are normalized to
364 100%. All Fe is assumed ferrous. *Computed by subtracting the matrix contribution to the comprehensive
365 composition (see Supplementary Information). - = not determined, Ol = olivine, Fp = ferropericlase.

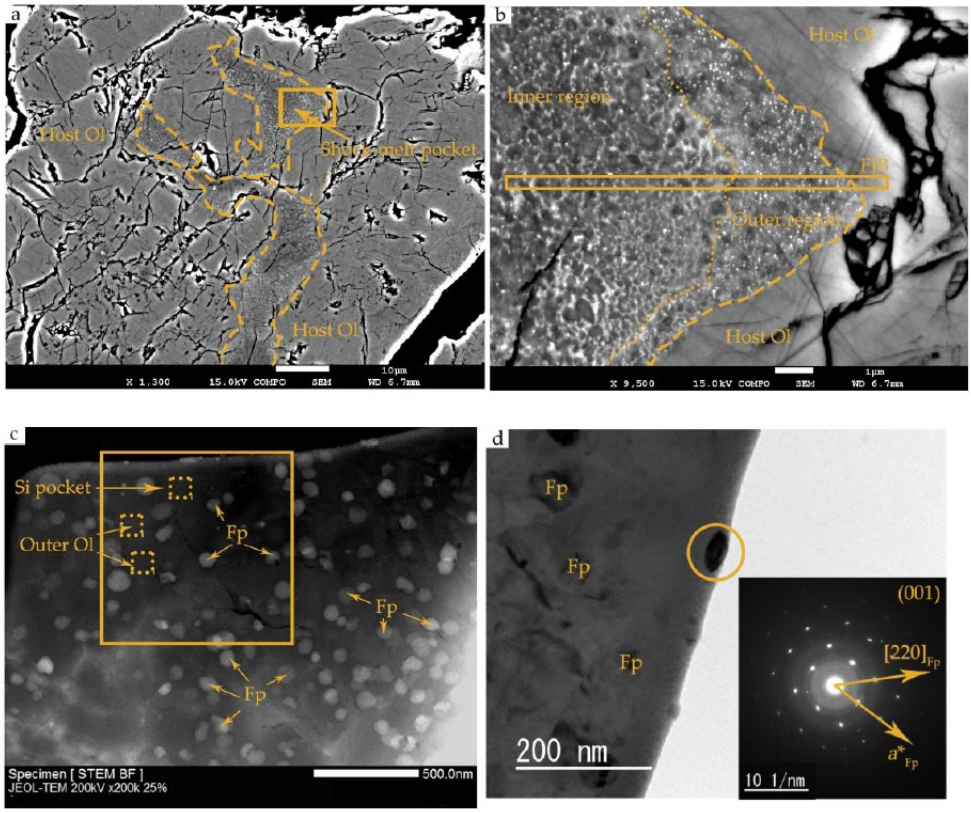

Figure 1. Field emission Scanning Electron Microscopy (SEM) and Transmission Electron Microscopy (TEM) images of the investigated shock melt pocket. a) Back-scattered Electron (BSE) image collected with a field emission SEM of the shock-melt pocket; b) High magnification BSE image of the outer and inner region of the shock-melt pocket. Mustard rectangle shows the location of the block extracted through FIB; c) High-Angle Annular Dark Field (HAADF) image collected with TEM of the FIB section exposing the micro-texture and mineralogical assemblage in the outer region of shock-melt pocket. Mustard suqare shows the area where elemental maps (Figure 2) were collected. Dashed boxes denote the location of the individual chemical analysis points listed in Table 2. Ol = olivine, Fp = ferropericlase; d) TEM image of ferropericlase crystals. Inset SAED pattern is from the ferropericlase crystal within the mustard circle.

379

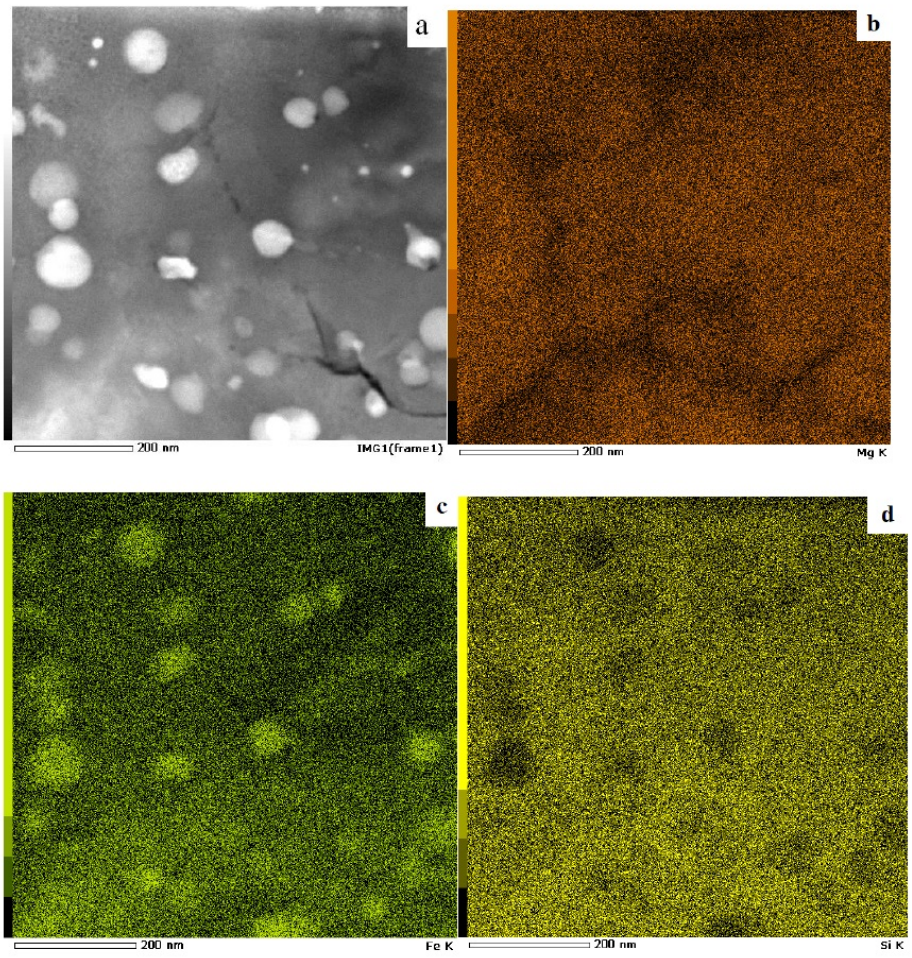

380

381

382 **Figure 2**. Transmission Electron Microscopy (TEM) image and elemental mapping of the
383 (Mg,Fe)O ferropericlase + $(Mg,Fe)_2SiO_4$ olivine assemblage contained in the shock-melt pocket
384 in the outer region of the shock-melt pocket. (a) Bright-field STEM image; (b-d) elemental
385 mapping images obtained with STEM-EDS showing the partitioning of Mg, Fe and Si in the
386 (Mg,Fe)O ferropericlase + $(Mg,Fe)_2SiO_4$ olivine assemblage.

387

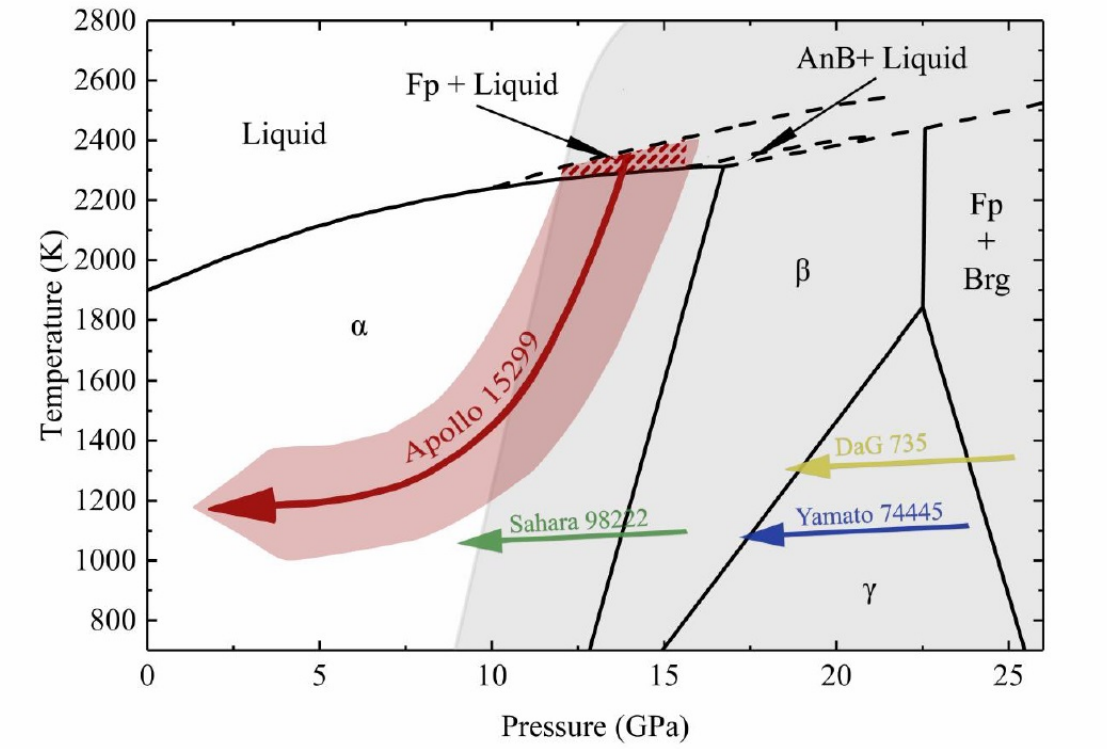

388

389 **Figure 3.** *P-T* conditions estimated from the high-pressure assemblages (patterned region in red)
390 contained in the shock-melt pocket of the Apollo sample 15299. Phase relations are from Presnal
391 et al. (1993). The light grey region in the *P-T* space represents the stability field of stishovite
392 (Schmitt & Ahrens, 1983). Shaded region in red shows a tentative *P-T* path of the Apollo sample
393 15299. Yellow, green and blue arrows represent the tentative adiabatic decompression paths of
394 shergottite - DaG 735 (Miyahara et al., 2011) and, L6 chondrites - Sahara 98222 and Yamato
395 74445 (Ozawa et al., 2009), respectively. Fp = ferropericlase, Brg = bridgmanite, α = olivine, β =
396 wadsleyite, γ = ringwoodite and AnB = anhydrous phase B.

397

4.1 Supplementary Material

Supplementary Information for

Natural Incongruent Melting of Olivine in a Regolith Breccia Provides New Insights for Collisions on the Moon's Surface

Niccolò Satta[1,*], Masaaki Miyahara[2], Shin Ozawa[3], Hauke Marquardt[4], Masahiko Nishijima[5], Tomoko Arai[6] and Eiji Ohtani[3]

[1]Bayerisches Geoinstitut, Universität Bayreuth, D-95440 Bayreuth, Germany

[2]Department of Earth and Planetary Systems Science, Graduate School of Science, Hiroshima University, Higashi-Hiroshima 739-8526, Japan

[3]Department of Earth Science, Graduate School of Science, Tohoku University, Sendai 980-8578, Japan

[4]Department of Earth Sciences, University of Oxford, Oxford OX1 3AN, United Kingdom

[5]Institute for Materials Research, Tohoku University, Sendai 980-8577, Japan

[6]Planetary Exploration Research Center, Chiba Institute of Technology, Chiba 275-0016, Japan

Corresponding author: Niccolò Satta (niccolo.satta@uni-bayreuth.de)

This PDF file includes:

Supplementary Text

Fig. S1 to S2

Tables S1 to S2

SI references

31

32 **Determination of chemical composition of ferropericlase**

33 Due the thickness of the TEM lamella (~100 nm), and to the small size of the ferropericlase grains
34 (~50 nm), the measured chemical composition determined with STEM-EDS is a convolution
35 between the contribution from the ferropericlase crystal and that of the surrounding matrix. A clear
36 suggestion for the contamination of the measured composition of ferropericlase comes from the
37 detection of Si, which should not be present in ferropericlase. A ferropericlase crystal close to the
38 rim of the lamella was selected because its measured composition showed a low Si content, hence
39 a low contamination (Table S1). A mass balance approach was applied to estimate the composition
40 of ferropericlase:

41

42 comprehensive measured composition = ferropericlase + surrounding matrix

43

44 The amount of Si (14.9 at%) detected in the measured composition of ferropericlase was assumed
45 to belong entirely to the surrounding matrix. STEM-EDS results show that the chemical
46 composition of the surrounding matrix matches the composition of the host olivine. Therefore, Mg
47 and Fe contributions to the measured composition raising from the surrounding matrix were
48 quantified following Mg/Si and Fe/Si of the host olivine. Finally, the composition of ferropericlase
49 was estimated by subtracting the contribution of the surrounding matrix to the comprehensive
50 measured composition.

51 **Determination of the lattice parameter of ferropericlase**

52 Selected Area Electron Diffraction (SAED) was employed to obtain diffraction patterns of a
53 ferropericlase grain and an olivine grain adjacent to it. According to the STEM-EDS analysis,
54 olivine grains coexisting with ferropericlase have a magnesium number of Mg# = ~68. Calculation
55 of the d-spacing for (020) and (200) reflections was done assuming a linear relation between d-
56 spacings of fayalite and forsterite end-members. We found that measured d_{020} and d_{200} of olivine
57 are systematically shifted from those calculated for an olivine with the same Mg# (Table S2). The
58 shift detected in the measured d-spacing can be a result of spherical aberration and de-focusing of
59 the objective lens. Therefore, the measured d_{020} and d_{220} of ferropericlase were corrected
60 accordingly.
61
62 **Porosity determination.**
63 Areal fracture porosity was estimated using an imaging procedure on a low-magnification SEM
64 picture of the basaltic domain. The chosen image contains the shock-melt pocket investigated in
65 this study (Figure S1). The area assigned to the fractures constitutes 17.5% of the total image
66 (Figure S2).

67 **Table S1.** Atomic % determined by STEM-EDS.

Atom %	**Measured composition**	**Surrounding matrix**	**Fp***
Si	14.9	33.6	-
Fe	37.8	20.5	51.5
Mg	47.3	45.8	48.5
Total (at%)	100	100	100

68 Atomic % are normalized to 100 %. All Fe is assumed ferrous. * Computed by subtracting the matrix
69 contribution to the comprehensive measured composition. composition. - = not determined, Fp =
70 ferropericlase.

71

71 **Table S2.** SAED results for olivine and ferropericlase.

	d_{020} (Å)	d_{200} (Å)	d_{220} (Å)
Forsterite[1]	5.1035	2.378	-
Fayalite[2]	5.2355	2.378	-
Calculated ol[3]	5.193	2.399	
Measured ol	5.5132	2.5462	
Ratio[4]	1.0616	1.0613	
Measured Fp		2.27(1)	1.60
Corrected Fp		2.14(1)	1.51

72 [1]Smyth & Hazen (1973); [2]Smyth (1975); [3]Calculated d-spacings assuming a composition with Mg# = 68,
73 and a linear variation between fayalite and forsterite end-members; [4]d-spacing ratio between measured
74 and calculated values of olivine (Mg# = 68). Numbers in parentheses are the standard deviations in the
75 last significant digit. - = not determined, Ol = olivine, Fp = ferropericlase.

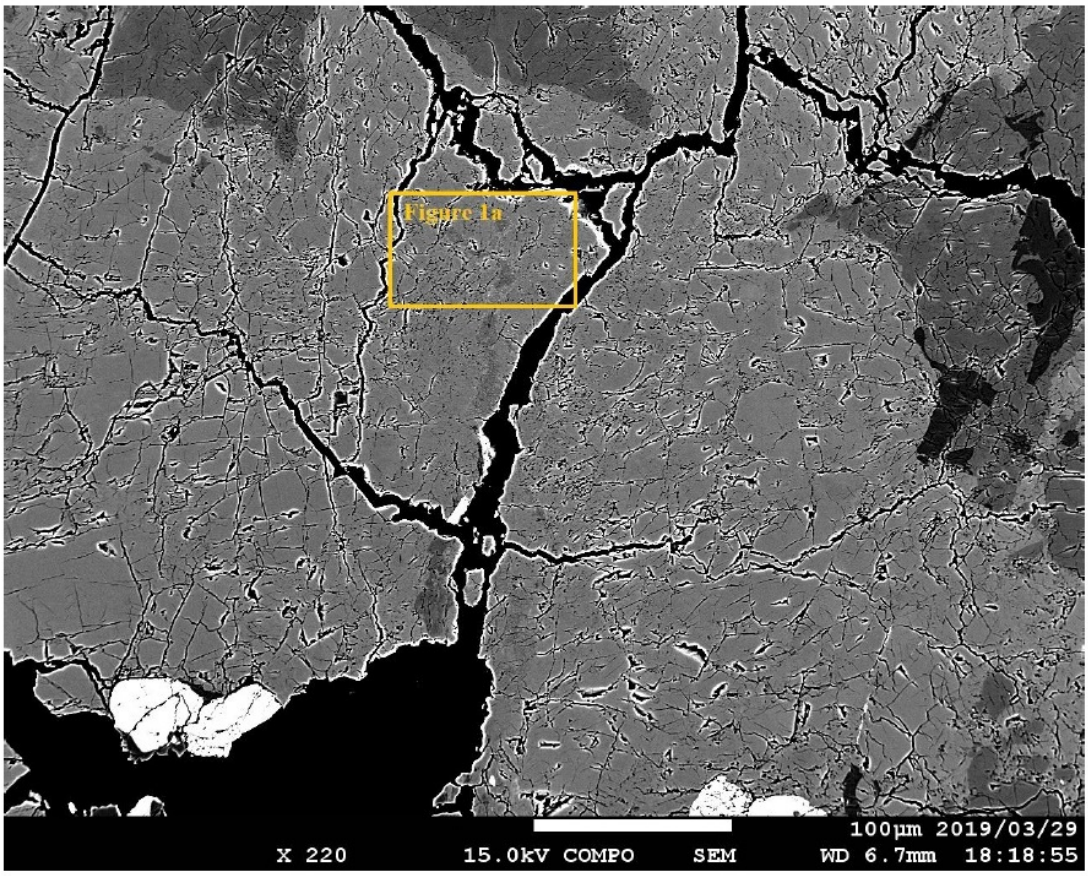

77

78 **Figure S1.** Low magnification BSE image representative of the basaltic domain of Apollo sample
79 15299. The mustard rectangle shows the location of the Figure 1a. Figure 1a contains the
80 investigated shock-melt pocket, and is reported in the main manuscript.

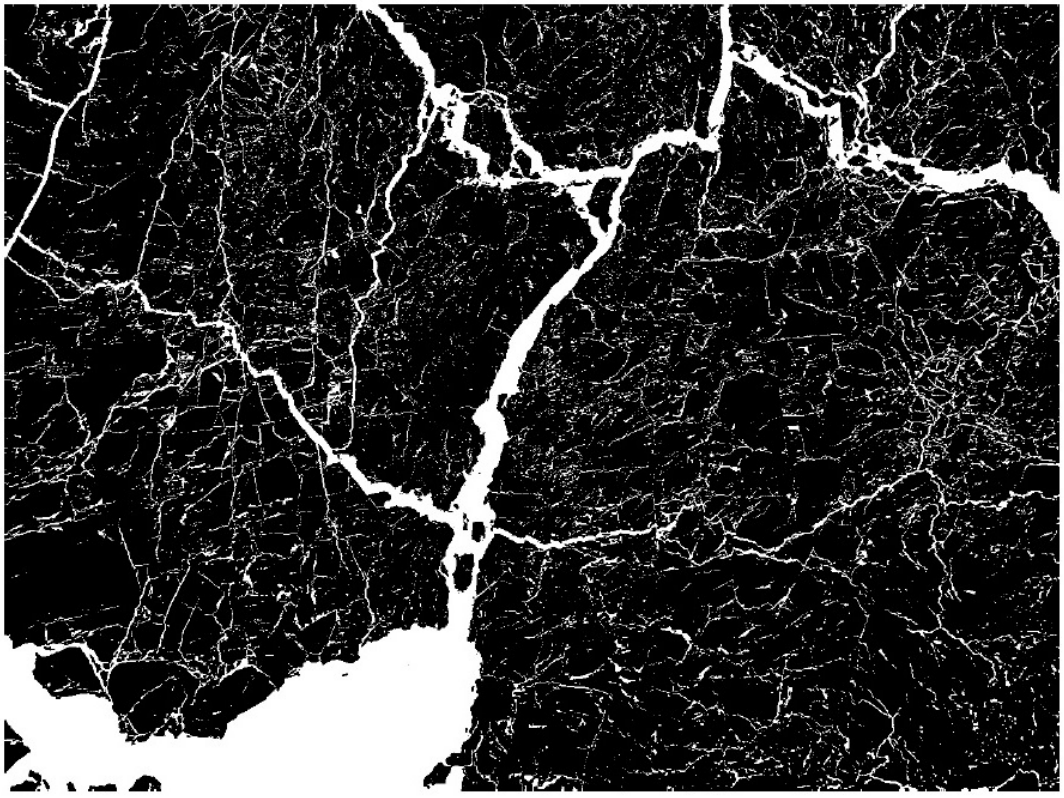

Figure S2. Processed image. The white areas represent the portions of the picture assigned to the fractures.

83 **SI References**

84 Smyth, J. R. (1975). High temperature crystal chemistry of fayalite1. *American Mineralogist*,
85 *60*(11–12), 1092–1097.
86 Smyth, J. R., & Hazen, R. M. (1973). The crystal structures of forsterite and hortonolite at
87 several temperatures up to 900°C. *American Mineralogist*, *58*(7–8), 588–593.

88

5 | Satta *et al.*, (2019). AM. (2019): 1526-1529

American Mineralogist, Volume 104, pages 1526–1529, 2019

LETTER

Single-crystal elasticity of iron-bearing phase E and seismic detection of water in Earth's upper mantle

NICCOLÒ SATTA[1,*], HAUKE MARQUARDT[2], ALEXANDER KURNOSOV[1], JOHANNES BUCHEN[3], TAKAAKI KAWAZOE[4], CATHERINE MCCAMMON[1], AND TIZIANA BOFFA BALLARAN[1]

[1]Bayerisches Geoinstitut, Universität Bayreuth, 95440 Bayreuth, Germany
[2]Department of Earth Sciences, University of Oxford, Oxford OX1 3AN, U.K.
[3]Seismological Laboratory, California Institute of Technology, Pasadena, California 91125, U.S.A.
[4]Department of Earth and Planetary Systems Science, Hiroshima University, Hiroshima 739-8526, Japan

ABSTRACT

The elastic properties of $Mg_{2.12(2)}Fe_{0.21(2)}Ni_{0.01}Si_{1.15(1)}O_6H_{2.67(8)}$ phase E single crystals with $Fe^{3+}/\Sigma Fe$ = 0.25(3) have been determined by Brillouin spectroscopy at ambient conditions. We find that that the elasticity of iron-bearing phase E is described by the six independent stiffness tensor components (all in units of GPa): C_{11} = 192.2(6), C_{12} = 56.4(8), C_{13} = 43.5(8), C_{14} = –4.3(3), C_{33} = 192.1(7), C_{44} = 46.4(3). The Voigt-Reuss-Hill averages of bulk and shear moduli are 95.9(4) and 59.6(2) GPa, respectively. The aggregate velocities of iron-bearing phase E are v_P = 7.60(2) and v_S = 4.43(1) km/s, markedly lower than those of major mantle minerals at ambient conditions. Modeling based on our results suggests that the presence of iron-bearing phase E may reduce the sound wave velocities in upper mantle and transition zone rocks, making it a possible target for future seismological investigations aiming to map hydration in subducting slabs.

Keywords: DHMS, phase E, Brillouin spectroscopy, elasticity

INTRODUCTION

Knowledge of the abundance and distribution of H_2O ("water") in the upper mantle is important for quantifying Earth's deep water cycle and improving our understanding of dynamic mantle processes, including deep earthquakes and magmatism (Schmidt and Poli 1998; Hacker et al. 2003). Subduction of oceanic lithosphere (slabs) is the main mechanism to transport water into Earth's interior. The alteration of oceanic lithosphere leads to the formation of OH-rich serpentine minerals at the expense of olivine and pyroxene. Upon subduction, water might be successively released as a free fluid at ~200 km depth after the breakdown of serpentine (Ulmer and Trommsdorff 1995). Along a cold geotherm typical of subducting slabs, however, water can be stored in dense hydrous magnesium silicate (DHMS) phases and transported to greater depths (e.g., Nishi et al. 2014). Phase E is a member of the DHMS group; it crystallizes in the $R\bar{3}m$ space group and is non-stoichiometric (Kudoh et al. 1993). The crystal structure of phase E is characterized by brucite-like sheets [(Mg,Fe)$(OH)_2$] of edge-sharing polyhedra that are stacked along the *c*-axis and connected by randomly occupied interlayer cation sites (Supplemental[1] Fig. S1). Commonly, Si^{4+} occupies the tetrahedrally coordinated cation sites (TO_4), while Mg^{2+} and Fe^{2+}/Fe^{3+} occupy the octahedrally coordinated sites (MO_6). All of these structural aspects lead to a very low density of phase E and allow up to ~18 wt% of water to be incorporated in the crystal structure (Crichton and Ross 2000). Since phase E has been found to be stable at temperatures up to 1200 °C at 13.5 GPa (Komabayashi et al. 2005), it could act as an important carrier of water into the deep mantle. Based on high-pressure X-ray diffraction (XRD) measurements, Shieh et al. (2000) reported a relatively low isothermal bulk modulus K_{0T} of 93(4) GPa for iron-free phase E that was later confirmed for an iron-bearing single crystal of phase E (Crichton and Ross 2000). The low bulk modulus of phase E could cause a detectable seismic signature in subducted slabs since it could lead to comparably low compressional wave velocities. However, no information on the shear modulus and the elastic anisotropy of phase E has been previously reported, hampering the interpretation of seismological observations. In this study, we conducted Brillouin scattering measurements on iron-bearing phase E single crystals at ambient conditions to quantify the compressional and shear wave velocities as well as the elastic anisotropy of phase E.

MATERIALS AND METHODS

San Carlos olivine powder was loaded into a platinum capsule together with distilled water. Phase E crystals were synthesized at 14 GPa and 1100 °C for 3 h in a multi-anvil apparatus at Bayerisches Geoinstitut (Germany). The chemical compositions of five grains were determined using an electron microprobe (JEOL JXA-8200) operated at a low beam current (5 nA) and with a defocused beam (10 μm in diameter) to minimize any possible damage to the samples. The average major element concentrations based on 139 analyzed points are 7.7(4) wt% FeO, 43.8(3) wt% MgO, 35.4(3) wt% SiO_2, and 0.3(1) wt% NiO. To determine the $Fe^{3+}/\Sigma Fe$ ratio by Mössbauer spectroscopy, five crystals were glued together on a plastic holder to form a wide circular mosaic aggregate with a diameter of 600 μm and a thickness of 400 μm. A Mössbauer spectrum (Supplemental[1] Fig. S2) was collected in transmission mode using a ^{57}Co point source. A least-square fitting procedure of Lorentzian functions implemented in the software MossA (Prescher et al. 2012) was used to fit the acquired spectrum. A model was employed using three quadrupole doublets. The center shifts (CS) of the doublets are located at 0.33(3) mm/s for CS_1, 1.08(1) mm/s for CS_2, and 1.10(2) mm/s for CS_3 when using a velocity scale calibrated using α-Fe (former National Bureau of Standards material no. 1541). The spectral components are interpreted to arise from both octahedrally coordinated ferric (CS_1) and ferrous

* E-mail: niccolo.satta@uni-bayreuth.de; Orcid 0000-0003-0397-6511
Open access: Article available to all readers online.

(CS_2, CS_3) iron. Based on the relative areas, a $Fe^{3+}/\Sigma Fe$ ratio of 0.25(3) has been determined. The resulting mineral formula of the studied phase E samples based on six oxygen atoms per formula unit (Kanzaki 1991) is $Mg_{2.12(2)}Fe^{2+}_{0.16(1)}Fe^{3+}_{0.05(1)}Ni_{0.01}Si_{1.15(1)}O_6H_{2.67(8)}$, where the H_2O content of 12.4(4) wt% has been estimated from the deviation of the sum of the analyzed oxides from 100%. Two optically clear single crystals were selected for Brillouin spectroscopy, oriented on a four-circle Eulerian cradle using XRD, and then double-side polished to a thickness of about 20 µm. Single-crystal XRD and Brillouin scattering measurements were conducted at ambient conditions using the combined system at the Bayerisches Geoinstitut (Trots et al. 2011; Kurnosov et al. 2017). Single-crystal diffraction experiments were performed employing a Mo$K\alpha$ X-ray flux generated by a rotating anode source operating at 50 kV and 40 mA. Diffracted X-rays were detected by a scintillation point detector. X-ray reflection profiles were recorded using the 8-position centering method (King and Finger 1979) and analyzed with the SINGLE software (Angel and Finger 2011) to correct for imperfect crystal centering. The refined unit-cell parameters obtained from a total of 15 centered reflections were a = 2.9748(6) Å, c = 13.8873(5) Å, v = 106.43(4) Å^3. A density of 3.04(1) g/cm^3 was calculated from the combination of the XRD results and the chemical analysis. Platelet normal vectors for crystal 1 and crystal 2 were found to be (0.84, –0.54, –0.01) and (0.11, –0.5, 0.86), respectively, in a Cartesian coordinate system where the Y-axis is parallel to the b*-axis and the Z-axis is parallel to the c-axis. Brillouin spectroscopy experiments were carried out using a solid-state Nd:YVO_4 laser source with a wavelength of λ = 532 nm. Brillouin frequency shifts were quantified using a six-pass Fabry-Perot interferometer (Lindsay et al. 1981) combined with an avalanche photodiode detector. All measurements were conducted using a symmetric forward scattering geometry (Whitfield et al. 1976; Speziale et al. 2014) with a measured external scattering angle (θ) of 80.8° calibrated using a silica reference glass. Experimentally determined frequency shifts (Δω) were converted to velocities (v) using the equation

$$v = \frac{\Delta\omega\lambda}{2\sin(\theta/2)}$$

where λ is the laser wavelength in air. We inverted experimentally measured sound wave velocities (v) together with crystallographic orientations and density to find the weighted nonlinear best fit to the Christoffel equation (Haussühl 2008) and to constrain all six independent components of the stiffness tensor (C_{ij}). Experimentally measured sound wave velocities as well as direction cosines and modeled velocities are given in Supplemental[1] Tables S1 and S2. We calculated the adiabatic bulk (K_S) and shear (G) moduli from the C_{ij} values using the Voigt-Reuss-Hill averaging procedure (Hill 1952; Watt et al. 1976).

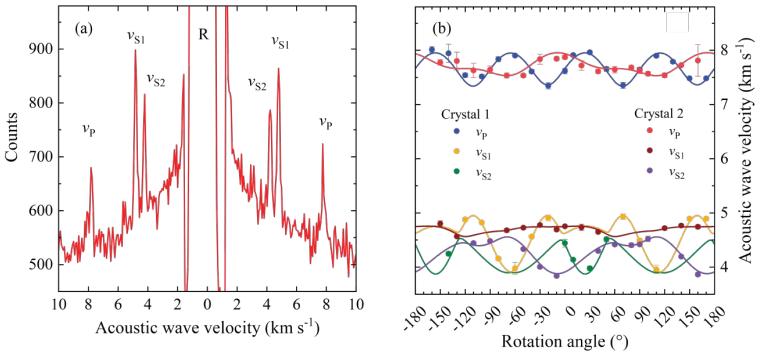

▲ **FIGURE 1.** (**a**) Representative Brillouin spectrum of iron-bearing phase E. Labeled peaks arise from inelastic anti-Stokes and Stokes scattering by quasi-longitudinal (v_P), quasi-transversal fast (v_{S1}), and quasi-transversal slow (v_{S2}) acoustic modes. The peak of elastically scattered light is marked with R. (**b**) Experimentally measured (filled circles) and calculated (solid curves) acoustic wave velocities as a function of the rotation angle. (Color online.)

TABLE 1. Components of the single-crystal stiffness tensor and Voigt and Reuss elastic moduli for a polycrystalline aggregate of phase E

C_{ij}	Value (GPa)	Parameters	Value (GPa)
C_{11}	192.2(6)	K_{Voigt}	95.9(3)
C_{33}	192.1(7)	G_{Voigt}	61.0(2)
C_{44}	46.4(3)	K_{Reuss}	95.8(4)
C_{12}	56.4(8)	G_{Reuss}	58.1(2)
C_{13}	43.5(8)	K_S	95.9(4)
C_{14}	–4.3(3)	G	59.6(2)

Notes: K_S and G were calculated using the Voigt-Reuss-Hill averaging scheme. Uncertainties on Hill averaged values have been calculated as the arithmetic mean between Voigt and Reuss bound uncertainties.

RESULTS AND DISCUSSION

A representative Brillouin spectrum of iron-bearing phase E is shown in Figure 1a. Figure 1b shows the observed angular dispersion of acoustic wave velocities for both crystals together with computed wave velocities using the Christoffel equation and the best-fit C_{ij} values. All measured velocity data are provided in Supplemental[1] Tables S1 and S2, while the best-fit elastic parameters are given in Table 1.

C_{11} and C_{33} show the same values within uncertainties, indicating that the stiffnesses along the a-axis and c-axis are similar. The elastic shear components C_{66} and C_{44} [where $C_{66} = (C_{11} - C_{12})/2$ and $C_{44} = C_{55}$] show different values, where C_{44} is ~30% smaller than C_{66}. The low value of C_{44} (and C_{55}) may be related to the low cation occupancies of the interlayer TO_4 and MO_6 polyhedra, which translate to a low resistance to shear stress in planes perpendicular to the structural layering. On the other hand, the edge-sharing polyhedra in the brucite-like sheets may be responsible for the relatively high value of C_{66}. Elastic wave velocities propagating in a phase E single crystal have been computed using the C_{ij} values as reported in Table 1 to investigate acoustic wave anisotropy (Supplemental[1] Fig. S3). The shear wave polarization anisotropy (in percentage), $A_{vs} = 200(v_{S1} - v_{S2})/(v_{S1} + v_{S2})$, reaches its maximum of ~20% along [100] in the basal plane. The fastest compressional waves propagate in the basal plane with a velocity of 7.96 km/s (v_{Pmax}) while the slowest wave propagates with 7.25 km/s (v_{Pmin}) along [0.61, 0.35, 0.71], i.e., in a direction between the basal plane and the c-axis. The maximum longitudinal anisotropy (in percentage) is ~9%, calculated as $A_{vp} = 200 \times (v_{Pmax} - v_{Pmin})/(v_{Pmax} + v_{Pmin})$.

IMPLICATIONS

Based on our single-crystal measurements on phase E, we derived aggregate compressional and shear sound wave velocities of v_P = 7.60(2) and v_S = 4.43(1) km/s at ambient conditions. These velocities are significantly lower than the sound wave velocities of other mantle minerals that are predicted to be stable along with phase E in upper mantle and transition zone rocks. A comparison among selected minerals is given in Supplemental[1] Table S3.

To estimate the effect of iron-bearing phase E on seismic velocities in subducted rocks, we used the data summarized in Supplemental[1] Table S3 to calculate isotropic aggregate velocities at ambient conditions for three different phase assemblages (phase E-bearing, hydrous, and dry). We calculated the elastic moduli of these

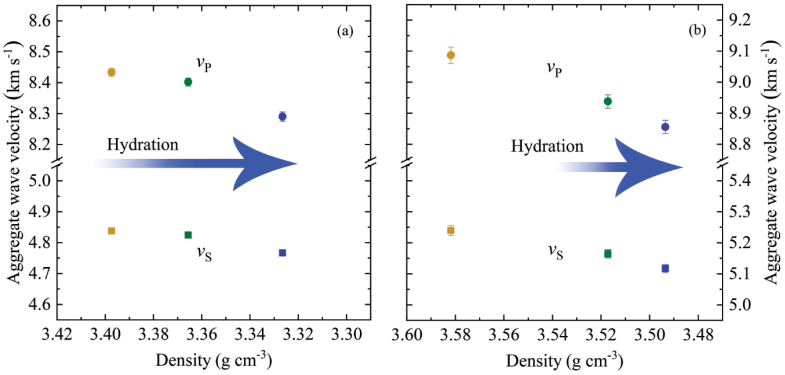

►**Figure 2.** Aggregate wave velocities of dry, hydrous, and phase E-bearing upper mantle (**a**) and transition zone (**b**) peridotites at ambient conditions as a function of density. Circles and squares refer to v_P and v_S, respectively. Dry, hydrous, and phase E-bearing assemblage velocities are in yellow, green, and blue colors, respectively.

assemblages using the arithmetic mean (Hill-average) of their Voigt M_V and Reuss M_R bounds, described as:

$$M_V = \sum_{i=1}^{N} M_i f_i \text{ and } 1/M_R = \sum_{i=1}^{N} f_i / M_i.$$

Here, N is the number of different mineral phases in the assemblage and f_i and M_i are the volume fractions and elastic moduli of the i-th constituent (Avseth et al. 2010), respectively. The modeled assemblages represent various stages of hydration of a cold slab of a peridotitic composition and are expected to form at conditions of the shallow transition zone (TZ) and the lowermost upper mantle (UM) just above the 410 km seismic discontinuity. The compositions of both the TZ and UM phase E-bearing assemblages are based on those given by Ohtani et al. (2004). Phase volume fractions of the employed TZ and UM assemblages as well as their acoustic velocities are listed in Supplemental[1] Table S4.

To compare velocities in hydrous (no phase E) and dry assemblages, we fixed the mineral volume fractions in dry and hydrous assemblages and only changed the hydration state of wadsleyite or olivine. For hydrous, phase E-bearing assemblages, we assume phase E to form at the expense of either hydrous wadsleyite or olivine. This is consistent with previous findings that water-saturated conditions are likely required for phase E formation in the presence of wadsleyite (Frost 1999). Furthermore, we assumed that the Mg/Fe ratio in both wadsleyite and olivine does not change once phase E is formed.

Our modeling shows that hydration and the presence of phase E in isotropic aggregates substantially reduce propagation velocities of both compressional and shear waves at ambient conditions (Fig. 2). For example, the here-considered UM phase E-bearing assemblage exhibits a reduction of 2% and 1.8% for

$$v_P = \sqrt{\frac{K_S + \frac{4}{3}G}{\rho}} \text{ and } v_S = \sqrt{\frac{G}{\rho}}$$

with respect to the dry UM assemblage (Fig. 2a). Comparison among different UM assemblages shows that hydration of olivine reduces v_P and v_S values of a dry UM assemblage by only about 0.5 and 0.3%, respectively, showing that phase E is the primary source of seismic wave speed reductions in our models. Similarly, the modeled TZ phase E-bearing assemblage is characterized by 2.5 and 2.4% slower velocities for isotropic v_P and v_S compared to the dry TZ assemblage (Fig. 2b). It has been shown experimentally that the effect of hydration on the sound wave velocities of olivine, wadsleyite, and ringwoodite significantly decreases with pressure, possibly making hydration of wadsleyite and ringwoodite invisible to seismology (Mao et al. 2010; Buchen et al. 2018; Schulze et al. 2018). The presence of phase E-bearing assemblages in cold subducting slabs, instead, might lead to a seismologically detectable reduction of seismic wave velocities, unless phase E exhibits a strong velocity increase with pressure. To evaluate the effect of pressure on phase E elasticity, we combined the here-derived ambient-pressure elastic moduli with previously published high-pressure XRD data. Previous compression studies reported different pressure derivatives of the bulk modulus (K_0') of 7.3(2) (Crichton and Ross 2000) and 5(1) (Shieh et al. 2000). We re-evaluated the previous data sets independently by fitting the reported high-pressure unit-cell volumes to a third-order Birch Murnaghan equation of state using EoSFit7c (Angel et al. 2014). Our re-evaluation of the previous XRD data (Supplemental[1] Fig. S4) shows that both previous works are consistent with $K_0' \sim 7$. Angel et al. (2001) argued that polyhedral edge-sharing, which is characteristic of DHMS phase crystal structures, controls their compression mechanism. According to the authors, the crystal structures of DHMS phases can accommodate compression by shortening of cation-oxygen bonds and/or through a deformation of the polyhedra. Among the DHMS, phase A has a density most similar to phase E and comparably low bulk and shear moduli, $K_S = 106(1)$ GPa; $G = 61$ GPa (Sanchez-Valle et al. 2006, 2008). Other DHMS phases such as superhydrous phase B (Rosa et al. 2015) and phase D (Rosa et al. 2013) have more dense-packed structures and both their elastic moduli and pressure derivatives differ substantially from those of phase E. Therefore, we assume that the shear modulus of phase E shows a similar response to compression as the one of phase A. Consequently, we used the pressure derivative of the shear modulus of iron-bearing phase A, $G' = 1.8$ (Sanchez-Valle et al. 2008) together with a K_0' of 7.1, consistent with the re-evaluated compression studies of Crichton and Ross (2000) and Shieh et al. (2000) on phase E, to compute sound wave velocities of phase E at mantle pressures. We found that at 13 GPa and 300 K, phase E will have compressional and shear wave velocities of 7.33 and 4.88 km/s, respectively, which are about 8% and 16% lower compared to hydrous wadsleyite at the same pressure (Mao et al. 2011). Phase E might, therefore, be

a better indicator to map hydration in the shallow transition zone using seismology than the volumetrically dominant mineral wadsleyite. Future high-pressure and high-temperature experimental investigations on the elastic properties of phase E, including its high-pressure shear modulus, are needed to precisely determine how varying abundances of phase E in both randomly distributed and textured aggregates may affect the propagation of seismic waves in hydrous subducted slabs.

Acknowledgments and Funding

We thank R. Njul for polishing the crystal platelets. This research was supported through the project "GeoMaX" funded under the Emmy-Noether Program of the German Science Foundation DFG (MA4534/3-1) as well as the International Research Training Group "Deep Earth Volatile Cycles" (GRK 2156/1). H. Marquardt acknowledges support from the Bavarian Academy of Sciences. N. Satta thanks S. Speziale for his suggestions on Brillouin scattering measurements.

References cited

Angel, R.J., and Finger, L.W. (2011) SINGLE: a program to control single-crystal diffractometers. Journal of Applied Crystallography, 44(1), 247–251.

Angel, R.J., Frost, D.J., Ross, N.L., and Hemley, R. (2001) Stabilities and equations of state of dense hydrous magnesium silicates. Physics of the Earth and Planetary Interiors, 127(1-4), 181–196.

Angel, R.J., Alvaro, M., and Gonzalez-Platas, J. (2014) EosFit7c and a Fortran module (library) for equation of state calculations. Zeitschrift für Kristallographie—Crystalline Materials, 229(5), 405–419.

Avseth, P., Mukerji, T., and Mavko, G. (2010) Quantitative Seismic Interpretation: Applying Rock Physics Tools to Reduce Interpretation Risk. Cambridge.

Buchen, J., Marquardt, H., Speziale, S., Kawazoe, T., Boffa-Ballaran, T., Kurnosov, A. (2018) High-pressure single-crystal elasticity of wadsleyite and the seismic signature of water in the shallow transition zone. Earth and Planetary Science Letters, 498, 77–87.

Collins, M.D., and Brown, J.M. (1998) Elasticity of an upper mantle clinopyroxene. Physics and Chemistry of Minerals, 26, 7–13.

Crichton, W.A., and Ross, N.L. (2000) Equation of state of phase E. Mineralogical Magazine, 424, 561–567.

Frost, D.J. (1999) The stability of dense hydrous magnesium silicates in Earth's transition zone and lower mantle. In Y. Fei, C.M. Bertka, and B.O. Mysen, Eds., Mantle Petrology: Field Observations and High Pressure Experimentation: A Tribute to Francis R. (Joe) Boyd. The Geochemical Society, Special Publication No.6.

Hacker, B.R., Peacock, S.M., Abers, G.A., and Holloway, S.D. (2003) Subduction factory 2. Are intermediate-depth earthquakes in subducting slabs linked to metamorphic dehydration reactions? Journal of Geophysical Research: Solid Earth, 108(B1).

Haussühl, S. (2007) Physical Properties of Crystals: An Introduction. Wiley.

Hill, R. (1952) The elastic behavior of a crystalline aggregate. Proceedings of the Physical Society A, 65, 349–354.

Jacobsen, S.D., F. Jiang, Z. Mao, T.S. Duffy, J.R. Smyth, C.M. Holl, and Frost, D.J. (2009) Correction to ''Effects of hydration on the elastic properties of olivine". Geophysical Research Letters, 36, L12302, doi:10.1029/2009GL038660.

Kanzaki, M. (1991) Stability of hydrous magnesium silicates in the mantle transition zone. Physics of the Earth and Planetary Interiors, 66(3-4), 307–312.

King, H.E., and Finger, L.W. (1979) Diffracted beam crystal centering and its application to high-pressure crystallography. Journal of Applied Crystallography, 12(4), 374–378.

Komabayashi, T., Omori, S., and Maruyama, S. (2005) Experimental and theoretical study of stability of dense hydrous magnesium silicates in the deep upper mantle. Physics of the Earth and Planetary Interiors, 153(4), 191–209.

Kudoh, Y., Finger, L.W., Hazen, R.M., Prewitt, C.T., Kanzaki, M., and Veblen, D.R. (1993) Phase E: A high pressure hydrous silicate with unique crystal chemistry. Physics and Chemistry of Minerals, 19(6), 357–360.

Kurnosov, A., Marquardt, H., Frost, D.J., Boffa Ballaran, T., and Ziberna, L. (2017) Evidence for a Fe^{3+}-rich pyrolitic lower mantle from (Al,Fe)-bearing bridgmanite elasticity data. Nature, 543(7646), 543.

Lindsay, S.M., Anderson, M.W., and Sandercock, J.R. (1981) Construction and alignment of a high performance multipass vernier tandem Fabry-Perot interferometer. Review of Scientific Instruments, 52(10), 1478–1486.

Mao, Z., Jacobsen, S.D., Jiang, F., Smyth, J.R., Holl, C.M., Frost, D.J., and Duffy, T.S. (2010) Velocity crossover between hydrous and anhydrous forsterite at high pressures. Earth and Planetary Science Letter, 293, 250–258.

Mao, Z., Jacobsen, S.D., Frost, D.J., McCammon, C.A., Hauri, E.H., and Duffy, T.S. (2011) Effect of hydration on the single-crystal elasticity of Fe-bearing wadsleyite to 12 GPa. American Mineralogist, 96(10), 1606–1612.

Nishi, M., Irifune, T., Tsuchiya, J., Tange, Y., Nishihara, Y., Fujino, K., and Higo, Y. (2014) Stability of hydrous silicate at high pressures and water transport to the deep lower mantle. Nature Geoscience, 7(3), 224.

Ohtani, E., Litasov, K., Hosoya, T., Kubo, T., and Kondo, T. (2004) Water transport into the deep mantle and formation of a hydrous transition zone. Physics of the Earth and Planetary Interiors, 143, 255–269.

Pamato, M.G., Kurnosov, A., Boffa Ballaran, T., Frost, D.J., Ziberna, L., Giannini, M., Speziale, S., Tkachev, S.N., Zhuravlev, K.K., and Prakapenka, V.B. (2016) Single crystal elasticity of majoritic garnets: Stagnant slabs and thermal anomalies at the base of the transition zone. Earth and Planetary Science Letters, 451, 114–124.

Prescher, C., McCammon, C., and Dubrovinsky, L. (2012) MossA: a program for analyzing energy-domain Mössbauer spectra from conventional and synchrotron sources. Journal of Applied Crystallography, 45(2), 329–331.

Rosa, A.D., Mezouar, M., Garbarino, G., Bouvier, P., Ghosh, S., Rohrbach, A., and Sanchez-Valle, C. (2013) Single-crystal equation of state of phase D to lower mantle pressures and the effect of hydration on the buoyancy of deep subducted slabs. Journal of Geophysical Research: Solid Earth, 118(12), 6124–6133.

Rosa, A.D., Sanchez-Valle, C., Wang, J., and Saikia, A. (2015) Elasticity of superhydrous phase B, seismic anomalies in cold slabs and implications for deep water transport. Physics of the Earth and Planetary Interiors, 243, 30–43.

Sanchez-Valle, C., Sinogeikin, S.V., Smyth, J.R., and Bass, J.D. (2006) Single-crystal elastic properties of dense hydrous magnesium silicate phase A. American Mineralogist, 91, 961–964.

Sanchez-Valle, C., Sinogeikin, S.V., Smyth, J.R., and Bass, J.D. (2008) Sound velocities and elasticity of DHMS phase A to high pressure and implications for seismic velocities and anisotropy in subducted slabs. Physics of the Earth and Planetary Interiors, 170(3-4), 229–239.

Schmidt, M.W., and Poli, S. (1998) Experimentally based water budgets for dehydrating slabs and consequences for arc magma generation. Earth and Planetary Science Letters, 163(1-4), 361–379.

Schulze, K., Marquardt, H., Kawazoe, T., Boffa Ballaran, T., McCammon, C., Koch-Müller, M., Kurnosov, A., and Marquardt, K. (2018) Seismically invisible water in Earth's transition zone? Earth and Planetary Science Letters, 498, 9–16.

Shieh, S.R., Mao, H.K., Konzett, J., and Hemley, R.J. (2000) In-situ high pressure X-ray diffraction of phase E to 15 GPa. American Mineralogist, 85, 765–769.

Speziale, S., Marquardt, H., and Duffy, T.S. (2014) Brillouin scattering and its application in geosciences. Spectroscopic Methods in Mineralogy and Materials Sciences, 78, 543–603.

Trots, D.M., Kurnosov, A., Vasylechko, L., Berkowski, M., Boffa Ballaran, T., and Frost, D.J. (2011) Elasticity and equation of state of $Li_2B_4O_7$. Physics and Chemistry of Minerals, 38(7), 561.

Ulmer, P., and Trommsdorff, V. (1995) Serpentine stability to mantle depths and subduction-related magmatism. Science, 268, 858–861.

Watt, J.P., Davies, G.F., and O'Connell, R.J. (1976) The elastic properties of composite materials. Reviews of Geophysics, 14(4), 541–563.

Webb, S.L. (1989) The elasticity of the upper mantle orthosilicates olivine and garnet to 3 GPa. Physics and Chemistry of Minerals, 16(7), 684–692.

Whitfield, C.H., Brody, E.M., and Bassett, W.A. (1976) Elastic moduli of NaCl by Brillouin scattering at high pressure in a diamond anvil cell. Review of Scientific Instruments, 47(8), 942–947.

Manuscript received April 19, 2019
Manuscript accepted July 8, 2019
Manuscript handled by Ian Swainson

Endnote:

[1]Deposit item AM-19-107084, Supplemental Material. Deposit items are free to all readers and found on the MSA website, via the specific issue's Table of Contents (go to http://www.minsocam.org/MSA/AmMin/TOC/2019/Oct2019_data/Oct2019_data.html).

5.1 Supplementary Material

CRYSTAL 1									
Rotation angle (°)	**Photon direction cosines**			**V_P (km s^{-1})**		**V_{S1} (km s^{-1})**		**V_{S2} (km s^{-1})**	
χ_0 = -155.4	X	Y	Z	Observed	Model	Observed	Model	Observed	Model
0	-0.48	-0.77	0.42	7.62(5)	7.67	-	4.62	4.44(7)	4.42
-20	-0.37	-0.61	0.70	7.35(6)	7.37	4.91(5)	4.95	-	4.32
-40	-0.22	-0.37	0.90	7.61(4)	7.63	4.56(3)	4.53	-	4.04
-60	-0.04	-0.09	1.00	7.90(3)	7.93	3.98(10)	3.96	-	3.89
-80	0.15	0.21	0.97	7.84(4)	7.84	4.16(4)	4.15	-	3.95
-100	0.31	0.47	0.82	7.52(3)	7.44	4.82(3)	4.80	-	4.19
-120	0.44	0.68	0.58	7.54(4)	7.42	4.88(4)	4.83	-	4.48
-140	0.52	0.81	0.27	7.95(17)	7.81	-	4.71	4.25(4)	4.13
-160	0.53	0.84	-0.08	8.01(6)	7.94	-	4.75	-	3.89
10	-0.52	-0.82	0.25	7.91(3)	7.85	-	4.70	4.14(2)	4.10
30	-0.53	-0.84	-0.10	7.96(2)	7.93	-	4.75	3.98(4)	3.91
50	-0.49	-0.76	-0.43	7.66(4)	7.62	-	4.75	4.52(4)	3.91
70	-0.38	-0.59	-0.71	7.35(6)	7.34	4.93(5)	4.95	-	4.35
90	-0.23	-0.35	-0.91	7.64(3)	7.64	4.49(3)	4.48	-	4.06
110	-0.05	-0.06	-1.00	7.90(3)	7.94	3.96(8)	3.95	-	3.90
130	0.13	0.23	-0.96	7.79(3)	7.82	-	4.19	-	3.94
150	0.30	0.50	-0.82	7.48(2)	7.44	4.89(3)	4.84	-	4.17
170	0.44	0.70	-0.57	7.47(2)	7.46	4.89(3)	4.79	-	4.45

Supplementary Table 1.

CRYSTAL 2									
Rotation angle (°)	**Photon direction cosines**			**V_P (km s^{-1})**		**V_{S1} (km s^{-1})**		**V_{S2} (km s^{-1})**	
χ_0 = -6.1	X	Y	Z	Observed	Model	Observed	Model	Observed	Model
0	0.96	0.29	0.05	7.87(3)	7.94	4.75(2)	4.75	-	3.91
-20	0.80	0.55	0.22	7.72(9)	7.80	4.73(6)	4.76	-	4.13
-40	0.55	0.75	0.37	7.61(4)	7.69	4.65(3)	4.69	4.30(3)	4.35
-60	0.24	0.85	0.47	7.64(6)	7.67	-	4.56	4.42(3)	4.45
-80	-0.11	0.85	0.51	7.68(4)	7.64	-	4.62	4.40(4)	4.40
-100	-0.28	0.82	0.51	7.63(6)	7.59	-	4.65	4.42(2)	4.44
-120	-0.44	0.75	0.49	7.57(4)	7.55	-	4.66	4.52(5)	4.51
-140	-0.72	0.56	0.41	7.54(4)	7.56	4.72(3)	4.71	-	4.51
-160	-0.91	0.30	0.29	7.72(3)	7.75	4.77(2)	4.74	4.19(3)	4.23
10	-0.99	0.00	0.12	7.81(29)	7.92	4.74(4)	4.74	3.86(3)	3.93
30	0.99	0.15	-0.04	7.84(3)	7.96	4.69(3)	4.75	3.84(2)	3.88
50	0.97	-0.15	-0.21	7.84(9)	7.85	4.78(2)	4.74	4.00(3)	4.06
70	0.83	-0.44	-0.35	7.54(3)	7.63	4.73(2)	4.73	4.33(2)	4.39
90	0.59	-0.67	-0.46	7.53(4)	7.53	4.68(3)	4.68	-	4.56
110	0.28	-0.82	-0.51	7.64(7)	7.59	-	4.65	4.48(3)	4.44
130	-0.06	-0.87	-0.50	7.63(13)	7.66	-	4.59	4.44(3)	4.41
150	-0.40	-0.81	-0.42	7.80(16)	7.67	4.56(2)	4.61	-	4.42
170	-0.69	-0.66	-0.30	7.78(5)	7.73	4.80(5)	4.73	-	4.25

Supplementary Table 2

Mineral phases	H_2O (wt%)	ρ (g cm^{-3})	K_S (GPa)	G (GPa)	V_P (km s^{-1})	V_S (km s^{-1})
Iron-bearing phase E*	12.4(4)	3.04(1)	95.9(4)	59.6(2)	7.60(2)	4.43(1)
Fo90[a]	0	3.350	129.5	77.5	8.34	4.81
Hydrous Fo90[b]	0.89	3.303	126	75.8	8.29	4.79
Mg89 wadsleyite[c]	0	3.610(1)	169.6(9)	105.2(5)	9.26(2)	5.40(2)
Hydrous Mg89 wadsleyite[d]	1.93(22)	3.513(7)	156.2(5)	98.0(3)	9.04(1)	5.28(1)
Majorite[e]	0	3.601(3)	173(3)	92(1)	9.06(5)	5.05(3)
Peridotitic clinopyroxene[f]	0	3.327(3)	117.2(7)	72.2(2)	8.01(1)	4.66(1)

Supplementary Table 3. Water content, density, isotropic aggregate elastic moduli and acoustic wave velocities for upper mantle and transition zone phases at ambient conditions, as used for the modelling. *Our study; [a] Webb (1989); [b]ρ, K_S and G calculated following the Hy-Fo100 water dependence in Jacobsen et al. (2009); [c]Linear extrapolation to anhydrous composition of ρ(H20), K_S(ρ) and G(ρ) using Mg89H2 from Buchen et al. (2018) and Mg89H15 Mao et al. (2011) data; [d]Mao et al. (2011); [e]Py78Alm6Mj16 in Pamato et al. (2016); [f]Collins and Brown (1998).

	Upper Mantle Assemblage			Transition Zone Assemblage		
Mineral phases	**Phase E-bearing**	**Hydrous**	**Dry**	**Phase E-bearing**	**Hydrous**	**Dry**
Iron-bearing phase E (vol%)	14.8			5		
Fo90 (vol%)			67.8			
Hydrous Fo90 (vol%)	53	67.8				
Mg89 wadsleyite (vol%)						66.6
Hydrous Mg89 wadsleyite (vol%)				61.6	66.6	
Majorite (vol%)	20	20	20	24.2	24.2	24.2
Peridotitic clinopyroxene (vol%)	12.2	12.2	12.2	9.2	9.2	9.2
Assemblage velocities						
V_P (km s^{-1})	8.29(2)	8.40(1)	8.43(1)	8.86(2)	8.94(2)	9.09(3)
V_S (km s^{-1})	4.77(1)	4.82(1)	4.84(1)	5.12(1)	5.16(1)	5.24(2)

Supplementary Table 4. Phase volume fractions used for the modelling, based on Ohtani et al. (2004), and isotropic aggregate velocities of upper mantle and transition zone assemblages calculated at ambient conditions.

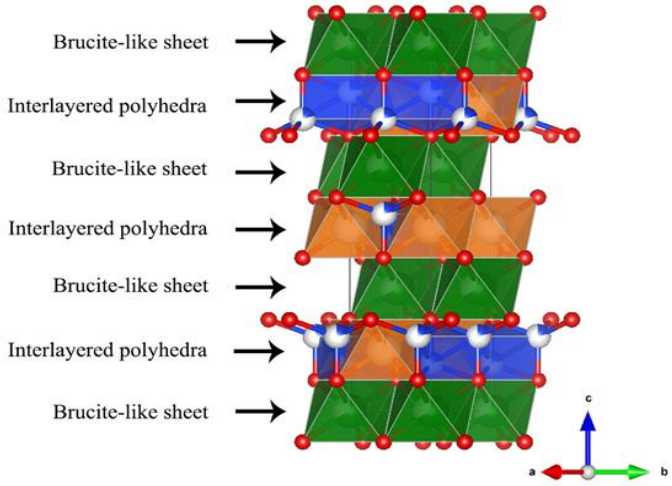

Supplementary Figure 1. Phase E crystal structure. Brucite-like sheets $[(Mg,Fe)(OH)_2]$ in green. Interlayered TO_4 and MO_6 polyhedra in blue and orange, respectively. Oxigens in red. Spheres in the center of polyhedra represent polyhedra occupancy.

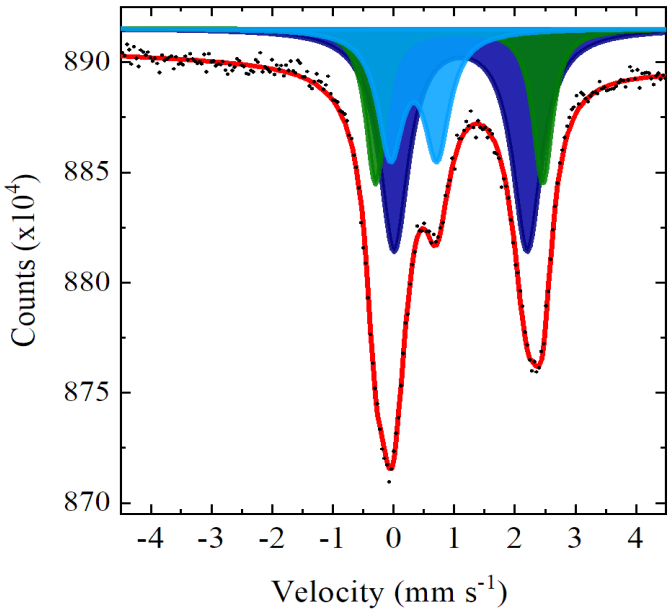

Supplementary Figure 2. Mössbauer spectrum of phase E. Areas of CS_1, CS_2 and CS_3 are presented as light blue, green and dark blue respectively.

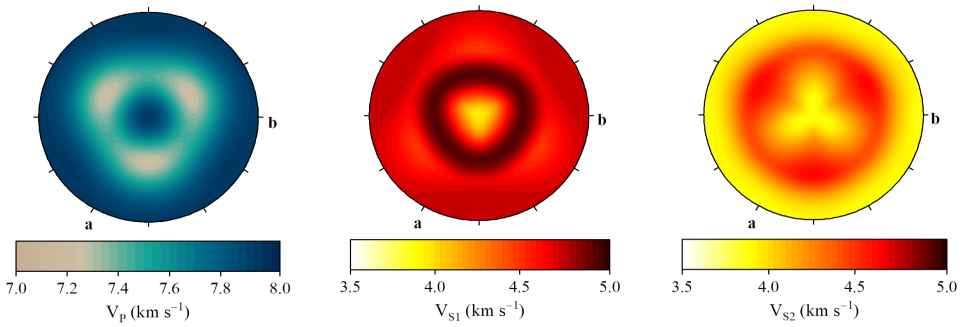

Supplementary Figure 3. Stereographic projections of acoustic wave velocities in phase E, at ambient conditions. The c-axis is perpendicular to the projection. Other lattice axes are marked.

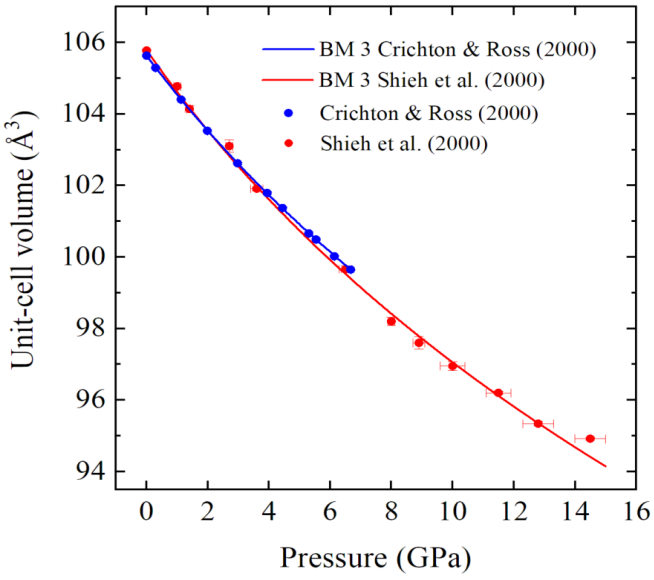

Supplementary Figure 4. Variation of phase E unit-cell volume with pressure using Shieh et al. (2000) and Crichton & Ross (2000) data, in red and blue, respectively. Dots represent measured points, solid lines represent data fitted to a third-ordered Birch-Murnagham equation of state.

6 | Satta *et al.*, Manuscript Draft

Manuscript Draft

Elastic Softening Driven by Hydrogen Disorder in δ-(Al,Fe)OOH

Niccolò Satta[1], Giacomo Criniti[1], Alexander Kurnosov[1], Tiziana Boffa Ballaran[1], Takayuki Ishii[1] and Hauke Marquardt[2]

[1]Bayerisches Geoinstitut, Universität Bayreuth, D-95440 Bayreuth, Germany

[2]Department of Earth Sciences, University of Oxford, Oxford OX1 3AN, United Kingdom

Abstract

Simultaneous single-crystal high-pressure X-ray diffraction and Brillouin spectroscopy measurements have been performed on an Fe-bearing δ-AlOOH sample containing ~3% of Fe^{3+} in order to constrain the elastic behaviour of this oxy-hydroxide compound through the $P2_1nm$ to $Pnnm$ phase transition. This transformation occurs between 7.59(3) GPa and 7.94(2) GPa. The compression behaviour of the $P2_1nm$ phase shows a large anisotropy in the axial compressibility which follows the scheme: $\beta_b > \beta_a > \beta_c$. However, after the transition to the $Pnnm$ structure, the b-axis becomes the least compressible. The isothermal bulk modulus, K_{T0}, and its first pressure derivative, K'_{T0}, have been accurately determined for the $P2_1nm$ phase by fitting the measured P-V data using a 3rd-order Birch-Murnaghan equation of state. The resulting values K_{T0} = 149.9(11) GPa and K'_{T0} = 3.7(4) are identical to those reported for the δ-AlOOH end-member and significantly smaller than the values reported in theoretical studies. The full elastic tensor obtained at 7 different high-pressure points reveals softening of three elastic components, namely C_{22}, C_{12} and C_{23} above 6.5 GPa with consequent softening of the adiabatic bulk modulus and of the aggregate longitudinal wave velocity. This softening is associated with the change in hydrogen bond character which is localized in the $P2_1nm$ structure but has a disorder configuration of the

hydrogen atoms in the *Pnnm* structure. Similar changes in the hydrogen bond character are expected in other hydroxide minerals with increasing pressure due to changes in the O-H···O distance during compression. This suggests that softening may be a common precursor of hydrogen bond symmetrisation.

Key Words: High-pressure, phase transition, X-ray diffraction, δ-AlOOH

Introduction

The subduction of oceanic crust and pelagic sediments is responsible for carrying a significant amount of water into the Earth's mantle (Peacock 1990). As hydrous minerals dehydrate with increasing depth, water is released and migrates into the overlying mantle causing metasomatism and influencing melting processes. Some of this water, however, likely remains in the subducting lithosphere and is either incorporated in nominally anhydrous minerals (Bell and Rossman 1992) or in dense hydrous silicates (Ohtani 2015) as suggested by mineral inclusions in diamonds (Wirth et al. 2007; Pearson et al. 2014).

Phase equilibria studies performed at subduction zone conditions have indicated that a chain of hydrous phases involving phengite, topaz, $AlSiO_3(OH)$ phase egg and ending in δ-phase AlOOH could transport water within hydrated natural sediment compositions into the lower mantle (Ono 1998; Sano et al. 2004). Due to the much lower water storage capacity of ultramafic lower mantle compositions (Bolfan-Casanova 2005; Nishi et al. 2014; Ohtani 2015) water that is subducted into the lower mantle may also be forced to migrate into subducted sediment lithologies. In addition, the basaltic crust can contributite (Liu et al. 2019; Nishi et al. 2019). Furthermore δ-phase AlOOH

is one of the only hydrous phases that is stable along a lower mantle geotherm and has the highest thermal stability at these conditions of any known hydroxide (Ohira et al. 2014).

Dense aluminum and iron oxy-hydroxide (δ-AlOOH and ε-FeOOH) may, therefore, be an important hydrogen host in the deep mantle particularly due to their stability over a wide pressure and temperature range (Ohtani et al. 2001; Sano et al. 2004; Sano-Furukawa et al. 2008; Nishi et al. 2017). Solid solution among the two oxy-hydroxide has been found above 18 GPa and appears to cover a large compositional range (Kawazoe et al. 2017; Nishi et al. 2017; Xu et al. 2019). Both compounds have a $CaCl_2$-type structure with space group $P2_1nm$ (Komatsu et al. 2006; Bolotina et al. 2008; Suzuki 2010; Kuribayashi et al. 2014) consisting of columns parallel to the *c*-axis of edge-sharing octahedra. The columns are connected to each other via shared corners. The octahedral cation site is coordinated by 5 oxygens and one hydroxide, which gives rise to a strong hydrogen bond on the *a*-*b* plane (Figure 1a). Both phases undergo a phase transformation from the low-symmetry $P2_1nm$ space group to the high-symmetry *Pnnm* space group. For δ-AlOOH a general consent among theoretical and experimental studies (Cortona 2017; Pillai et al. 2018; Sano-Furukawa et al. 2018) has been reached, reporting a hydrogen bond symmetrisation pressure between 15 and 18 GPa. However, the $P2_1nm$ to *Pnnm* phase transition occurs at much lower pressures, between 8–10 GPa (Sano-Furukawa et al. 2009; Kuribayashi et al. 2014) and it is associated with a large change in axial compressibility. The transition appears to be driven not by symmetrisation but by the disorder of the hydrogen between two equivalent sites across the centre of the O···O distance where the two oxygens are one the proton donor and the other the acceptor in the hydrogen bond (Sano-Furukawa et al. 2018). In the *Pnnm* H-disordered structure as defined by Sano-Furukawa et al. (2018)(Figure 1b), the hydrogen potential consists of a two-wells and it is induced by the change in the O···O distance due to compression. The hydrogen is expected to be

71 delocalised in the two wells owning to thermal effects (Benoit and Marx 2005). A further
72 compression drives the oxygens even closer and the hydrogen potential becomes a single-well at
73 the centre of the O···O distance (Figure 1c). The effect of these changes on elastic properties are
74 debated. The completion of symmetrisation appears to have little effect on the compressibility of
75 the *Pnnm* structure according to existing *P-V* experimental data (e.g., Sano-Furukawa et al. 2009).
76 In contrast, theoretical studies predicts changes in slopes or even large discontinuities in some of
77 the elastic tensor components at the onset of symmetrisation (Tsuchiya and Tsuchiya 2009;
78 Cortona 2017; Pillai et al. 2018). A drastic change has been instead observed above 15 GPa in the
79 acoustic wave velocities measured by means of Brillouin spectroscopy on a powdered sample of
80 δ-AlOOH (Mashino et al. 2016) likely due to the hydrogen bond symmetrization. However, in this
81 previous Brillouin study no effect attributable to the effect $P2_1nm$ to *Pnnm* phase transition on the
82 measured velocities, in agreement with the smooth change of the elastic stiffness component up to
83 symmetrisation reported by theoretical studies (Tsuchiya and Tsuchiya 2009; Cortona 2017; Pillai
84 et al. 2018). At the other end of the solid solution, hydrogen bond symmetrisation in ε-FeOOH has
85 been so far predicted only by first principle calculations at about 43 GPa (Gleason et al. 2013) and
86 between 10 and 20 GPa (Thompson et al. 2017). Thompson et al. (2017) suggests an abrupt change
87 in structural parameters in the 10-20 GPa pressure interval, whereas a change in axial
88 compressibility has been observed above 45 GPa in X-ray diffraction experiments (Gleason et al.
89 2013). Both changes have been interpreted as the onset of the $P2_1nm$ to *Pnnm* phase transition due
90 to hydrogen bond symmetrisation. No change in axial compressibility of ε-FeOOH has been
91 reported in experimental works up to 24 GPa (Suzuki 2010, 2016; Ikeda et al. 2019), although a
92 change in the adiabatic bulk modulus, K_S, is visible above 17 GPa (Ikeda et al. 2019). It is therefore
93 not yet clear how the substitution of Al for Fe^{3+} at the octahedral site of the $P2_1nm$ structure effect

94 on the hydrogen bonding behaviour. Note, however, that a $P2_1nm$ to $Pnnm$ phase transition
95 associated with a change in axial compressibility has been reported close to 10 GPa for Fe-bearing
96 δ-AlOOH samples (Ohira et al. 2019) i.e. at a pressure very close to that where the same
97 transformation is observed for the δ-AlOOH end-member. The stability and compressibility of
98 these high-pressure phases have been studied extensively using both experimental techniques and
99 first principle calculations (Vanpeteghem et al. 2002; Panero and Stixrude 2004; Xue and Kanzaki
100 2007; Sano-Furukawa et al. 2008, 2009; Otte et al. 2009; Tsuchiya and Tsuchiya 2009; Suzuki
101 2010, 2016; Gleason et al. 2013; Cedillo et al. 2016; Mashino et al. 2016; Thompson et al. 2017;
102 Ohira et al. 2019).
103 Two early experimental works, Vanpeteghem et al. (2002) and Suzuki (2009), report very
104 discrepant compressibility results for δ-AlOOH, the first giving a bulk modulus, K_{T0}, of 252(3)
105 GPa with the first pressure derivative, K'_{T0}, fixed to 4 and the second giving K_{T0} = 124(2) GPa
106 with K'_{T0} = 13.5(7). No phase transition, however, was observed in these two studies, in spite of
107 covering a pressure range between room pressure and 17 – 22 GPa. (Sano-Furukawa et al. 2009)
108 reports a K_{T0} = 152(2) GPa with K'_{T0} fixed to 4 for the $P2_1nm$ structure. This value is very similar
109 to those reported for the Fe-bearing δ-AlOOH samples studied by Ohira et al. (2019). First
110 principle calculation studies give in general bulk moduli larger than 152 GPa for the $P2_1nm$
111 structure, however, there is a general agreement on the fact that the $Pnnm$ structure of δ-AlOOH
112 is stiffer than the $P2_1nm$ structure. The bulk modulus of the $P2_1nm$ structure of ε-FeOOH also is
113 not very well constrained, although most values are smaller than those reported for δ-AlOOH
114 (Suzuki 2010, 2016; Gleason et al. 2013; Ikeda et al. 2019). Only an early study, Gleason et al.
115 (2008) reported a value of K_{T0} = 158(5) GPa with K'_{T0} fixed to 4 obtained by fitting high-pressure
116 and temperature powder diffraction data, whereas a theoretical study (Thompson et al. 2017)

reported a value of K_{T0} = 188 with K'_{T0} = 5.19. The *Pnnm* structure of ε-FeOOH also appears stiffer than the $P2_1nm$ structure, however this is a purely theoretical observation, since no compressibility study for the high-symmetry phase of this material has been reported so far.

All mentioned studies have focused their attention on characterising the behaviour of these high-pressure phases at conditions of the deep Earth's interior given their importance as possible hydrogen carriers in the lower mantle. Only few studies have paid attention at the evolution of the hydrogen bond and possible isotope effects (Sano-Furukawa et al. 2008, 2009, 2018; Kuribayashi et al. 2014). Hydrogen bond symmetrisation is bound to occur on all OH···O-bearing compounds once the O···O distance reaches a critical value below 2.5 – 2.4 Å (Holzapfel 1972; Benoit and Marx 2005) and it has been reported for example in ice VII (e.g. (Meier et al. 2018) and reference therein) and in goethite (Xu et al. 2013). It has also been shown that disorder of the hydrogen bond occurs as a precursor to symmetrisation (Figure 1) and is responsible for the $P2_1nm$ to *Pnnm* phase transformation in δ-AlOOH (Sano-Furukawa et al. 2018). Constraining the elastic response associated with the evolution of the hydrogen bond and the consequent $P2_1nm$ to *Pnnm* transition can, therefore, give remarkable insight into the symmetrization process and its influence on the physical properties of hydrous materials in general.

The aim of this study is to determine the compressibility and the variation of the full elastic tensor of an Fe-bearing δ-AlOOH across the $P2_1nm$ to *Pnnm* transition in order to shed light on the elastic behaviour responsible for the major change of the axial compressibility observed during the transformation. By choosing an Fe-bearing sample we also aim at constraining the effect of Fe^{3+}, i.e. cation substitution, on the evolution of the hydrogen bond.

Materials and Methods

Single crystals of δ-(Al,Fe)OOH (sample H4765) were synthesised at 21 GPa and 1473 K in a multi-anvil apparatus following the same experimental procedure described in Kawazoe et al. (2017). A finely ground mixture of $Al(OH)_3$ and 96% ^{57}Fe-enriched Fe_2O_3 was used as a starting material. The powder was loaded in an $Au_{80}Pd_{20}$ capsule, which was then closed and sealed by welding. The capsule was inserted in a 10 mm Cr-doped MgO octahedral cell assembly with a $LaCrO_3$ furnace. WC cubes with 4 mm truncated edges were used as second stage anvils. The cell assembly was first compressed to the desired pressure and then heated at a constant rate of 100 K/min. Temperature was held constant for 4 h and quenched by cutting the power supply. After recovering the run products, single crystals were selected under a polarizing microscope based on absence of inclusions and sharp optical extinction, and used for chemical analyses, Mössbauer spectroscopy, X-ray diffraction characterization and Brillouin scattering measurements. The chemical composition of the run products was determined using an electron probe micro-analyzer operated in wavelength dispersive mode (JEOL JXA-8100) installed at the Bayerisches Geoinstitut. Al_2O_3 corundum and natural andradite were used as standards for Al and Fe respectively. Mössbauer spectroscopy measurements were performed on large single crystals of δ-(Al,Fe)OOH using a constant acceleration Mössbauer spectrometer equipped with a ^{57}Co point source (McCammon 1994). Mössbauer spectra were analysed and fitted with the MossA software (Prescher et al. 2012) using Lorentzian doublets for Fe^{3+} . No Fe^{2+} was detected in the analyzed spectra. All Fe present in samples H4765 is in the ferric state, therefore the averaged composition of the crystals studied is $Al_{0.973(5)}Fe^{3+}_{0.027(8)}OOH$, named hereafter as Fe3.

Large single-crystals were selected according to their sharp diffraction peak profiles (less than 0.07° in ω-scan) measured using ω-scan rotations on a Huber X-ray diffractometer equipped with non-monochromated Mo-radiation and a point detector. Two selected crystals, H4765x1 and

H4765x2 were oriented relative to the Cartesian indices (e_1, e_2, e_3), where H4765x1 (0.103, 0.836, 0.539) and H4765x2 (0.7842, 0.021, 0.620), respectively, with $e_2 \| b$ and $e_3 \| c$. Both platelets were double-sided polished to a thickness of 15 μm. The two Fe3 platelets were cut into several half-circles (Marquardt and Marquardt 2012; Schulze et al. 2017) with a FEI Scios focused ion beam machine using an acceleration voltage of 30 kV and an ion beam current of 20 nA. High-pressure measurements were carried out in a piston-cylinder BX90 diamond anvil cell with an opening angle of 90° (Kantor et al. 2012) equipped with Boehler-Almax type diamonds (Boehler and De Hantsetters 2004) having a culet size of 400 μm. A Re gasket was indented down to 65 μm and a 250 μm in diameter hole was drilled in the center of the indentation. The two FIB-cut Fe3 crystals were loaded together in the same DAC with a ruby crystal for pressure determination and Ne or He were loaded as quasi-hydrostatic pressure transmitting media using a gas loading apparatus (Klotz et al. 2009). Simultaneous high-pressure single-crystal X-ray diffraction and Brillouin scattering experiments up to 9.92(5) GPa were conducted using the system installed at the Bayerisches Geoinstitut (Trots et al. 2011). For X-ray diffraction measurements, a Huber diffractometer coupled with an ultra-high intensity Mo rotating anode X-ray source FR-E+ SuperBright from Rigaku and a multilayer VaryMax^{TM} focusing optics (800 mm focal point) was used. The diffractometer was equipped with a point detector and was driven by the SINGLE software (Angel and Finger 2011). The unit-cell lattice parameters of both crystals (Table 1) were determined by centering up to 17 Bragg reflections ($21° < 2\theta < 40°$) in eight positions according to the procedure described by (King and Finger 1979). Brillouin scattering measurements were performed in a 80° symmetric/platelet scattering geometry using a coherent Verdi V2 solid state Nd:YVO_4 frequency doubled laser (λ_0 = 532.0 nm) at the power of 100-150 mW. A six-pass Sandercock-type piezoelectrically driven scanning tandem Fabry-Perot interferometer (Lindsay et

al. 1981) with 4 mm plate spacing was used in combination with a single pixel photon counter detector (Hamamatsu). Brillouin spectroscopy measurements were performed at eight different pressure points included room pressure up to 9.92(5) GPa. Brillouin spectra were collected for each pressure point and for each crystal at different χ orientations at 20° interval for the whole 360° χ range. Each spectrum was collected for at least 1 hour. The measured frequency shifts are directly converted into acoustic wave velocities using the calibration obtained at ambient condition from the measurement of a fused silica standard. The Brillouin signals were analysed using pseudo-Voigt function implemented in PeakFIT software to fit inelastic and elastic contributions to the spectrum. The final peak positions were calculated as an arithmetic mean between Stokes and anti-Stokes contributions. Ghosts were used as internal calibration for the channel-frequency conversion. According to the used scattering geometry, frequencies were converted into velocity using the equation (Whitfield et al. 1976; Speziale et al. 2014):

$$v = \frac{\Delta\omega\,\lambda_0}{2\sin\left(\frac{\Theta ext}{2}\right)} \quad (1)$$

Where $\Delta\omega$ is the measured frequency shift, λ_0 is the laser wavelength and Θext is the external scattering angle (80°). Uncertainties in the velocity values were determined by the propagation of the uncertainties resulting from individual peak fitting, and the standard deviation between Stokes and anti-Stokes contributions. The elastic tensor of the $P2_1nm$ to $Pnnm$ orthorhombic phases of δ-(Al,Fe)OOH consists of nine independent elastic coefficients reported in the following in Voigt notation: C_{11}, C_{22}, C_{33}, C_{44}, C_{55}, C_{66}, C_{12}, C_{13}, C_{23}. These were obtained at each pressure by fitting the variation with χ orientation of the acoustic compressional velocity, v_P, and the two shear wave velocities, v_{S1} and v_{S2}, obtained for both Fe3 crystals using the Christoffel equation (Haussühl 2007):

208 $$\left|C_{ijkl}n_j n_l - \rho v^2 \delta_{ik}\right| = 0 \quad (2)$$

209 where C_{ijkl} are the elastic stiffness coefficients, $n_j n_l$ the phonon propagation direction, ρ the density
210 and δ_{ik} the Kronecker delta. The fitting procedure is implemented into Origin 2018 program as
211 described in details by Buchen (2018). The density used for the fitting was that obtained from the
212 unit-cell volume measured by means of X-ray diffraction at the same pressure points as the
213 Brillouin data collections.
214
215 **Results and Discussion**
216 *$P2_1nm$ to Pnnm transition of δ-(Al,Fe)OOH*
217 The evolution of the 0-30 reflection of sample H4765x1 has been followed as a function of pressure
218 (Figure 2) in order to pin point the onset of the *$P2_1nm$* to *Pnnm* phase transition. This reflection is
219 intense in the *$P2_1nm$* space group and it is a systematic extinction in the *Pnnm* space group in
220 which only the 0k0, k = 2n reflections can be observed. The intensity of this reflections has been
221 normalised with respect to the 1-30 reflection which is present in both space groups. The intensity
222 of the 0-30 reflection decreases with increasing pressure and disappears between 7.59(3) GPa and
223 7.94(2) GPa. Note that we have done very long collection of the 0-30 reflection profile in order to
224 enhance the signal to noise ratio particularly close to the transition pressure. The quality and aspect
225 of the single crystals studied remained unchanged after the phase transformation. A previous study
226 (Sano-Furukawa et al. 2009) has observed the disappearance of the 010 and 120 reflections of δ-
227 AlOOH at lower pressures (i.e. at 4.83 GPa and at 6.53 GPa, respectively) in their neutron powder
228 diffraction patterns, however Kuribayashi et al. (2014), analyzing single-crystal X-ray diffraction
229 data of δ-AlOOH, reported the disappearance of selected 0kl reflections with k + l = odd (i.e.
230 systematic extension in the *Pnnm* space group) between 6.1 and 8.4 GPa in excellent agreement

231 with our results. The disappearance of the 0-30 reflection coincides with the change in slope of the
232 axial unit-cell axes ratios a/b, b/c and a/c (Figure 3). A similar change in slope is observed at the
233 same pressure of about 8 GPa also for the axial unit-cell axes ratios of δ-AlOOH (Sano-Furukawa
234 et al. 2009; Kuribayashi et al. 2014), suggesting that the incorporation of 3% of Fe^{3+} into the δ-
235 AlOOH structure has a negligible effect on the $P2_1nm$ to $Pnnm$ phase transition. The unit-cell
236 lattice parameters for two Fe-bearing samples of δ-AlOOH containing 5% and 12% of Fe^{3+} (Fe5
237 and Fe12, respectively) also show a similar behavior (Figure 2) (Ohira et al. 2019), suggesting that
238 also for richer Fe-bearing δ-AlOOH samples there is little if any influence of the Fe^{3+} substitution
239 on the $P2_1nm$ to $Pnnm$ phase transition, at least for the compositions investigated so far. The very
240 different behavior of the axial ratios obtained for ε-FeOOH (Ikeda et al. 2019) is likely due to the
241 different axial compressibility of the Fe-end-member. A substituting atom in a solid solution can
242 affect the transition point of the end-member only once the microscopic strain field created by its
243 substitution start to overlap. As Fe^{3+} atoms are added into the δ-AlOOH structure, we can expect
244 the $P2_1nm$ to $Pnnm$ transition pressure to remain constant until a critical composition, which is a
245 direct reflection of the magnitude of the strain fields created by the cation substitution (e.g.
246 Hayward and Salje 1996; Carpenter et al. 1999, 2009; Boffa Ballaran et al. 2000). As there are two
247 cation sites in one unit-cell, the richest Fe-bearing δ-AlOOH sample Fe12 studied by Ohira et al.
248 (2019) consists of about one atom of Fe^{3+} every 4 unit-cells. Since no effect on the transition
249 pressure is observed, we can therefore expect that the distortion field around Fe^{3+} is smaller than
250 16 Å and a much larger concentration will be necessary to observe any change in the behaviour of
251 the $P2_1nm$ to $Pnnm$ phase transition due to cation substitution.
252
253 *Compressibility of $P2_1nm$ δ-(Al,Fe)OOH*

254 The variations of the unit-cell parameters and volume (Table 1) of samples H4765 normalised with
255 respect to their room pressure values are reported in Figure 4. The data collected for the two
256 crystals are indistinguishable up to the last pressure measured. The unit-cell volume data up to
257 6.46(2) GPa have been fitted using a 3rd-order Birch-Murnaghan Equation of State (BM3 EoS)
258 (Birch 1947) using the program EoSFit7 (Angel et al. 2014; Gonzalez-Platas et al. 2016). We have
259 neglected the volume data between 6.5 GPa and 8 GPa in order to give insight on possible volume
260 anomalies associated with the $P2_1nm$ to $Pnnm$ phase transition. The resulting BM3 EoS parameters
261 obtained refining simultaneously the volume at room pressure, V_0 as well as K_{T0} and K'_{T0} using
262 data weighted by the uncertainties in both P and V are the following: V_0 = 56.695(3) (**Å**^{3}), K_{T0} =
263 149.9(11) GPa and K'_{T0} = 3.7(4) (Table 2). The bulk modulus value obtained in this study is
264 practically identical to that of the δ-AlOOH end-member reported by Sano-Furukawa et al. (2009)
265 and of the Fe5 sample studied by Ohira et al. (2019), once the uncertainties have been taken into
266 account. These results gives a strong constrain on the isothermal bulk modulus of δ-AlOOH and
267 at the same time points out to the fact that a 3% of Fe^{3+} substitution has no effect on the
268 compressibility of the δ-AlOOH end-member. Given the high-quality of the unit-cell lattice
269 parameter data collected in this study, we can observe a small deviation of the volume data from
270 the BM3 EoS fit (Figure 4b) above 6.5 GPa, i.e. close to the $P2_1nm$ to $Pnnm$ transition pressure.
271 The volume data show smaller values than expected, suggesting that the low-symmetry $P2_1nm$
272 phase of Fe3 presents a softening of the bulk modulus in the neighborhood of the transition similar
273 to that observed in other mineral phase transformations (Arlt and Angel 2000; McConnell et al.
274 2000; Carpenter and Zhang 2011).
275

276 The axial compressibility (Figure 4a) follows the scheme $\beta_b > \beta_a > \beta_c$ agreement with what reported
277 for data below 10 GPa in Sano-Furukawa et al. (2009). The linear moduli, *M*, and their first
278 pressure derivatives, *M'*, have been obtained fitting the unit-cell parameters up to 6.46(2) GPa with
279 linearized BM3 EoS implemented in EosFit7 (Angel et al. 2014; Gonzalez-Platas et al. 2016) and
280 the resulting parameters are reported in Table 2. Deviation from the BM3 fit is clearly visible for
281 the data points relative to the *b*-axis close to the $P2_1nm$ to *Pnnm* transition pressure, the *a*-axis
282 values collected at 7.06(3) GPa, 7.44(1) GPa and 7.59(3) GPa are only slightly smaller than those
283 expected from the BM3 fit, whereas no deviation can be observed for the *c*-axis.
284
285 *Elastic tensor of δ-(Al,Fe)OOH*
286 Typical Brillouin spectra collected for the $P2_1nm$ low-symmetry phase and for the *Pnnm* high-
287 symmetry phase of one crystal of Fe3 as well as the acoustic velocities obtained for both crystals
288 at the same pressures are shown in Figure 5 as example. The elastic coefficients obtained at each
289 pressure are reported in Table 3 and their variations with pressure are shown in Figure 6. The room
290 pressure shear components, C_{44}, C_{55} and C_{66} and the off-diagonal components of the elastic tensor
291 are in general agreement with those obtained for $P2_1nm$ δ-AlOOH by *ab-initio* calculations
292 (Tsuchiya and Tsuchiya 2009; Cortona 2017; Pillai et al. 2018). A larger discrepancy is found for
293 the values of C_{66} and C_{22} which are very similar in the theoretical studies whereas they differ of 68
294 GPa with $C_{11} > C_{22}$ in this study. The elastic components show a smooth variation with pressure
295 up to 6.46(2) GPa that can be described by finite strain expressions (Stixrude and Lithgow-
296 Bertelloni 2005):

297
$$C_{ijkl} = (1+2f)^{\frac{5}{2}}\left(C_{ijkl,0} + \left(3K_0C'_{ijkl,0} - 5C_{ijkl,0}\right)f + \right.$$
$$\left. +\left(6K_0C'_{ijkl,0} - 14C_{ijkl,0} - \frac{3}{2}K_0\delta_{kl}^{ij}(3K_0 - 16)\right)f^2\right) \quad (3)$$

298 where $C'_{ijkl,0}$ are the first pressure derivative of the elastic stiffness coefficients.

299 The major increase with pressure is observed for the C_{11} component, followed by C_{33} and then by
300 C_{22} and C_{66}. This is in contrast with what observed in theoretical studies (Tsuchiya and Tsuchiya
301 2009; Cortona 2017; Pillai et al. 2018) which report the largest increases for C_{22} and C_{11} up to the
302 hydrogen bond symmetrization. Above 6.5 GPa we observed a large softening of the C_{22}, C_{12} and
303 C_{23} components (Figure 6), in agreement with the observed softening of the unit-cell volume
304 (Figure 2b). Discontinuity in some of the elastic stiffness coefficients have been reported in the
305 theoretical studies at a pressure of 17 GPa and have been interpreted as result from the hydrogen
306 bond symmetrisation (Tsuchiya and Tsuchiya 2009; Cortona 2017; Pillai et al. 2018). However,
307 the changes reported in Pillai et al. (2018) are not in agreement with our observation since those
308 authors calculated a softening of the C_{11} and C_{13} components and a hardening of the C_{22} and C_{23}
309 components. The softening of the C_{22}, C_{12} and C_{23} components observed in this study is very likely
310 associated with the softening of O-H stretching modes which has been reported in a first principle
311 calculation (Tsuchiya et al. 2008). The optical softening occurs at the hydrogen symmetrisation
312 pressure which Tsuchiya et al. (2008) calculated to be about 30 GPa, however the results obtained
313 in this study suggest that softening of the O-H stretching modes may be associated with the onset
314 of the hydrogen bond disorder and not with its symmetrisation as it is associated with the $P2_1nm$
315 to $Pnnm$ phase transformation. The axial compressibility of a material can be calculated through
316 the sum of elements of the compliance matrix which can be obtained by inverting the elastic tensor
317 matrix (Nye 1985):

318 $$\beta_i = S_{i1} + S_{i2} + S_{i3} \quad (4)$$

319 where β_i is the axial compressibility of the i-axis and S_{ij} are the compliance coefficients. The
320 axial compressibilities calculated with Equation 4 are (values in GPa^{-1}): β_a = 0.00205(3), β_b

321 =0.00281(3) and β_c =0.00154(2) are in very good agreement with the inverse of the axial bulk
322 moduli reported in (Table 2). The compressibility scheme $\beta_b > \beta_a > \beta_c$ is due to different response
323 of the δ-(Al,Fe)OOH structure to compression, being the *a*-*b* plane more compressible due to the
324 presence of the small hydrogen inside an octahedral site (Figure 1a), whereas chain of edge-sharing
325 octahedra are elongated along the *c*-axis giving rise to a stiffer unit to be compressed. With
326 increasing pressure, however the compressibility of the *a*-axis (and to a smaller extent that of the
327 *b*-axis) decreases quickly as indicated by its large moduli first pressure derivative. This is likely
328 due to the stiffening of the O···O distance defining the hydrogen bond which is indeed one of the
329 most compressible as reported for the $P2_1nm$ phase of δ-AlOOD (Sano-Furukawa et al. 2008), but
330 stiffen faster than the other O···O distances due to the onset of the disordered hydrogen bond (Sano-
331 Furukawa et al. 2018). This large change in compressibility of the *a*- and *b*-axes are well described
332 by the strong increases of the C_{11} and C_{22} elastic components which are the major contribution to
333 the calculation of the axial compressibilities given their much larger values with respect to those
334 of the off-diagonal components. The elastic tensor obtained at 9.92(5) GPa for the *Pnnm* phase of
335 Fe3 is in good agreement is in good agreement with that of δ-AlOOH at 10 GPa reported by
336 Cortona (2017), showing a major stiffening of the C_{22}. From the inversion of this elastic tensor,
337 we have calculated the axial compressibilities for the *Pnnm* phase of Fe3 at 9.92(5) GPa, obtaining
338 (values in GPa^{-1}): β_a =0.00138(3), β_b =0.00129(3) and β_c =0.00139(2). These results show
339 indeed that the $P2_1nm$ to *Pnnm* phase transformation gives rise to a major change in the axial
340 compressibility scheme in agreement with what observed above 10 GPa for the δ-AlOOH end-
341 member (Sano-Furukawa et al. 2009) and for Fe-bearing δ-AlOOH (Ohira et al. 2019).
342
343 *Aggregate properties of δ-(Al,Fe)OOH*

344 The Reuss and Voigt bounds of the adiabatic bulk, K_S, and shear, G, moduli were calculated at
345 each pressure using the elastic and compliance tensors (Nye 1985). The arithmetic average
346 between the two bounds has been used to calculate the Reuss-Voigt-Hill average to represent the
347 aggregate bulk and shear moduli of a composite material (Hill 1952; Watt et al. 1976), Table 4.
348 The variation of adiabatic bulk and shear moduli with pressure are shown in Figure 7. As expected,
349 there is large softening of the bulk modulus above 6.5 GPa associated with $P2_1nm$ to $Pnnm$ phase
350 transformation. Moreover, a major jump is visible at 9.92(5) GPa after the transition, where the
351 bulk modulus is 60 GPa larger than that at 6.46(2) GPa. The shear modulus, instead increases
352 smoothly with pressure and no jump is observed after the phase transition. The Reuss bound of the
353 adiabatic bulk modulus (Table 4) obtained from the inversion of the compliance matrix calculated
354 at room pressure is only slightly larger than the isothermal K_{T0} obtained from fitting the P-V data
355 (Table 1) using a BM3 EOS. The aggregate values of K_{S0} and G_0 (K_{VRH0} and G_{VRH0} , Table 4) at
356 room pressure also are smaller than those reported for δ-AlOOH in theoretical studies (Tsuchiya
357 and Tsuchiya 2009; Cortona 2017; Pillai et al. 2018), except for the G value reported by Tsuchiya
358 and Tsuchiya (2009) which is 10 GPa smaller than that observed in this study. The Fe^{3+}
359 substitution appears to decrease both the incompressibility and the resistance to shear stress since
360 the values reported for ε-FeOOH [K_{S0} = 133 (7) GPa and G_0 = 71 (2) GPa, Ikeda et al. 2019] are
361 much smaller than those obtained in this study.
362 The aggregate compressional, v_P, and shear, v_S, wave velocities (Table 4), were calculated
363 following the Adams-Williamson relations $v_P = \sqrt{\frac{Ks+4/3G}{\rho}}$ and $v_S = \sqrt{\frac{G}{\rho}}$. respectively, by using
364 the elastic moduli determined with the Reuss-Voigt-Hill average and density measured using
365 single-crystal X-ray diffraction on the same crystals. The room pressure v_P and v_S values of the
366 sample investigated in this study are respectively 3.6% and 6.8% larger than those reported by

Mashino et al. (2016) for the δ-AlOOH end-member. Because Fe^{3+} substitution appears to decrease the wave velocities according to an ultrasonic study of ε-FeOOH (Ikeda et al. 2019), the difference between our sample and the results of Mashino et al. (2016) cannot be ascribed to their different compositions. Instead, the difference may be due to the presence of some preferred orientation in the polycrystalline sample studied by Mashino et al. (2016) which may give rise to some deviation from the properties of a perfectly random distributed aggregate due to the large anisotropy of δ-AlOOH. The variations with pressure of the wave velocities of Fe3 are shown in Figure 8. As v_P depends on the bulk modulus variation, it is possible to observe a slight softening above 6.46(2) GPa and a jump after the $P2_1nm$ to $Pnnm$ phase transition, whereas v_S show a smooth evolution with pressure. Mashino et al. (2016) observed a major change in both v_P and v_S wave velocities above 20 GPa and they suggested that such changes were due to the hydrogen bond symmetrisation. A closer inspection of Figure 4 reported in Mashino et al. (2016), however, reveals a jump in v_P at pressure between 5 and 7 GPa, although the paucity of data in that region does not allow a more careful analysis. Our results together with those of Mashino et al. (2016) show that any change in hydrogen bond character may have large influence on the elastic response of a material. Further analyses are necessary to shed light on whether elastic softening is not only associated with hydrogen bond disordering as clearly shown in this study but also with hydrogen bond symmetrisation.

Conclusion

The study of δ-(Al,Fe)OOH single crystals containing about 3% of iron has allowed to constrain the elastic behavior of this high-pressure oxy-hydroxide phases through the $P2_1nm$ to $Pnnm$ transition. This transition, associated with the disordering of the hydrogen bond in the *a*-*b* plane

of δ-(Al,Fe)OOH, occurs between 7.59(3) GPa and 7.94(2) GPa as demonstrated by the disappearance of the 0-30 reflection which is systematically absent in the *Pnnm* space group. The equation of state of the $P2_1nm$ δ-(Al,Fe)OOH structure has been accurately constrained and is in agreement with recent studies (Sano-Furukawa et al. 2009; Ohira et al. 2019). The full elastic tensor of sample H4765 has been determined up to 9.92 (5) GPa and a large softening of the C_{22}, C_{12} and C_{23} has been observed above 6.5 GPa and before the transformation to the high-symmetry phase. As a consequence, a large softening is also present in the adiabatic bulk modulus close to the transition and is reflected in a small deviation of the *P-V* data from the $P2_1nm$ BM3 EoS. Softening of these elastic components may be associated with the softening of the OH infra-red stretching mode occurring with increasing pressure (Tsuchiya et al. 2008) and it is due to the change in the strength of the hydrogen bond as the O-H···O distances change with pressure. It is very likely for a similar softening to occur also in other high-pressure hydroxide phases, as for example Al-phase D (Pamato et al. 2015), when compressed at the extreme conditions of the Earth's interior.

References

Angel, R.J., and Finger, L.W. (2011) SINGLE: a program to control single-crystal diffractometers. Journal of Applied Crystallography, 44, 247–251.

Angel, R.J., Alvaro, M., and Gonzalez-Platas, J. (2014) EosFit7c and a Fortran module (library) for equation of state calculations. Zeitschrift für Kristallographie - Crystalline Materials, 229.

Arlt, T., and Angel, R.J. (2000) Displacive phase transitions in C-centred clinopyroxenes: spodumene, LiScSi2O6 and ZnSiO3. Physics and Chemistry of Minerals, 27, 719–731.

Bell, D.R., and Rossman, G.R. (1992) Water in Earth's Mantle: The Role of Nominally Anhydrous Minerals. Science, 255, 1391–1397.

Benoit, M., and Marx, D. (2005) The Shapes of Protons in Hydrogen Bonds Depend on the Bond Length. ChemPhysChem, 6, 1738–1741.

417 Birch, F. (1947) Finite Elastic Strain of Cubic Crystals. Physical Review, 71, 809–824.

418 Boehler, R., and De Hantsetters, K. (2004) New anvil designs in diamond-cells. High Pressure
419 Research, 24, 391–396.

420 Boffa Ballaran, T., Angel, R.J., and Carpenter, M.A. (2000) High-pressure transformation
421 behaviour of the cummingtonite-grunerite solid solution. European Journal of
422 Mineralogy, 12, 1195–1213.

423 Bolfan-Casanova, N. (2005) Water in the Earth's mantle. Mineralogical Magazine, 69, 229–257.

424 Bolotina, N.B., Molchanov, V.N., Dyuzheva, T.I., Lityagina, L.M., and Bendeliani, N.A. (2008)
425 Single-crystal structures of high-pressure phases FeOOH, FeOOD, and GaOOH.
426 Crystallography Reports, 53, 960–965.

427 Buchen, J. (2018) The Elastic Properties of Wadsleyite and Stishovite at High Pressures :
428 Tracing Deep Earth Material Cycles, 199 p. University of Bayreuth.

429 Carpenter, M.A., and Zhang, Z. (2011) Anelasticity maps for acoustic dissipation associated with
430 phase transitions in minerals. Geophysical Journal International, 186, 279–295.

431 Carpenter, M.A., Boffa Ballaran, T., and Atkinson, A.J. (1999) Microscopic strain, local
432 structural heterogeneity and the energetics of silicate solid solutions. Phase Transitions,
433 69, 95–109.

434 Carpenter, M.A., McKnight, R.E.A., Howard, C.J., Zhou, Q., Kennedy, B.J., and Knight, K.S.
435 (2009) Characteristic length scale for strain fields around impurity cations in perovskites.
436 Physical Review B, 80, 214101.

437 Cedillo, A., Torrent, M., and Cortona, P. (2016) Stability of the different AlOOH phases under
438 pressure. Journal of Physics: Condensed Matter, 28, 185401.

439 Cortona, P. (2017) Hydrogen bond symmetrization and elastic constants under pressure of δ-
440 AlOOH. Journal of Physics: Condensed Matter, 29, 325505.

441 Gleason, A.E., Jeanloz, R., and Kunz, M. (2008) Pressure-temperature stability studies of
442 FeOOH using X-ray diffraction. American Mineralogist, 93, 1882–1885.

443 Gleason, A.E., Quiroga, C.E., Suzuki, A., Pentcheva, R., and Mao, W.L. (2013) Symmetrization
444 driven spin transition in ε-FeOOH at high pressure. Earth and Planetary Science Letters,
445 379, 49–55.

446 Gonzalez-Platas, J., Alvaro, M., Nestola, F., and Angel, R. (2016) EosFit7-GUI: a new graphical
447 user interface for equation of state calculations, analyses and teaching. Journal of Applied
448 Crystallography, 49, 1377–1382.

449 Haussühl, S. (2007) Physical Properties of Crystals: An Introduction, 439 p. Wiley-VCH.

450 Hayward, S.A., and Salje, E.K.H. (1996) Displacive phase transition in anorthoclase; the
451 "plateau effect" and the effect of T1-T2 ordering on the transition temperature. American
452 Mineralogist, 81, 1332–1336.

453 Hill, R.S.R. (1952) The Elastic Behaviour of a Crystalline Aggregate. Proceedings of the
454 Physical Society. Section B.

455 Holzapfel, W.B. (1972) On the Symmetry of the Hydrogen Bonds in Ice VII. The Journal of
456 Chemical Physics, 56, 712–715.

457 Ikeda, O., Sakamaki, T., Ohashi, T., Goto, M., Higo, Y., and Suzuki, A. (2019) Sound velocity
458 measurements of ε–FeOOH up to 24 GPa. Journal of Mineralogical and Petrological
459 Sciences, 114, 155–160.

460 Kantor, I., Prakapenka, V., Kantor, A., Dera, P., Kurnosov, A., Sinogeikin, S., Dubrovinskaia,
461 N., and Dubrovinsky, L. (2012) BX90: A new diamond anvil cell design for X-ray
462 diffraction and optical measurements. Review of Scientific Instruments, 83, 125102.

463 Kawazoe, T., Ohira, I., Ishii, T., Ballaran, T.B., McCammon, C., Suzuki, A., and Ohtani, E.
464 (2017) Single crystal synthesis of δ-(Al,Fe)OOH. American Mineralogist, 102, 1953–
465 1956.

466 King, H.E., and Finger, L.W. (1979) Diffracted beam crystal centering and its application to
467 high-pressure crystallography. Journal of Applied Crystallography, 12, 374–378.

468 Klotz, S., Chervin, J.-C., Munsch, P., and Marchand, G.L. (2009) Hydrostatic limits of 11
469 pressure transmitting media. Journal of Physics D: Applied Physics, 42, 075413.

470 Komatsu, K., Kuribayashi, T., Sano, A., Ohtani, E., and Kudoh, Y. (2006) Redetermination of
471 the high-pressure modification of AlOOH from single-crystal synchrotron data. Acta
472 Crystallographica Section E: Structure Reports Online, 62, i216–i218.

473 Kuribayashi, T., Sano-Furukawa, A., and Nagase, T. (2014) Observation of pressure-induced
474 phase transition of δ-AlOOH by using single-crystal synchrotron X-ray diffraction
475 method. Physics and Chemistry of Minerals, 41, 303–312.

476 Lindsay, S.M., Anderson, M.W., and Sandercock, J.R. (1981) Construction and alignment of a
477 high performance multipass vernier tandem Fabry–Perot interferometer. Review of
478 Scientific Instruments, 52, 1478–1486.

479 Liu, X., Matsukage, K.N., Nishihara, Y., Suzuki, T., and Takahashi, E. (2019) Stability of the
480 hydrous phases of Al-rich phase D and Al-rich phase H in deep subducted oceanic crust.
481 American Mineralogist, 104, 64–72.

482 Marquardt, H., and Marquardt, K. (2012) Focused ion beam preparation and characterization of
483 single-crystal samples for high-pressure experiments in the diamond-anvil cell. American
484 Mineralogist, 97, 299–304.

485 Mashino, I., Murakami, M., and Ohtani, E. (2016) Sound velocities of δ-AlOOH up to core-
486 mantle boundary pressures with implications for the seismic anomalies in the deep
487 mantle. Journal of Geophysical Research: Solid Earth, 121, 595–609.

488 McCammon, C.A. (1994) A Mössbauer milliprobe: Practical considerations. Hyperfine
489 Interactions, 92, 1235–1239.

490 McConnell, J.D.C., McCammon, C.A., Angel, R.J., and Seifert, F. (2000) The nature of the
491 incommensurate structure in åkermanite, Ca2MgSi2O7, and the character of its
492 transformation from the normal structure. Zeitschrift für Kristallographie - Crystalline
493 Materials, 215, 669–677.

494 Meier, T., Petitgirard, S., Khandarkhaeva, S., and Dubrovinsky, L. (2018) Observation of nuclear
495 quantum effects and hydrogen bond symmetrisation in high pressure ice. Nature
496 Communications, 9, 2766.

497 Nishi, M., Irifune, T., Tsuchiya, J., Tange, Y., Nishihara, Y., Fujino, K., and Higo, Y. (2014)
498 Stability of hydrous silicate at high pressures and water transport to the deep lower
499 mantle. Nature Geoscience, 7, 224–227.

500 Nishi, M., Kuwayama, Y., Tsuchiya, J., and Tsuchiya, T. (2017) The pyrite-type high-pressure
501 form of FeOOH. Nature, 547, 205–208.

502 Nishi, M., Tsuchiya, J., Kuwayama, Y., Arimoto, T., Tange, Y., Higo, Y., Hatakeyama, T., and
503 Irifune, T. (2019) Solid Solution and Compression Behavior of Hydroxides in the Lower
504 Mantle. Journal of Geophysical Research: Solid Earth, 124, 10231–10239.

505 Nye, J.F. (1985) Physical Properties of Crystals: Their Representation by Tensors and Matrices.
506 Oxford University Press.

507 Ohira, I., Ohtani, E., Sakai, T., Miyahara, M., Hirao, N., Ohishi, Y., and Nishijima, M. (2014)
508 Stability of a hydrous δ-phase, AlOOH–MgSiO2(OH)2, and a mechanism for water
509 transport into the base of lower mantle. Earth and Planetary Science Letters, 401, 12–17.

510 Ohira, I., Jackson, J.M., Solomatova, N.V., Sturhahn, W., Finkelstein, G.J., Kamada, S.,
511 Kawazoe, T., Maeda, F., Hirao, N., Nakano, S., and others (2019) Compressional
512 behavior and spin state of δ-(Al,Fe)OOH at high pressures. American Mineralogist, 104,
513 1273–1284.

514 Ohtani, E. (2015) Hydrous minerals and the storage of water in the deep mantle. Chemical
515 Geology, 418, 6–15.

516 Ohtani, E., Litasov, K., Suzuki, A., and Kondo, T. (2001) Stability field of new hydrous phase,
517 δ-AlOOH, with implications for water transport into the deep mantle. Geophysical
518 Research Letters, 28, 3991–3993.

519 Ono, S. (1998) Stability limits of hydrous minerals in sediment and mid-ocean ridge basalt
520 compositions: Implications for water transport in subduction zones. Journal of
521 Geophysical Research: Solid Earth, 103, 18253–18267.

522 Otte, K., Pentcheva, R., Schmahl, W.W., and Rustad, J.R. (2009) Pressure-induced structural and
523 electronic transitions in FeOOH from first principles. Physical Review B, 80, 205116.

524 Pamato, M.G., Myhill, R., Boffa Ballaran, T., Frost, D.J., Heidelbach, F., and Miyajima, N.
525 (2015) Lower-mantle water reservoir implied by the extreme stability of a hydrous
526 aluminosilicate. Nature Geoscience, 8, 75–79.

527 Panero, W.R., and Stixrude, L.P. (2004) Hydrogen incorporation in stishovite at high pressure
528 and symmetric hydrogen bonding in δ-AlOOH. Earth and Planetary Science Letters, 221,
529 421–431.

530 Peacock, S.M. (1990) Fluid processes in subduction zones. Science, 248, 329–337.

531 Pearson, D.G., Brenker, F.E., Nestola, F., McNeill, J., Nasdala, L., Hutchison, M.T., Matveev,
532 S., Mather, K., Silversmit, G., Schmitz, S., and others (2014) Hydrous mantle transition
533 zone indicated by ringwoodite included within diamond. Nature, 507, 221–224.

534 Pillai, S.B., Jha, P.K., Padmalal, A., Maurya, D.M., and Chamyal, L.S. (2018) First principles
535 study of hydrogen bond symmetrization in δ-AlOOH. Journal of Applied Physics, 123,
536 115901.

537 Prescher, C., McCammon, C., and Dubrovinsky, L. (2012) MossA: a program for analyzing
538 energy-domain Mössbauer spectra from conventional and synchrotron sources. Journal of
539 Applied Crystallography, 45, 329–331.

540 Sano, A., Ohtani, E., Kubo, T., and Funakoshi, K. (2004) In situ X-ray observation of
541 decomposition of hydrous aluminum silicate AlSiO3OH and aluminum oxide hydroxide
542 d-AlOOH at high pressure and temperature. Journal of Physics and Chemistry of Solids,
543 65, 1547–1554.

544 Sano-Furukawa, A., Komatsu, K., Vanpeteghem, C.B., and Ohtani, E. (2008) Neutron diffraction
545 study of δ-AlOOD at high pressure and its implication for symmetrization of the
546 hydrogen bond. American Mineralogist, 93, 1558–1567.

547 Sano-Furukawa, A., Kagi, H., Nagai, T., Nakano, S., Fukura, S., Ushijima, D., Iizuka, R.,
548 Ohtani, E., and Yagi, T. (2009) Change in compressibility of δ-AlOOH and δ-AlOOD at
549 high pressure: A study of isotope effect and hydrogen-bond symmetrization. American
550 Mineralogist, 94, 1255–1261.

551 Sano-Furukawa, A., Hattori, T., Komatsu, K., Kagi, H., Nagai, T., Molaison, J.J., dos Santos,
552 A.M., and Tulk, C.A. (2018) Direct observation of symmetrization of hydrogen bond in
553 δ-AlOOH under mantle conditions using neutron diffraction. Scientific Reports, 8, 1–9.

554 Schulze, K., Buchen, J., Marquardt, K., and Marquardt, H. (2017) Multi-sample loading
555 technique for comparative physical property measurements in the diamond-anvil cell.
556 High Pressure Research, 37, 159–169.

557 Speziale, S., Marquardt, H., and Duffy, T.S. (2014) Brillouin Scattering and its Application in
558 Geosciences. Reviews in Mineralogy and Geochemistry, 78, 543–603.

559 Stixrude, L., and Lithgow-Bertelloni, C. (2005) Thermodynamics of mantle minerals - I.
560 Physical properties. Geophysical Journal International, 162, 610–632.

561 Suzuki, A. (2009) Compressibility of the high-pressure polymorph of AlOOH to 17 GPa.
562 Mineralogical Magazine, 73, 479–485.

563 Suzuki A. (2010) High-pressure X-ray diffraction study of ε-FeOOH. Physics and Chemistry of
564 Minerals, 37, 153–157.

565 Suzuki A. (2016) Pressure–volume–temperature equation of state of ε–FeOOH to 11 GPa and
566 700 K. Journal of Mineralogical and Petrological Sciences, 111, 420–424.

567 Thompson, E.C., Campbell, A.J., and Tsuchiya, J. (2017) Elasticity of ε-FeOOH: Seismic
568 implications for Earth's lower mantle. Journal of Geophysical Research: Solid Earth, 122,
569 5038–5047.

570 Trots, D.M., Kurnosov, A., Vasylechko, L., Berkowski, M., Boffa Ballaran, T., and Frost, D.J.
571 (2011) Elasticity and equation of state of Li2B4O7. Physics and Chemistry of Minerals,
572 38, 561.

573 Tsuchiya, J., and Tsuchiya, T. (2009) Elastic properties of δ-AlOOH under pressure: First
574 principles investigation. Physics of the Earth and Planetary Interiors, 174, 122–127.

575 Tsuchiya, J., Tsuchiya, T., and Wentzcovitch, R.M. (2008) Vibrational properties of δ-AlOOH
576 under pressure. American Mineralogist, 93, 477–482.

577 Vanpeteghem, C.B., Ohtani, E., and Kondo, T. (2002) Equation of state of the hydrous phase δ-
578 AlOOH at room temperature up to 22.5 GPa. Geophysical Research Letters, 29, 1119.

579 Watt, J.P., Davies, G.F., and O'Connell, R.J. (1976) The elastic properties of composite
580 materials. Reviews of Geophysics, 14, 541–563.

581 Whitfield, C.H., Brody, E.M., and Bassett, W.A. (1976) Elastic moduli of NaCl by Brillouin
582 scattering at high pressure in a diamond anvil cell. Review of Scientific Instruments, 47,
583 942–947.

584 Wirth, R., Vollmer, C., Brenker, F., Matsyuk, S., and Kaminsky, F. (2007) Inclusions of
585 nanocrystalline hydrous aluminium silicate "Phase Egg" in superdeep diamonds from
586 Juina (Mato Grosso State, Brazil). Earth and Planetary Science Letters, 259, 384–399.

587 Xu, C., Nishi, M., and Inoue, T. (2019) Solubility behavior of δ-AlOOH and ε-FeOOH at high
588 pressures. American Mineralogist, 104, 1416–1420.

589 Xu, W., Greenberg, E., Rozenberg, G.Kh., Pasternak, M.P., Bykova, E., Boffa-Ballaran, T.,
590 Dubrovinsky, L., Prakapenka, V., Hanfland, M., Vekilova, O.Yu., and others (2013)
591 Pressure-Induced Hydrogen Bond Symmetrization in Iron Oxyhydroxide. Physical
592 Review Letters, 111, 175501.

593 Xue, X., and Kanzaki, M. (2007) High-Pressure δ-Al(OH)3 and δ-AlOOH Phases and
594 Isostructural Hydroxides/Oxyhydroxides: New Structural Insights from High-Resolution
595 1H and 27Al NMR. The Journal of Physical Chemistry B, 111, 13156–13166.

596

597 **Figures**

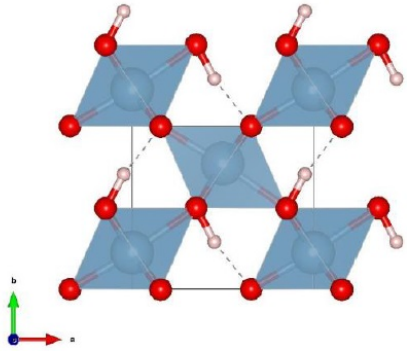

(a) $P2_1nm$ - Asymmetric hydrogen

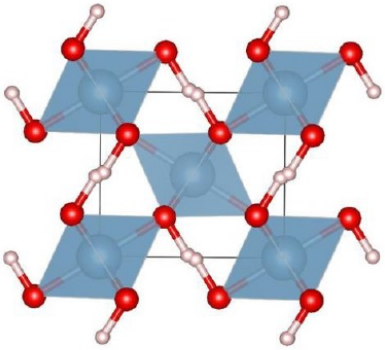

(b) $Pnnm$ - Hydrogen disorder

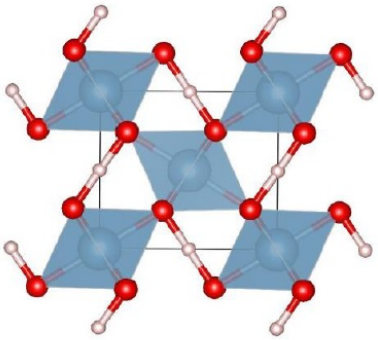

(c) $Pnnm$ - Symmetric hydrogen

598

599 **Figure 1.** Structural models of δ-Al,OOH polymorphs. (a) room pressure, structural data from

600 (Komatsu et al. 2006); (b) at 9.5 GPa, and (c) and 18 GPa. Structural data of (b) and (c) from

601 (Sano-Furukawa et al. 2018).

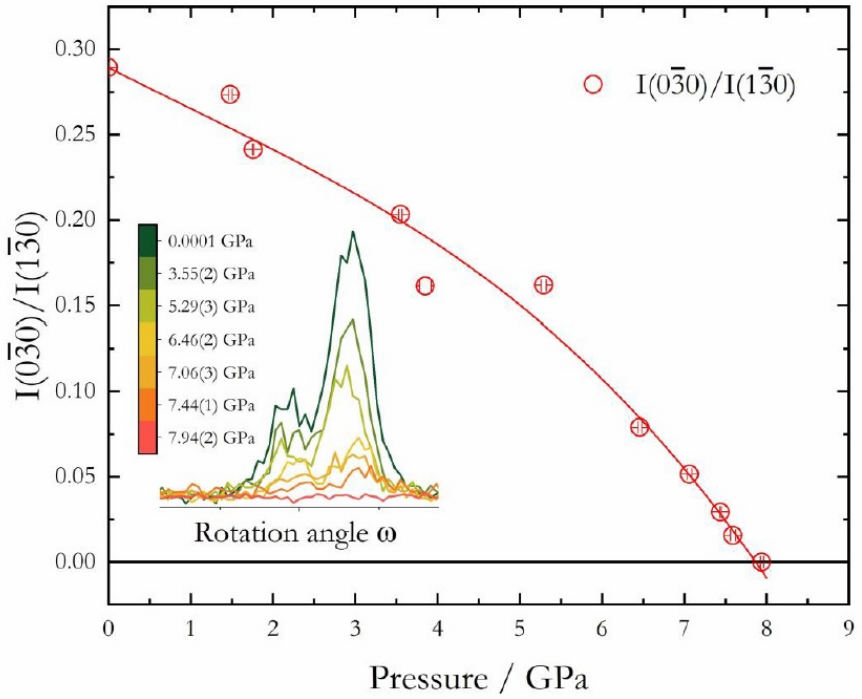

602 **Figure 2.** Evolution with pressure of the the 0-30 reflection, which is present in the $P2_1nm$ space
603 group and is a systematic absence in the *Pnnm* space group. The 0-30 reflection is normalized with
604 respect to the 1-30 reflection collected at the same pressure points.

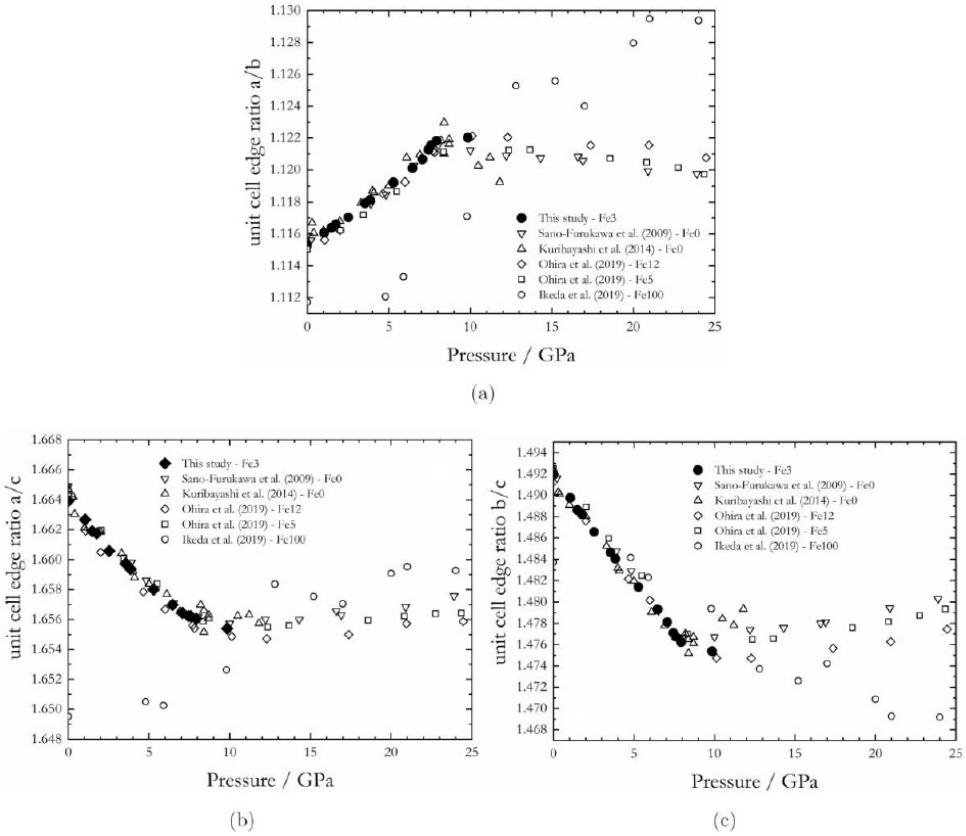

605 **Figure 3**. The axial unit-cell lattice parameters ratios variation with pressure: (a) a/b, (b) a/c and
606 (c) b/c. Filled black circles are data from this study, open symbols represent data reported in the
607 literature.

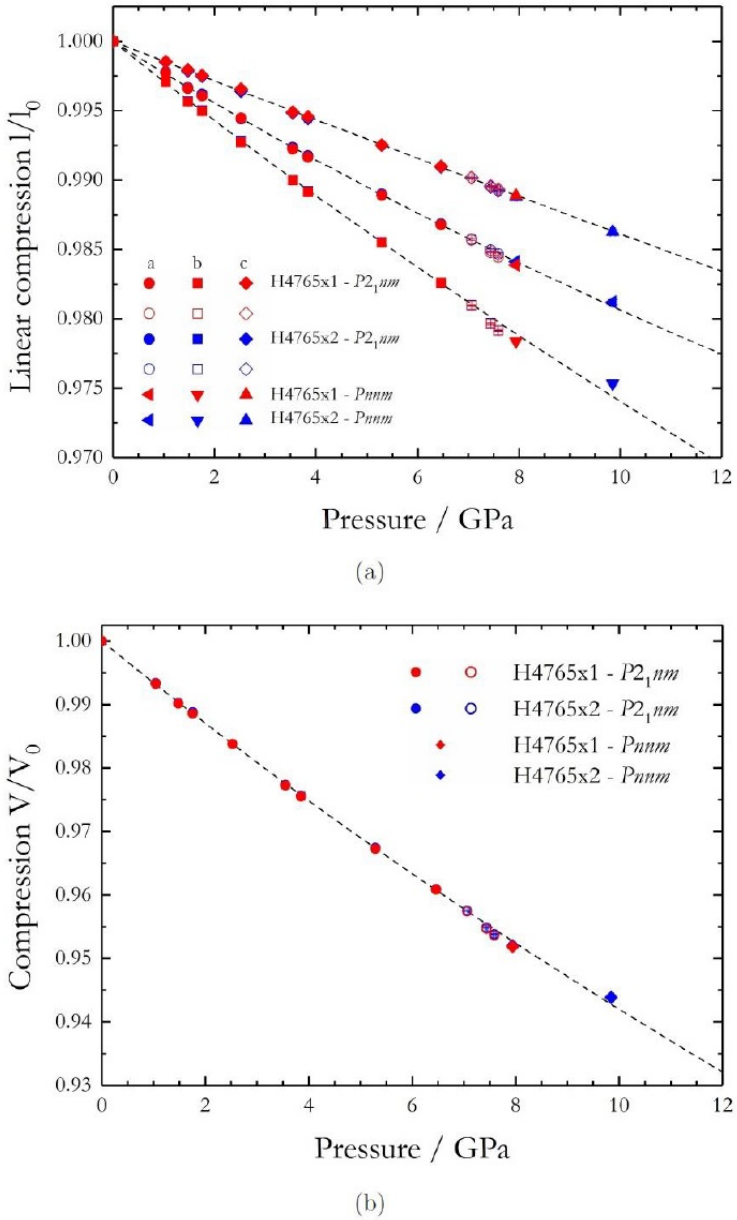

608 **Figure 4.** The unit-cell lattice parameters and (b) the unit-cell volume of δ-(Al,Fe)OOH variation
609 with pressure. The values of each crystal have been normalized with respect to those measured at
610 room pressure. Open symbols refer to data close to the P21nm to Pnnm transition pressure and
611 they were not considered in the BM3 EoS.

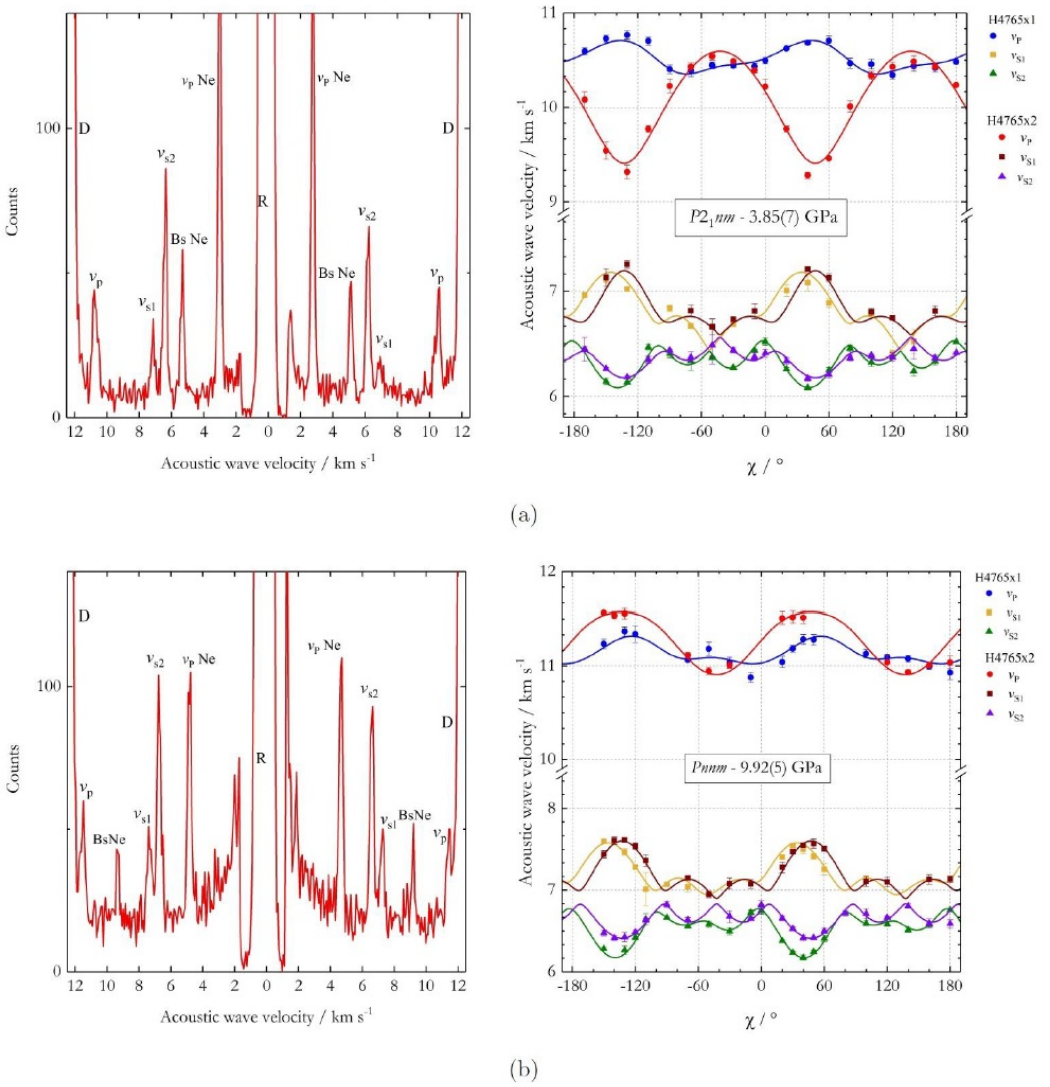

612 **Figure 5**. Representative Brillouin spectra collected for H4765x1 at $\chi = 20°$ of sample H4765
613 and acoustic velocities of both crystals as a function of χ orientation through the $P2_1nm$ to $Pnnm$
614 phase transition: (a) at 3.85(7) GPa, space group $P2_1nm$; (b) 9.92(5) GPa, space group $Pnnm$. R =
615 Rayleigh peak, D = diamond v_S. BsNe = Ne back-scattered.

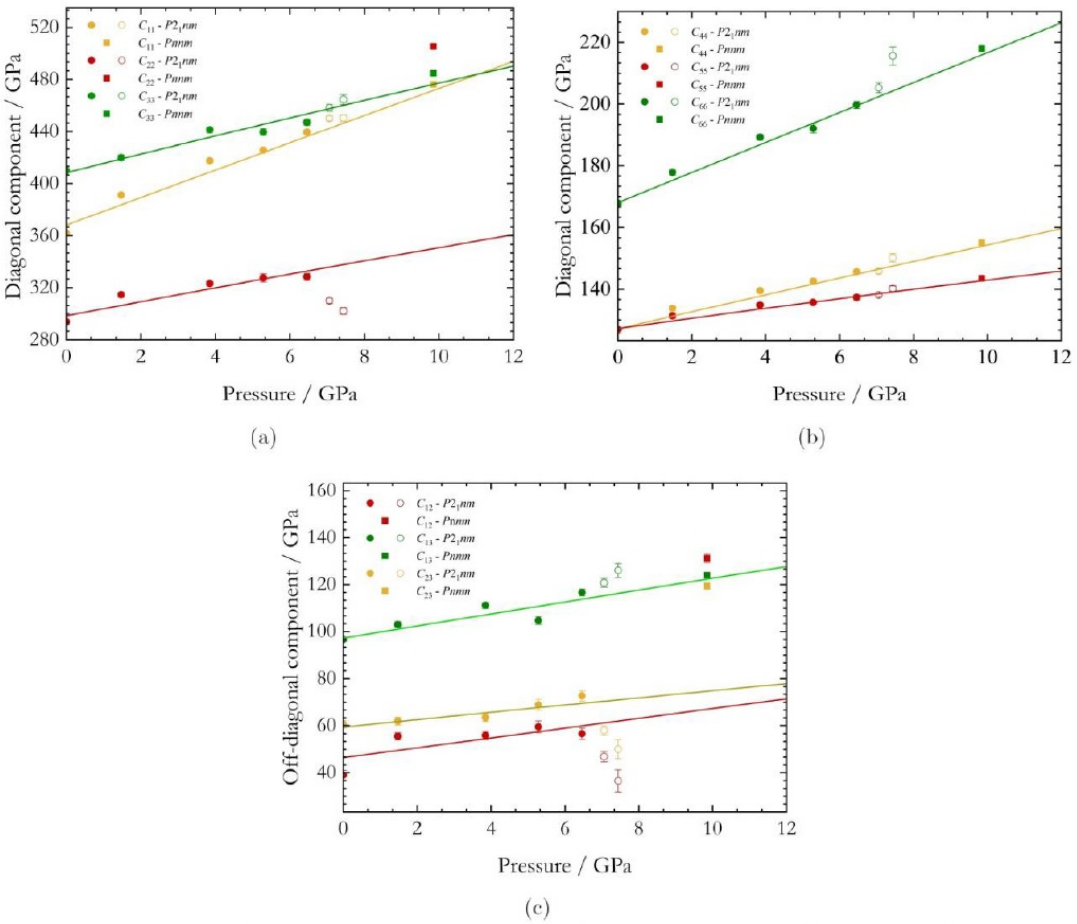

616 **Figure 6.** Variation of the nine components c_{ij} of the elastic tensors of δ-Al,OOH with pressure.
617 Open symbols refer to data close to the $P2_1nm$ to $Pnnm$ transition pressure and they were not
618 considered in the fit.

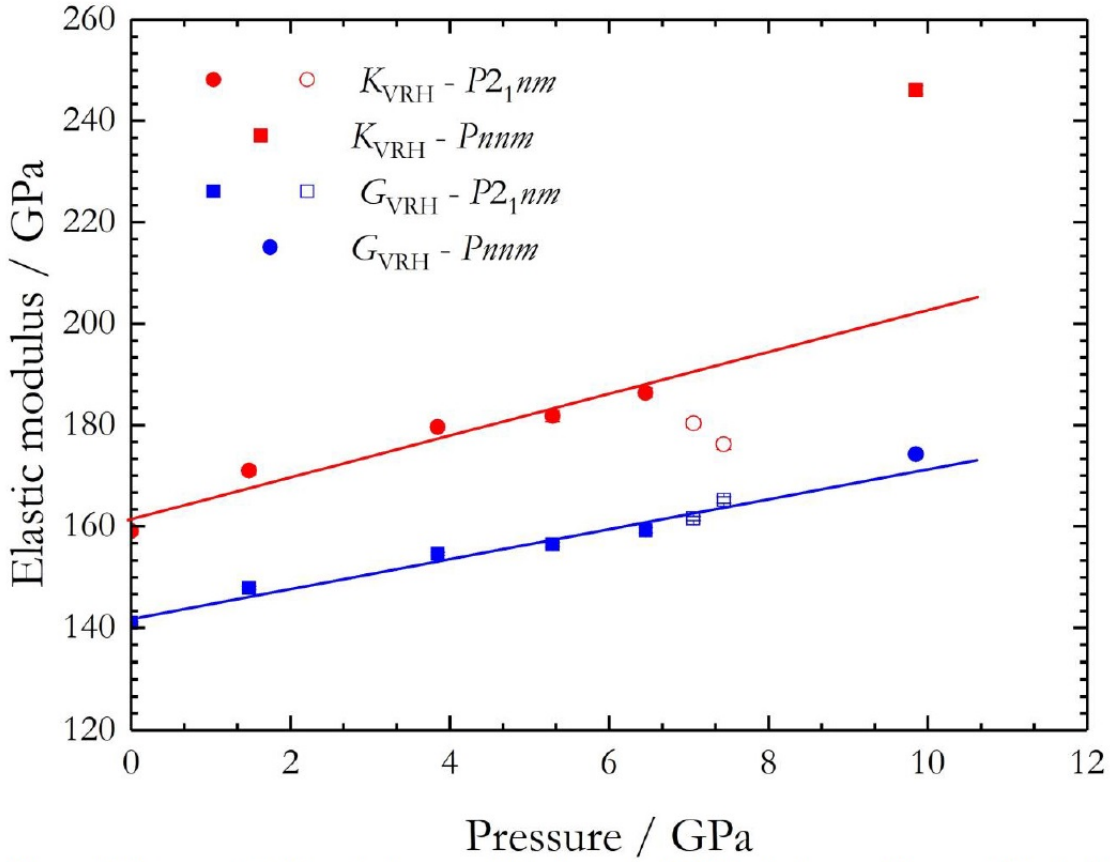

619 **Figure 7.** Aggregate bulk and shear moduli of sample H4765. A large softening of the bulk
620 modulus is observed above 6.5 GPa, whereas the shear modulus variation is continuous through
621 the $P2_1nm$ to $Pnnm$ phase transition.

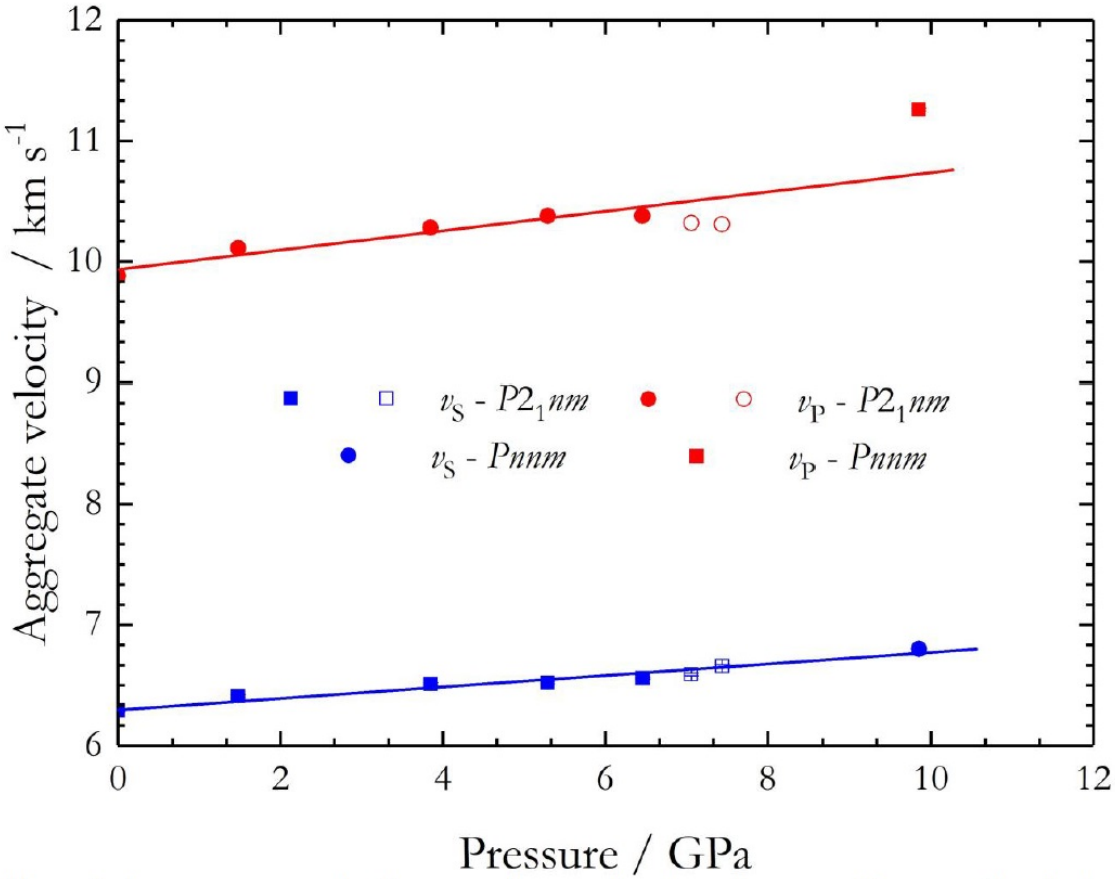

622 **Figure 8**. Aggregate wave velocities v_P, and v_S as a function of pressure. Note a small softening

623 of v_P, above 6.5 GPa and a drastic jump after the $P2_1nm$ to $Pnnm$ phase transition.

624

625 **Tables**

626 **Table 1.** Unit-cell parameters and volumes of constrained at different pressures (*P*). - = not

627 determined.

	H4765x1				H4765x2			
P (GPa)	a (Å)	b (Å)	c (Å)	V (Å^3)	a (Å)	b (Å)	c (Å)	V (Å^3)
Neon – *P*2$_1$*nm*								
10^{-4}	4.7218(7)	4.232(2)	2.8386(8)	56.72(2)	4.7215(8)	4.232(4)	2.8362(4)	56.67(1)
1.04(2)	4.71151(9)	4.2210(2)	2.8338(1)	56.357(3)	4.7092(1)	4.21943(4)	2.83228(5)	56.277(2)
1.48(2)	4.70627(8)	4.2150(2)	2.8321(1)	56.180(3)	4.7040(2)	4.21353(6)	2.83048(7)	56.101(2)
2.53(2)	4.6961(1)	4.2027(4)	2.8282(2)	55.817(5)	4.6933(3)	4.20151(9)	2.8263(1)	55.732(3)
3.85(7)	4.6829(1)	4.1875(6)	2.8225(2)	55.347(7)	4.6807(2)	4.18616(8)	2.8208(1)	55.270(3)
Neon – *Pnnm*								
9.92(5)	-	-	-	-	4.6321(7)	4.1295(3)	2.7978(3)	53.516(8)
Helium – *P*2$_1$*nm*								
10^{-4}	4.72227(5)	4.2335(1)	2.83793(5)	56.737(2)	4.7197(2)	4.23182(4)	2.8365(5)	56.653(2)
1.77(1)	4.70372(5)	4.2121(1)	2.83095(5)	56.089(2)	4.7018(3)	4.21076(6)	2.82939(8)	56.016(3)
3.85(7)	4.68561(6)	4.1911(2)	2.82346(6)	55.446(2)	4.6835(4)	4.18949(8)	2.8219(1)	55.370(4)
5.29(3)	4.66990(5)	4.1721(1)	2.81672(5)	54.878(2)	4.6678(3)	4.17058(6)	2.81528(8)	54.806(3)
6.46(2)	4.65988(6)	4.1598(2)	2.81237(7)	54.515(2)	4.6576(3)	4.15815(6)	2.81086(8)	54.437(3
7.06(3)	4.65464(4)	4.1529(1)	2.81010(5)	54.320(2)	4.6524(2)	4.15143(4)	2.80862(6)	54.245(2)
7.44(1)	4.65046(6)	4.1473(2)	2.80836(7)	54.164(2)	4.6487(4)	4.14592(5)	2.80678(9)	54.095(3)
7.59(3)	4.64883(6)	4.1452(2)	2.80077(7)	54.105(2)	4.6474(4)	4.14372(5)	2.80598(1)	54.036(3)
7.94(2)	4.6461(1)	4.1420(3)	2.8064(2)	54.006(3)	4.64472(3)	4.14035(4)	2.80471(7)	53.936(3)

628

629

630 **Table 2.** Unit-cell volume (V_0), isothermal bulk modulus (K_{T0}) and its pressure derivative (K'_{T0}),
631 unit-cell parameters, linear moduli (M) and their pressure derivative (M'), and axial
632 compressibilities (β) of δ-(Al,Fe)OOH.

V_0 (Å^3)	K_{T0} (GPa)	K'_{T0}		a_0 (Å)	M_a (GPa)	$M'a$	β_a (GPa^{-1})
56.695(3)	149.9(11)	3.7(4)		4.7209(5)	433(4)	17.2(15)	0.00231
b_0 (Å)	M_b (GPa)	M'_b	β_b (GPa^{-1})	c_0 (Å)	M_c (GPa)	M'_c	β_c (GPa^{-1})
4.2327(5)	342(2)	8.4(8)	0.00292	2.8372(7)	698(8)	4(3)	0.00143

633

634

635 **Table 3.** C_{ij} of of δ-(Al,Fe)OOH constrained at different pressures (P). All of the reported values

636 are in GPa.

P	C_{11}	C_{22}	C_{33}	C_{44}	C_{55}	C_{66}	C_{12}	C_{13}	C_{23}
P2$_1$nm									
10^{-4}	362(1)	294(2)	410(1)	126.7(4)	126.(3)	167.8(8)	39(2)	97(1)	61(2)
1.77(1)[a]	391(1)	315(2)	420(2)	134(1)	131(1)	178(1)	56(2)	103(1)	62(2)
3.85(7)[b]	418(1)	323(2)	441(2)	140(1)	134.9(3)	189(1)	56(2)	111(1)	63(2)
5.29(3)[a]	426(1)	328(3)	440(3)	143(1)	135.7(3)	192(1)	56(3)	105(2)	69(2)
6.46(2)[a]	440(2)	328(3)	447(2)	145.6(4)	137(1)	200(1)	57(2)	117(2)	73(2)
7.06(3)[a]	450(2)	310(2)	458(3)	146(1)	138	205(2)	47(2)	121(2)	58(2)
7.44(1)[a]	450(3)	302(3)	465(4)	150(1)	140(1)	216(3)	37(5)	126(3)	50(4)
Pnnm									
9.92(5)[b]	476(2)	505(1)	485(2)	155	143	218(1)	131(2)	124(1)	119(1)
[a] and [b] are used to laber runs that used He and Ne as pressure medium, respectively.									

637

638 **Table 4**. Elastic moduli (in GPa), densities ρ (in g/cm^3) and aggregate velocities in (km/s) of δ-
639 (Al,Fe)OOH constrained at different pressures P (in GPa). V and R subscripts label the elastic
640 moduli values determined assuming Voigt and Reuss bound conditions, respectively. VHR
641 subscript is used to label the Voigt-Reuss-Hill averaged values.

P	K_V	K_R	K_{VRH}	G_V	G_R	G_{VRH}	ρ	v_P	v_S
P2$_1$nm									
10^{-4}	162(1)	156(1)	159(1)	142.2(3)	139.7(2)	141.0(3)	3.560(5)	9.88(1)	6.29(1)
1.77(1)[a]	173(1)	169(1)	171(1)	149.2(4)	146.6(3)	147.9(4)	3.601(5)	10.11(1)	6.41(1)
3.85(7)[b]	183(1)	177(1)	180(1)	156.2(4)	152.9(3)	154.6(3)	3.649(5)	10.28(1)	6.51(1)
5.29(3)[a]	184(1)	179(1)	182(1)	158.5(5)	154.9(3)	156.5(4)	3.680(5)	10.30(1)	6.52(1)
6.46(2)[a]	190(1)	183(1)	186(1)	161.1(6)	157.4(5)	159.3(6)	3.705(5)	10.38(1)	6.56(1)
7.06(3)[a]	185(1)	175(1)	180(1)	164.0(5)	159.1(3)	161.6(4)	3.718(5)	10.32(1)	6.59(1)
7.44(1)[a]	182(1)	170(1)	176(1)	168(1)	162(1)	165(1)	3.729(5)	10.31(1)	6.66(1)
Pnnm									
9.92(5)[b]	246(1)	246(1)	246(1)	176.1(3)	172.4(2)	174.2(3)	3.772(5)	11.26(1)	6.80(1)
[a] and [b] are used to laber runs that used He and Ne as pressure medium, respectively.									

642

(Eidesstattliche) Versicherungen und Erklärungen

(§9 Satz 2 Nr. 3 PromO BayNAT)
Hiermit versichere ich eidesstattlich, dass ich die Arbeit selbstständig verfasst und keine anderen als die von mir angegebenen Quellen und Hilfsmittel benutzt habe
(vgl. Art. 64 Abs. 1 Satz 6 BayHSchG).

(§9 Satz 2 Nr. 3 PromO BayNAT)
Hiermit erkläre ich, dass ich die Dissertation nicht bereits zur Erlangung eines akademischen Grades eingereicht habe und dass ich nicht bereits diese oder eine gleichartige Doktorprüfung endgültig nicht bestanden habe.

(§9 Satz 2 Nr. 4 PromO BayNAT)
Hiermit erkläre ich, dass ich Hilfe von gewerblichen Promotionsberatern bzw. -vermittlern oder ähnlichen Dienstleistern weder bisher in Anspruch genommen habe noch künftig in Anspruch nehmen werde.

(§9 Satz 2 Nr. 7 PromO BayNAT)
Hiermit erkläre ich mein Einverständnis, dass die elektronische Fassung meiner Dissertation unter Wahrung meiner Urheberrechte und des Datenschutzes einer gesonderten Überprüfung unterzogen werden kann.

(§9 Satz 2 Nr. 8 PromO BayNAT)
Hiermit erkläre ich mein Einverständnis, dass bei Verdacht wissenschaftlichen Fehlverhaltens Ermittlungen durch universitätsinterne Organe der wissenschaftlichen Selbstkontrolle stattfinden können.

Bayreuth, _____
Ort, Datum, Unterschrift